MAX-PLANCK-INSTITUT
FÜR METEOROLOGIE

International Max Planck Research School on Earth System Modelling

Earth System Model-based Predictability of Land Carbon Fluxes

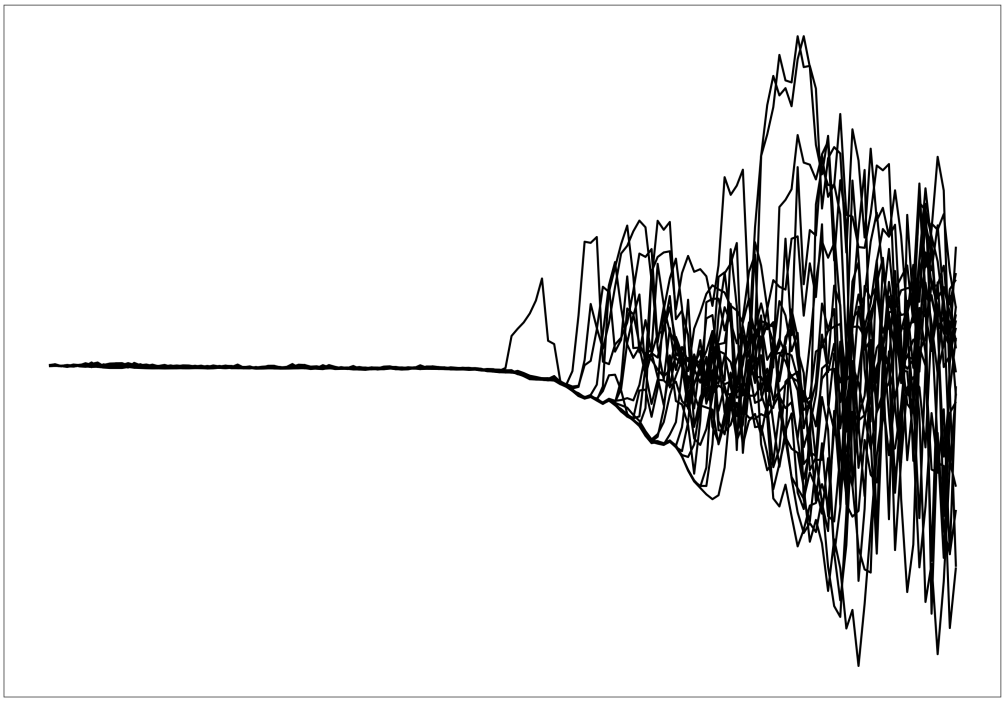

István Dunkl

Hamburg 2022

Berichte zur Erdsystemforschung
Reports on Earth System Science

259
2022

Hinweis

Die Berichte zur Erdsystemforschung werden vom Max-Planck-Institut für Meteorologie in Hamburg in unregelmäßiger Abfolge herausgegeben.

Sie enthalten wissenschaftliche und technische Beiträge, inklusive Dissertationen.

Die Beiträge geben nicht notwendigerweise die Auffassung des Instituts wieder.

Die "Berichte zur Erdsystemforschung" führen die vorherigen Reihen "Reports" und "Examensarbeiten" weiter.

Anschrift / Address

Max-Planck-Institut für Meteorologie
Bundesstrasse 53
20146 Hamburg
Deutschland

Tel./Phone: +49 (0)40 4 11 73 - 0
Fax: +49 (0)40 4 11 73 - 298

name.surname@mpimet.mpg.de
www.mpimet.mpg.de

Notice

The Reports on Earth System Science are published by the Max Planck Institute for Meteorology in Hamburg. They appear in irregular intervals.

They contain scientific and technical contributions, including PhD theses.

The Reports do not necessarily reflect the opinion of the Institute.

The "Reports on Earth System Science" continue the former "Reports" and "Examensarbeiten" of the Max Planck Institute.

Layout

Bettina Diallo and Norbert P. Noreiks
Communication

Copyright

Photos on the back from left to right:
Christian Klepp, Jochem Marotzke,
Christian Klepp, Clotilde Dubois,
Christian Klepp, Katsumasa Tanaka

Earth System Model-based Predictability of Land Carbon Fluxes

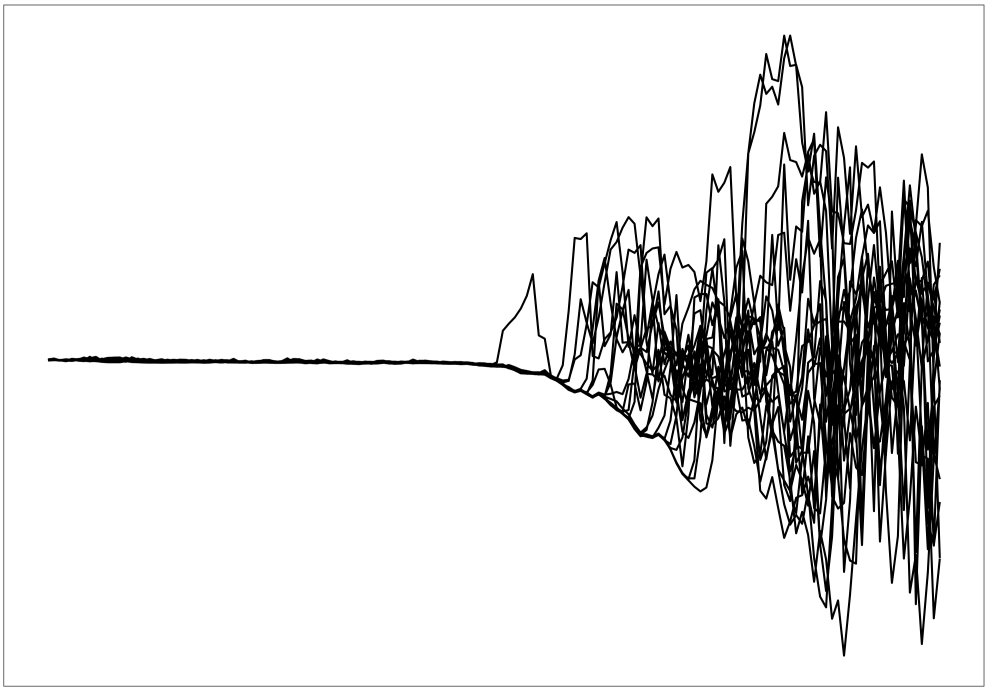

István Dunkl

Hamburg 2022

István Dunkl
Budapest, Hungary

Max-Planck-Institut für Meteorologie
The International Max Planck Research School on Earth System Modelling
(IMPRS-ESM)
Bundesstrasse 53
20146 Hamburg

Tag der Disputation: 2. November 2022

Folgende Gutachter empfehlen die Annahme der Dissertation:
Prof. Dr. Victor Brovkin
Dr. Tatiana Ilyina

Vorsitzender des Promotionsausschusses:
Prof. Dr. Hermann Held

Dekan der MIN-Fakultät:
Prof. Dr.-Ing. Norbert Ritter

Titelgrafik von István Dunkl:
The increasing spread among the simulation members indicates the decline in predictive capability

ISSN 1614-1199 - doi: 10.17617/2.3477022

István Dunkl

Earth System Model-based Predictability of Land Carbon Fluxes

ABSTRACT

The skilful prediction of the terrestrial carbon cycle is necessary to provide near-term estimations of atmospheric CO_2 concentrations. In this dissertation, I study the processes allowing us to predict terrestrial carbon fluxes and identify the current limitations of Earth system models (ESMs) to produce these predictions.

Earlier studies describe the predictability of carbon fluxes as highly variable in space and time, but the patterns of predictability are not well understood. I develop a conceptual framework to study carbon flux predictability based on the predictability of environmental drivers. These drivers explain the spatial and seasonal changes in predictability, as well as the difference in predictability between carbon fluxes.

The spatial variability of predictability implies that there are regional differences in the contribution to atmospheric CO_2 predictability. This regional contribution depends on the interannual variability (IAV) of carbon fluxes, and how much of the IAV is predictable. I analyse six ESMs to determine the uncertainty in these two factors. ESMs are similar in the fraction of IAV they can predict. However, large differences in their IAV patterns are limiting their predictive performance. This discrepancy in IAV results from differences in the role of environmental drivers.

The greatest driving force of IAV patterns in the earth system is arguably El Niño Southern Oscillation (ENSO). ENSO-related teleconnections create a patchwork of predictable climatic anomalies that drive the global carbon cycle. However, differences in the representation of ENSO-related anomalies are restraining the predictive potential of ENSO. The ENSO-related anomalies in gross primary production (GPP) are highest in Southeast Asia and Northern South America. However, the combined anomaly of these two regions ranges between 26% and 75% of global GPP anomalies among the ESMs. I identify the mechanisms leading to these uncertainties and provide information that can be used to reduce model biases.

The potential of ESMs to predict the terrestrial carbon cycle is not yet limited by the chaotic nature of weather and climate, but by the ability to reproduce the IAV of carbon fluxes. Improving our understanding on the sensitivity of carbon fluxes to envi-

ronmental drivers will allow to further expand the predictive potential.

ZUSAMMENFASSUNG

Die Vorhersage des terrestrischen Kohlenstoffkreislaufs ist notwendig, um kurzfristige Schätzungen der atmosphärischen CO_2-Konzentrationen zu erhalten. In dieser Dissertation untersuche ich die Prozesse, die es uns ermöglichen, die terrestrischen Kohlenstoffflüsse vorherzusagen, und zeige die derzeitigen Grenzen der Erdsystemmodelle (ESM) auf, um diese Vorhersagen zu erstellen.

Frühere Studien beschreiben die Vorhersagbarkeit von Kohlenstoffflüssen als sehr variabel in Raum und Zeit, aber die Muster der Vorhersagbarkeit sind nicht gut verstanden. Ich entwickle einen konzeptionellen Rahmen zur Untersuchung der Vorhersagbarkeit von Kohlenstoffflüssen auf der Grundlage der Vorhersagbarkeit von Umweltfaktoren. Diese Faktoren erklären die räumlichen und saisonalen Veränderungen in der Vorhersagbarkeit sowie die Unterschiede in der Vorhersagbarkeit zwischen den Kohlenstoffflüssen.

Die räumliche Variabilität der Vorhersagbarkeit impliziert, dass es regionale Unterschiede im Beitrag zur atmosphärischen CO_2-Vorhersagbarkeit gibt. Dieser regionale Beitrag hängt von der interannualen Variabilität (IAV) der Kohlenstoffflüsse ab und davon, wie viel von der IAV vorhersagbar ist. Ich habe sechs ESM analysiert, um die Unsicherheit in diesen beiden Faktoren zu bestimmen. Die ESM ähneln sich hinsichtlich des Anteils der IAV, den sie vorhersagen können. Große Unterschiede in ihren IAV-Mustern schränken jedoch ihre Vorhersageleistung ein. Diese Diskrepanz bei der IAV resultiert aus Unterschieden in der Rolle der Umweltfaktoren.

Die größte treibende Kraft der IAV-Muster im Erdsystem ist wohl die El Niño Southern Oscillation (ENSO). ENSO-bezogene Telekonnektionen schaffen ein Flickwerk vorhersehbarer klimatischer Anomalien, die den globalen Kohlenstoffkreislauf antreiben. Unterschiede in der Darstellung von ENSO-bezogenen Anomalien schränken jedoch das Vorhersagepotenzial von ENSO ein. Die ENSO-bedingten Anomalien der Bruttoprimärproduktion (GPP) sind in Südostasien und im nördlichen Südamerika

am höchsten. Die kombinierte Anomalie dieser beiden Regionen liegt jedoch zwischen 26% und 75% der globalen GPP-Anomalien in den ESMs. Ich identifiziere die Mechanismen, die zu diesen Unsicherheiten führen, und liefere Informationen, die zur Verringerung von Modellverzerrungen genutzt werden können.

Das Potenzial von ESMs zur Vorhersage des terrestrischen Kohlenstoffkreislaufs ist noch nicht durch die chaotische Natur von Wetter und Klima begrenzt, sondern durch die Fähigkeit, die IAV der Kohlenstoffflüsse zu reproduzieren. Das Potenzial von ESM zur Vorhersage des terrestrischen Kohlenstoffkreislaufs ist durch die Reproduktion der IAV der Kohlenstoffflüsse begrenzt. Ein besseres Verständnis der Empfindlichkeit der Kohlenstoffflüsse gegenüber Umweltfaktoren wird es ermöglichen, das Vorhersagepotenzial weiter auszubauen.

PUBLICATIONS AND PRE-PUBLICATIONS RELATED TO THIS DISSERTATION

APPENDIX A:

Dunkl, I., A. Spring, P. Friedlingstein, and V. Brovkin (2021). "Process-based analysis of terrestrial carbon flux predictability." *Earth System Dynamics* 12.4, pp. 1413–1426.

APPENDIX B:

Dunkl, István, Nicole Lovenduski, Alessio Collalti, Vivek K. Arora, Tatiana Ilyina, and Victor Brovkin. "GPP and the predictability of CO_2: more uncertainty in what we predict than how well we predict it." *Prepared for submission to Biogeosciences*.

CONTENTS

LIST OF FIGURES

UNIFYING ESSAY

1 INTRODUCTION

1.1 PREDICTING ATMOSPHERIC CO_2 CONCENTRATIONS

In the effort to limit global heating to below 2°C, nations have pledged their climate actions in the Paris Agreement in the form of Nationally Determined Contributions (NDCs, Paris Agreement 2015). To keep track of the NDCs and validate their effects, policymakers rely on an accurate estimation of greenhouse gas emissions. This is achieved in a bottom-up approach by national inventories in the global stocktake. However, this stocktaking approach relies on the emission declarations of all countries and is only executed every five years. Although stocktaking provides a retrospective evaluation of the efforts of the past years, its large time steps do not allow a continuous and real-time evaluation of climate mitigation. This could be achieved through the prediction of near-term atmospheric CO_2 concentrations. These predictions would allow policymakers to assess whether proposed climate mitigation will limit atmospheric CO_2 concentrations under a certain threshold, and give them tools for emission budgeting (Friedlingstein et al., 2020).

The need for CO_2 predictions

Changes in atmospheric CO_2 concentrations are resulting from anthropogenic emissions and the amount of carbon absorbed by the land and ocean sinks. It is, however, the land carbon sink that dominates the interannual variability (IAV) of atmospheric CO_2 concentrations (Piao et al., 2020). The prediction of atmospheric CO_2 concentrations therefore requires a skilful prediction of the land carbon sink. One way to achieve this is through simulations with an Earth system model (ESM), which combines a physical climate model with biogeochemical processes of the land surface.

The work presented in this thesis is directed towards exploring the ability of ESMs to predict the terrestrial carbon cycle on a seasonal to interannual timescale. I begin with introducing the key elements of the terrestrial carbon cycle and **identify the relevant processes for predictability**. Then, I analyse the **contribution of these processes** to the predictability of different carbon fluxes. Lastly, I compare the predictability of carbon fluxes between different ESMs to **identify the sources of uncertainty** and make

Exploring our ability to predict the land carbon sink

suggestions on how to overcome these limitations and improve our ability to predict terrestrial carbon fluxes.

1.2 THE GLOBAL CARBON CYCLE

Changes in the concentration of atmospheric CO_2 are caused by human activities and through changes in the natural carbon reservoirs. Anthropogenic emissions include the use of fossil fuels and land-use change. Around 25% of these emissions are absorbed by the ocean sink and around 30% by the land sink (Peters et al., 2017). While the ocean carbon sink can be estimated well, the terrestrial carbon sink is the least constrained part of the global carbon cycle (Friedlingstein et al., 2020; Luo, Keenan, and Smith, 2015). Its size is inferred indirectly, by deducting the other carbon sources and sinks from atmospheric measurements.

Where do anthropogenic emissions go?

The ocean and land sink also differ in their dynamics and contribution to the IAV of atmospheric CO_2. Ocean carbon uptake takes place in the form of CO_2 solubility and biological productivity. These processes are driven by ocean circulation and the ventilation of the deep ocean (McKinley et al., 2017). Compared to conditions on the land surface, these processes are relatively slow and lead to the ocean carbon cycle undergoing a low-frequency variability. While the ocean carbon sink has a comparably low IAV between 0.11 and 0.25 PgC yr^{-1}, the IAV of the land carbon sink is 2 PgC and thus drives atmospheric CO_2 variability (Friedlingstein et al., 2020). Since there is no need for predictions without variability, the first step towards finding the mechanisms of predictability is understanding the origins of variability.

A conceptual model for carbon flux predictability

One way to gain insight into the terrestrial carbon sink is through the lens of its drivers. Terrestrial carbon fluxes are driven by environmental variables such as temperature, moisture, or radiation. However, it is not only the variability of carbon fluxes that is determined by its drivers – but also their predictability. Every environmental driver undergoes different temporal dynamics in the earth system. For instance, solar radiation can change on an hourly scale, while anomalies in soil moisture can persist for years (Chikamoto et al., 2017). These differences in temporal dynamics determine the persistence of anomalies and influence how well each of these environmental drivers can be predicted. As a result, carbon flux anomalies which are driven by soil moisture have a generally higher pre-

dictability than anomalies driven by radiation. However, it does not matter how predictable an environmental driver is if it has a low variability, or the carbon flux is not very sensitive to it. Based on this conceptual framework, the major elements which determine carbon flux predictability are: a) which environmental variables drive the carbon flux, b) how sensitive is the carbon flux to the drivers, c) how strong is the variability of these drivers, and d) how much of the variability of the drivers is predictable. Quantifying the role of environmental drivers on the land carbon sink is the key to a process-based understanding of its predictability. However, the land carbon sink is not the result of a single process. Rather, it is the sum of several carbon fluxes. Each of these fluxes has a different set of drivers, as well as spatially and temporally varying sensitivities to those drivers.

Carbon fluxes and their drivers

The main fluxes contributing to the land carbon sink are gross primary production (GPP), which is the carbon entering ecosystems through photosynthesis; autotrophic and heterotrophic respiration (Ra and Rh), which is the carbon returned to the atmosphere through plants and microbial decomposition; and disturbances like fire. GPP is driven by the availability of energy in the form of temperature and radiation, plus the necessary resources: water, CO_2, and nutrients like nitrogen (Anav et al., 2015). Depending on the environmental conditions, any of these drivers can be the limiting factor of GPP – but not all of them create enough variability. For example, although plant growth is limited by CO_2 in dry regions (Donohue et al., 2013), the IAV of CO_2 does not significantly contribute to GPP IAV (Lee et al., 2018). Most of GPP IAV is caused by soil moisture, temperature and radiation (Anav et al., 2015). GPP increases with temperature in mid- to high-latitudes due to higher chemical reaction rates, but the relationship reverses as high temperatures damage enzyme structure and reduce the leaf-to-air vapour pressure difference necessary for photosynthesis (Aubry-Kientz et al., 2015). Therefore, GPP is negatively correlated with temperature across most of the tropics (O'Sullivan et al., 2020). GPP is positively correlated to soil moisture in most parts of the globe, but the strongest relationship is in the semi-arid tropics (Anav et al., 2015; O'Sullivan et al., 2020). Because plants respire some fixated carbon back to the atmosphere, we can quantify the net carbon fixated by plants as net primary production (NPP) by subtracting Ra from GPP. Ra is most sensitive to temperature (Piao et al., 2010), but since the amount of carbon available for Ra depends on the photosynthetic rate, GPP, Ra and NPP covary

(Van Oijen, Schapendonk, and Höglind, 2010). The main drivers of Rh variability are temperature, soil moisture and substrate availability (Chen et al., 2010; Reichstein et al., 2003). As temperature regulates the rate of chemical reactions, Rh increases with temperature as long as it does not lead to the limitation of other environmental factors (Wei, Weile, and Shaopeng, 2010). The relationship of Rh to moisture availability depends on the prevailing climatic conditions and ranges from strongly positive under water limitation, to negative when water saturation creates anaerobic conditions (Reichstein et al., 2003).

IAV of carbon fluxes

The IAV of the land carbon sink is mostly driven by the IAV of GPP and Rh, while fire emissions only play a minor role (Niu et al., 2017; Piao et al., 2020; Wang, Zeng, and Wang, 2016). Because of its high sensitivity to climate, GPP is considered to drive 56% to 90% of the terrestrial carbon sink IAV (Baldocchi, Chu, and Reichstein, 2018; Piao et al., 2020). However, there are some regions where Rh IAV drives the terrestrial carbon sink IAV. This is the case for the high latitudes, Australia and possibly parts of the Amazon basin (Jung et al., 2011; Piao et al., 2020; Schömann et al., 2022).

Covariability of fluxes

Because GPP and Rh share similar environmental drivers, their individual variabilities can covary, leading to an amplification or dampening of net variability. For most parts of the world, the high GPP variability is dampened by the positively correlated Rh because both fluxes are favoured by similar climatic conditions (Baldocchi, Chu, and Reichstein, 2018). However, this relationship can be reversed in the tropics, where extreme climatic conditions amplify the carbon sink by the covariability of GPP and Rh (Qian, Joseph, and Zeng, 2008). This occurs in the Amazon basin, where high temperatures can induce droughts, which lower plant productivity while increasing Rh.

Uncertainties of flux estimates

The spatial patterns of carbon flux IAV are highly heterogeneous, with small portions of the land surface driving global IAV (Poulter et al., 2014). The majority of the terrestrial carbon sink IAV can be attributed to tropical GPP. To be more specific, IAV peaks in warm, but water-limited ecosystems like the semi-arid tropics (Ahlström et al., 2015; Jung et al., 2011). However, there are large uncertainties in carbon flux IAV patterns among ESMs (O'Sullivan et al., 2020; Poulter et al., 2014). These errors originate from our limited understanding of the role of environmental drivers on carbon fluxes (Piao et al., 2020). For some regions, studies find opposing effects of water availability on

the carbon cycle, and the global sensitivity of carbon fluxes to environmental drivers are poorly constrained (Piao et al., 2010).

Observational products

One of the reasons for the high uncertainties in the terrestrial carbon cycle is the difficulty to measure carbon fluxes (Berkelhammer et al., 2014). The measurements of individual carbon fluxes, like GPP and NPP, rely on costly procedures like biomass inventories, sap flow methods, or leaf level measurement of photosynthesis (Baldocchi et al., 1996). Flux tower stations have eased this process by providing continuous measurements of high temporal resolution at hundreds of locations (Walther et al., 2022). However, they come with the caveat of measuring net land-atmosphere carbon fluxes and rely on statistical approaches to separate the total flux into individual carbon fluxes. Another limitation of flux towers is their sparse and uneven distribution, which leaves large parts of the tropics unsampled (Zhang and Ye, 2021). One source of spatially continuous maps are based on remote sensing data, most notably MODIS (Running, Qiaozhen, and Zhao, 2019). These products estimate GPP through the light use efficiency concept, which utilizes the fraction of absorbed photosynthetic active radiation by plants (O'Sullivan et al., 2020). A shortcoming of these methods is their low sensitivity in areas of high GPP values (Zhang and Ye, 2021). Another source of spatially continuous GPP data is produced by using remote sensing and climate data to upscale flux tower measurements (Jung et al., 2011). This product is widely verified and frequently serves reference for mean GPP values (Zhang and Ye, 2021). However, these products underestimate GPP IAV (Anav et al., 2015; O'Sullivan et al., 2020). It is recommended to scale the data so that the IAV of its integrated fluxes resemble observations (Jung et al., 2019).

1.3 ESM-BASED PREDICTION SYSTEMS

ESM predictions as decision aids

Modelling atmospheric CO_2 dynamics requires simulating several interacting realms. The necessary elements are combined in ESMs, which simulate the physical, chemical and biological processes of the atmosphere, oceans and land surface. Adding the biosphere to a physical climate model allows ESMs to simulate not just weather and climate, but also droughts, agricultural and fishery yields, habitat loss, resource availability, and more (Bonan and Doney, 2018; Flato, 2011; Merryfield et al., 2020). This makes ESMs a valuable tool to provide decision-makers

with predictions on topics with high social, economic, and environmental impact (Merryfield et al., 2020).

To generate predictions, an ensemble of ESM simulations is initialized from observations. Each member is initialized from slightly altered conditions, and as the inherent chaotic nature of climate develops, the ensemble members are driven apart. In a system with little predictive capability, the ensemble members will soon represent the natural variability of the system. However, there are certain processes which provide predictability by delaying this convergence to the climatic variability. These sources of predictability originate from the atmosphere, the oceans or the land surface, and operate on different temporal scales.

Predictability in the earth system from...

The atmosphere, for example, plays a large role for weather predictability, but anomalies do not persist longer than a few months (Merryfield et al., 2020). Notable drivers of atmospheric predictability are climate modes with low-frequency oscillations such as the Madden–Julian oscillation, the North Atlantic Oscillation or the quasi-biennial oscillation (Merryfield et al., 2020; Scaife et al., 2014).

...the atmosphere...

Due to their large heat capacity, oceans are the dominant driver of seasonal to decadal climate variability (Bellucci et al., 2015; Merryfield et al., 2020). The most prominent source of predictability in the oceans is the El Niño–Southern Oscillation (ENSO, Zeng et al. 2008). ENSO describes the periodic fluctuations of tropical Pacific sea surface temperature (SST) and their coupling with the atmosphere (Zhang et al., 2019). Every two to seven years, warm SST anomalies in the tropical Pacific lead to anomalies in radiation, temperature and precipitation ranging from Alaska to Australia, influencing 48% of vegetated land area (Zhang et al., 2019). Not only does ENSO drive global climate variability, its events are also predictable up to one, and sometimes two years in advance (Barnston et al., 2019; DiNezio et al., 2017). Therefore, ENSO is considered the main driver of seasonal to annual climate predictability (Chen and Dool, 1997; Manzanas et al., 2014).

...the oceans...

The land surface contributes to predictability by prolonging or intensifying climatic anomalies. An important source of predictability on the land surface is soil moisture memory (Bellucci et al., 2015). Its initialization plays a crucial role in temperature predictability (Ardilouze et al., 2017). Through its properties as a porous medium, soils act as a water reservoir that can prolong precipitation anomalies for up to 10-45

...the land surface.

months (Chikamoto et al., 2017). These anomalies directly impact plant growth through water availability and regulate the water and energy exchange at the land-atmosphere interface. This process is known as land-atmosphere coupling and drives surface temperatures and precipitation through evapotranspiration. Land-atmosphere coupling contributes to the maintenance and intensity of droughts (Bellucci et al., 2015). Vegetation can have a similar memory function as soil moisture. Although initializing of vegetation contributes little to temperature predictability, it improves the simulation of the hydrological cycle (Weiss et al., 2014). Nevertheless, the initialization of vegetation might be a more important source of predictability for carbon fluxes because it determines the leaf area available for carbon fixation as well as the amount of carbon available for decomposition. But vegetation might have more potential to provide long-lasting memory through less studied mechanisms like the drought legacy effect (Kaisermann et al., 2017; Lozano et al., 2022).

Ensemble initialization methods

There are a variety of approaches to initialize ESMs (Carrassi et al., 2018). The main differences between the approaches lie in the fields that are initialized, the spatial extent of the initialization, and the method used to bring the model closer towards observations. The most frequently initialized variables for seasonal to decadal predictions are ocean temperature, salinity, and sea-ice (Ilyina et al., 2021). Atmospheric fields such as temperature, wind components or humidity can be initialized, but they play a smaller role on these timescales as their anomalies do not persist long (Kataoka et al., 2020; Magnusson et al., 2013; Smith, Scaife, and Kirtman, 2012). The two main approaches in initialization techniques are (a) full-field initialization, in which model fields are replaced by the best estimates of the real state, and (b) anomaly initialization, where the observed climatic anomalies are translated to anomalies according to the model climatology (Smith, Scaife, and Kirtman, 2012). Although both methods have their advantages and shortcomings, they suffer from some degree of initialization shock. This occurs because forcing models out of their free run towards the observations removes them from their internal equilibrium, leading to a climate drift.

There are no observations to provide the initial conditions of the necessary land surface variables at the required resolution. Instead, the initial conditions are estimated indirectly through assimilation runs, but this method is restraining the full predictability potential (Spring et al., 2021).

1.4 MEASURING PREDICTABILITY

From predictive skill to potential predictability

The ensemble simulations used to assess predictability can either be run as forecasts, initialized with present conditions, or as retrospective forecasts (hindcasts), which are initialized from past conditions. The fore- and hindcast are verified against observations to obtain the prediction skill, which quantifies the suitability of the model to predict the real world (Kumar, Peng, and Chen, 2014). However, forecast verification is difficult if observations are unavailable or have high uncertainty, which is the case with terrestrial carbon fluxes. The proposed solution to overcome a lack of observations is to assess the potential predictability (Séférian, Berthet, and Chevallier, 2018). This method tests how well the models can predict themselves instead of observations. The requirements for this approach are the perfect reproduction of the observed variability and the implementation of all predictability-providing processes (Séférian, Berthet, and Chevallier, 2018). Because there are no spatially continuous and reliable observations of terrestrial carbon fluxes, only potential predictabilities are assessed in the following sections. All references to carbon flux predictability refer to potential predictability unless declared otherwise.

A variety of metrics are proposed to quantify predictability from ensemble simulations (Brady and Spring, 2021). One type of metric compares the ensemble mean to observations or an anticipated value. These metrics could measure the distance or the correlation between prediction and observations. Another type of metric focuses on the variance between the ensemble members. Comparing the ensemble variance with a reference variance quantifies how much the prediction is able to restrict the possibility of outcomes.

Carbon flux predictability metric dilemma

The role of terrestrial carbon flux predictability on the predictability of atmospheric CO_2 is a multifaceted problem that can not be fully analysed by using a single predictability metric. For instance, one interesting question is to assess the memory retention potential of ecosystems. In other words, how long does it take until the effects of initialization are undistinguishable from internal variability? To analyse the differences in memory retention, we need to use a metric that is independent of the absolute magnitude of variability. This applies to correlation-based metrics, or to metrics that are scaled by the local variability. Although these metrics allow us to evaluate the regional role of the sources of predictability, the regions with high memory

retention might not be the ones contributing to the predictability of atmospheric CO_2. This can be seen by very high values of the temporal autocorrelation of soil moisture in very wet and very dry regions (Dirmeyer, Halder, and Bombardi, 2018; Hagemann and Stacke, 2015). Despite being regions with above-average memory retention, these regions are characterized by a very small IAV of carbon fluxes and contribute little to the IAV of the global carbon sink (Piao et al., 2020). Therefore, assessing the regional contribution to the predictability of atmospheric CO_2 requires a metric which considers absolute flux IAV: The tropics may not have the best memory retention, but because of their high carbon flux IAV, they matter for the predictability of atmospheric CO_2.

The use of ESMs for terrestrial carbon flux predictability

So where do we stand with the use of ESMs to predict the terrestrial carbon cycle? An early study shows that it is possible to predict terrestrial carbon fluxes beyond nine months, and that predictability originates from the dynamical coupling of the land surface and climate that allows predictions of carbon fluxes beyond climate predictability (Zeng et al., 2008). Subsequent studies estimated the predictability of terrestrial carbon fluxes to be around two years (Ilyina et al., 2021; Li et al., 2022; Lovenduski et al., 2019; Spring and Ilyina, 2020; Séférian, Berthet, and Chevallier, 2018). The results showed that carbon flux predictability is distributed unevenly across the land surface. Most of the regions with high predictability are in the tropics, but there are deviations among the ESMs on the location of these regions. These patterns broadly resemble the ENSO-induced climate anomalies (Zeng et al., 2008), but no other explanation for these patterns is offered yet. Some of the listed studies address the question of predictability mechanisms by comparing simulations with and without initialized land surface. They find that the predictability of carbon fluxes increases with the initialization of soil moisture, vegetation, snow cover, as well as carbon and nitrogen pools (Lovenduski et al., 2019; Spring et al., 2021; Zeng et al., 2008). However, these studies assess the combined effect of several land surface variables that does not allow the attribution of predictability to single processes.

Knowledge gaps

Although we understand the general importance of these land surface processes, we still know little about the mechanisms of terrestrial carbon flux predictability. Why do some areas have higher predictability than others? Is predictability continuously decreasing with time, or does it change with the seasons? How does the uncertainty in the parameterization of carbon fluxes

affect predictability, and what are the current limitations in predictability? In the following chapters, I provide answers to these questions and guidance for future improvements of terrestrial carbon flux predictability.

2

PAPER I: MECHANISMS OF PREDICTABILITY

The predictability of terrestrial carbon fluxes is estimated to be around two years in several ESMs (Ilyina et al., 2021; Lovenduski et al., 2019; Spring and Ilyina, 2020; Séférian, Berthet, and Chevallier, 2018), but there is considerable spatial and temporal variability in these values. ESMs show that carbon flux predictability has a heterogeneous distribution within the tropics, leading to areas of high and low predictability. The estimates for globally aggregated carbon flux predictability also show a large IAV (Spring and Ilyina, 2020; Séférian, Berthet, and Chevallier, 2018). This could indicate that predictability is better in some years than others. As far as understanding the mechanisms of carbon flux predictability goes, most publications have focused on the effect of land surface initialization on carbon flux predictability on a global and annual scale (Lovenduski et al., 2019; Spring and Ilyina, 2020; Zeng et al., 2008). However, carbon fluxes are driven by several variables, and we know little about the role of the individual drivers in creating the observed patterns of carbon flux predictability.

Mechanisms of predictability largely unknown

This work focuses on understanding the mechanisms leading to carbon flux predictability and its variability by studying the relationship between carbon fluxes and their drivers. I use the assumption that the predictability of carbon fluxes is related to the predictability of its drivers. Within this framework, I analyse the contribution of environmental drivers to the regional patterns of carbon flux predictability at a monthly timescale to answer the following questions:

Research questions

1. **How do the environmental drivers of carbon fluxes contribute to the patterns of carbon flux predictability?**
2. **What mechanisms explain the seasonal variability and IAV of carbon flux predictability?**

Because the net land-atmosphere carbon flux is a composite of different fluxes, each with its own sensitivity to its drivers, we focus on two carbon fluxes contributing to a majority of the variability (Wang, Zeng, and Wang, 2016). NPP quantifies the amount of carbon fixated into the ecosystems by vegetation and is driven by soil moisture, temperature and radiation. Rh is the

Methods

largest flux of ecosystem carbon back to the atmosphere, and is driven by precipitation, temperature and substrate availability.

The data for this analysis is based on 35 ensemble simulations initialized along an unforced control run with the Max Planck Institute Earth System Model (MPI-ESM) version 1.2 (Mauritsen et al., 2019). Because this work aims to study the IAV of predictability, the starting points for the 35 initializations are selected to cover a wide range of ENSO conditions. The ensembles start in January, have 11 members, run for two years, and are initialized by small atmospheric perturbations to create divergence. Predictability is measured by comparing ensemble variance with climatological variance. I calculate the complement of the normalized ensemble variance (Griffies and Bryan, 1997):

$$V_c(t) = 1 - \frac{\sigma^2(t)_{Ensemble}}{\sigma^2_{Climatology}}, \tag{2.1}$$

where $\sigma^2(t)_{Ensemble}$ is the ensemble variance at lead time t, and $\sigma^2_{Climatology}$ the climatological variance for that given month of the year. A V_c of one means there is zero spread in the ensemble, and values under zero mean that the variance within the ensemble is larger than the climatological variance. In the next step, I use regression analysis to determine what is driving the predictability of NPP and Rh. For every grid cell and lead time, a multiple linear regression model is fitted. The regression models determine the contribution of the predictability of environmental drivers to NPP and Rh predictability.

Drivers of global predictability

The analysis allows us to identify the main drivers of carbon flux predictability. Global NPP predictability is driven to 62%, 30%, and 8% by the predictability of soil moisture, temperature, and radiation, respectively. Rh predictability is driven to 52%, 27%, and 21% by the predictability of substrate availability, temperature, and precipitation. The drivers are not distributed evenly across the globe but form distinct spatial patterns, which makes it possible to attribute hotspots of carbon flux predictability to individual drivers. There is also a difference in the persistence of NPP and Rh predictability. While most of the NPP predictability decays during lead year 1, there are still large areas with high Rh predictability in lead year 2. This can be explained by differences in the predictability of the drivers. Rh is driven to 52% by substrate availability, which has a very high predictability due to slow changes in its stocks.

Seasonal variability of predictability

Both NPP predictability and Rh predictability show a strong seasonality, and some regions even lose their predictability before it returns the next year. Curiously, the seasonality of NPP and Rh predictability have opposite phases, with NPP predictability peaking in the dry, and Rh predictability in the wet season. Nevertheless, I discovered that in both cases, the seasonality is caused by the same mechanism. The seasonal patterns of predictability are due to the seasonally changing environmental drivers of the fluxes, and the differences in the predictability of these drivers. On the one hand, we have substrate availability and soil moisture, which have very good predictability because they are the result of slowly varying processes. Radiation and precipitation, on the other hand, have a much lower predictability on the scale of days to weeks. NPP is limited by radiation in the wet season, meaning that NPP variability is caused by a poorly predictable driver. With the progression into the dry season, NPP becomes limited by water availability and NPP "inherits" the high predictability of soil moisture. Rh is limited by poorly predictable precipitation in the dry season, but its predictability increases as it becomes limited by substrate availability. The seasonally changing limiting factors especially contribute to the lengthening of Rh predictability. This happens as the dry season halts the decomposition and preserves the anomalies in substrate availability until the start of the wet season in the next year.

IAV of predictability

Within the analysed ensemble simulations, NPP predictability showed a high IAV. There are several grid cells where the standard deviation of NPP predictability exceeds the mean. I found that interannual differences in NPP predictability can be explained by hydrological conditions. The two regions where NPP predictability is the most impacted by this relationship are the Amazon Basin, where NPP predictability is higher in wet years, and northwestern Australia, where NPP predictability is higher in dry years. Although the direction of the relationship differs, it is the same phenomenon that creates the differences in predictability between years. In the case of the Amazon Basin, the variability of precipitation does not differ between wet and dry years, but years with above-average precipitation lead to the saturation of soils (Fig. 2.1). With sufficient precipitation, more and more ensemble members are "synchronized" in the saturated state, causing reduced variability of soil moisture. This decreases the ensemble variability of NPP through (a) less variability in water availability, and (b) reduced variability of

temperature due to reduced variability of latent and sensible heat flux. In the case of Australia, NPP predictability increases in dry years due to the higher predictability of soil moisture and radiation. Here, the ensemble members are synchronized because drought pushes the ensemble members against the depleted end of the spectrum. While there is some variability of cloud cover in wet years, variability of radiation decreases in dry years as the chance for cloud free days increases. For both the Amazon and Australia, the interannual differences in predictability are caused by years when the environmental conditions are pushed against the physical boundaries of the system, which leads to a synchronization of ensemble members.

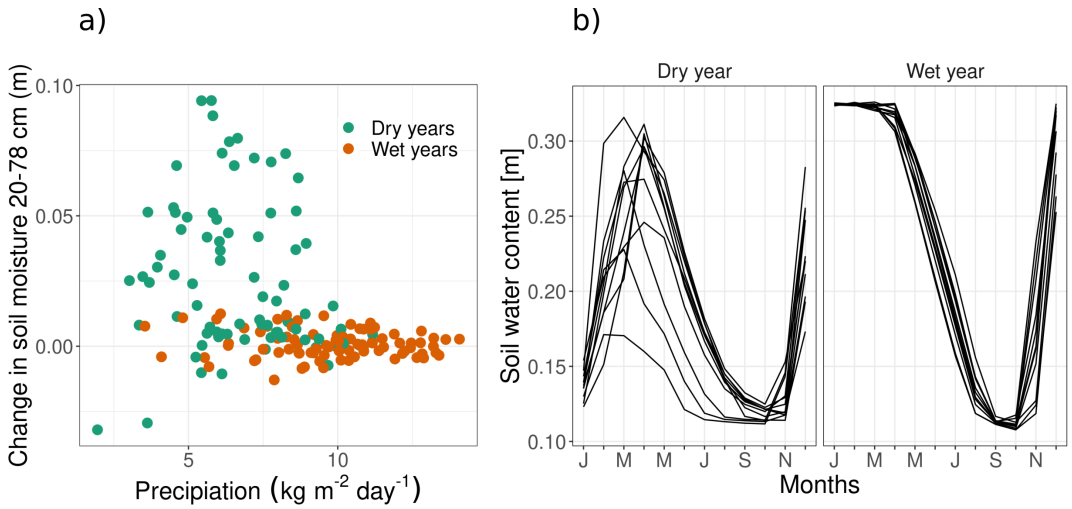

Figure 2.1: Soil water dynamics of dry and wet years in the Amazon basin at 8°S, 54°W. a) Relationship between February precipitation and change in soil moisture from February to March. While the variability in precipitation is similar in dry and wet years, there is only little change in soil moisture in the wet years. b) Soil water content of the 11 ensemble members for a single dry and wet year.

Key findings and conclusions

The majority of carbon flux predictability can be explained by the predictability of land surface variables such as soil moisture and substrate availability. The leading role of soil moisture is pointed out by other publications, stressing the importance of land surface initialization (Spring et al., 2021; Zeng et al., 2008). However, soil moisture monitoring is costly, and initial conditions have to be estimated indirectly through assimilation runs. This work shows that there are key hotspots of predictability which are driven by soil moisture. The identification of these

regions allows a targeted expansion of soil moisture monitoring at locations that maximize their impact on predictability.

The different predictabilities of environmental drivers explain the difference between NPP and Rh predictability, as well as variations in the seasonality of predictability. The IAV of carbon flux predictability is caused by environmental conditions approaching the physical boundaries of the system. This implies that the patterns of carbon flux predictability are highly dependent on model structure and the parameterization of ecosystem processes. Differences in the representation of processes like evapotranspiration, phenology, or climate variability can alter resource availability. This may cause changes in the limiting factors of carbon fluxes which determine their predictability.

I identify mechanisms responsible for the variability of predictability which are based on well understood processes. These mechanisms should be present in other ESMs, but it is difficult to conclude whether the spatio-temporal patterns of carbon flux predictability are specific to MPI-ESM or resemble the patterns found in other ESMs.

3

PAPER II: DRIVERS OF VARIABILITY

How much a region contributes to the predictability of CO_2 depends on two factors: How high is the IAV of carbon fluxes, and how much of this IAV can we predict. In Chapter 2, we discussed the latter, but we have not yet considered the differences in IAV. Despite the ongoing efforts of field scientists and model developers, several of the processes controlling the variability of GPP remain poorly constrained (Luo, Keenan, and Smith, 2015; Piao et al., 2020). There are large differences in the way ESMs reproduce the sensitivity of GPP to climate (Piao et al., 2013, 2020), phenology (Song et al., 2021), biome boundaries (Hu et al., 2022), or hydrology (Qiao, Zuo, and Xiao, 2022; Wu, Lo, and Scanlon, 2021). All of these uncertainties are likely to lead to different patterns of GPP IAV, which is the main driver of atmospheric CO_2 (Piao et al., 2020). This raises the question of how much these differences in GPP IAV will affect the predictability patterns among the ESMs. Are the earlier discovered predictability patterns specific to MPI-ESM or can they be generalized? In a multi-model analysis, I take a look at the role of environmental drivers in GPP IAV and predictability in six ESMs. The aim of this work is to identify the factors leading to the differences in carbon flux predictability between the ESMs. To investigate this topic, I ask:

The role of IAV patterns on predictability

1. **What drives the differences in carbon flux predictability among ESMs?**

2. **How it is possible that the predictive skill of atmospheric CO_2 is similar among ESMs (Ilyina et al., 2021), while there are large uncertainties in the key processes controlling terrestrial carbon flux IAV?**

I analyse six ESMs to find out how environmental drivers are affecting the IAV and predictability of GPP. I use regression analysis to determine the sensitivity of GPP to soil moisture, temperature and radiation. The regression model is applied to hindcast simulations to determine (a) the IAV of GPP caused by each driver and (b) the variability of GPP between the ensemble members in lead year one (caused by each driver). Predictability is calculated from the relationship of ensemble variability to

Role of environmental drivers on IAV and predictability

IAV. In Figure 3.1, I use a high- and a low-productivity site to exemplify how I calculate predictability and why one metric is not enough. The predictive component (pc) is the difference between IAV and ensemble variability in lead year one. Because pc is an absolute measure that factors in the size of anomalies, it allows quantifying the regional contribution to atmospheric CO_2 predictability. However, pc is strongly related to the overall magnitude of GPP IAV and does not give us an insight into how well memory is stored in the system. This is demonstrated with the example of the dry shrubland in Figure 3.1. The dry shrubland has a relatively small pc compared with the tropical forest, but a much larger predictable fraction (pf), which is the ratio of pc to IAV. pf allows us to assess how well memory is stored in the system. The IAV patterns of GPP are compared with observations from MODIS (Running, Qiaozhen, and Zhao, 2019) and FLUXCOM (version RS + METEO, Jung et al. 2019).

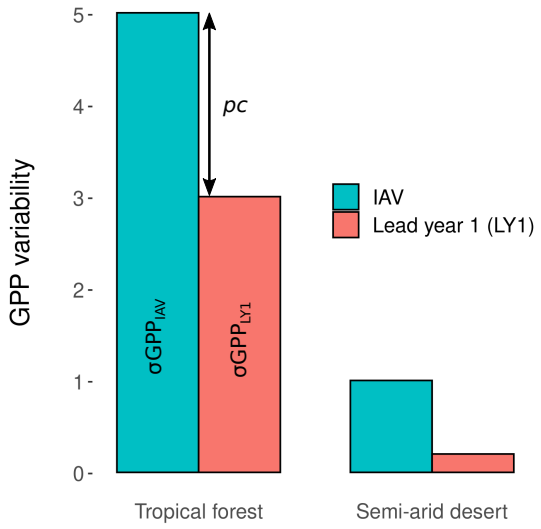

Predictable component (*pc*):
$pc = \sigma GPP_{IAV} - \sigma GPP_{LY1}$

Predictable fraction (pf):
$pf = pc / \sigma GPP_{IAV}$

	Tropical forest	Dry shrubland
pc	2	0.8
pf	0.4	0.8

Figure 3.1: Calculating the predictability metrics for a tropical forest and dry shrubland. The green bars show the IAV of GPP and the red bars the ensemble variability in lead year one. The predictable component (pc) is the absolute predictable IAV, and is useful to assess the predictability of atmospheric CO_2. pc is generally higher in regions with high IAV. pf is pc scaled by IAV and allows assessing the memory of an ecosystem.

Results

The six ESMs are fairly similar in their ability to retain memory (pf). The pf of GPP is between 19% and 24% in four out of six ESMs. However, it is not just the total pf which is similar

among the ESMs, there is also high consistency in the role of the environmental drivers in providing the memory to the system. While around 26% of the IAV caused by soil moisture is predictable, it is only 9% for the IAV caused by radiation. This reveals the key role of moisture availability: Predictability is highly sensitive to soil moisture regime and increases sharply from an energy-limited to water-limited evapotranspiration. This mechanism is likely to cause the overall low pf of GPP in MPI-ESM-LR. The GPP IAV caused by radiation is 20% higher in MPI-ESM-LR than in other ESMs, leading to a high fraction of poorly predictable IAV.

ESMs have similar memory retention

The ESMs have substantial differences in their patterns of GPP IAV. Several ESMs have unique hotspots responsible for a large fraction of their GPP IAV, which are not present in other ESMs. To quantify this disagreement, I define the top 20*th* percentile of GPP IAV grid cells as high variability areas. These high variability areas are shown in Figure 3.2 for the six ESMs and two observational products. Half of the high variability grid cells can only be found in one of the products. There is a large disagreement on the role of Australia, South Africa, and central South America. Besides the spatial mismatch, there is disagreement in the drivers of IAV. The main driver of global GPP IAV is temperature in some ESMs and soil moisture in others. Likely reasons for the differences in IAV patterns are differences in meteorological variability, the sensitivity of carbon fluxes to climate, and phenology (Anav et al., 2015; Peano et al., 2021; Piao et al., 2020).

Spatial mismatch in IAV patterns

Patterns of meteorological variability can be very specific to ESMs (Zhu and Yang, 2021). I examined the sensitivity of GPP to soil moisture IAV in Australia and Southern Africa, the regions with the highest uncertainty of GPP IAV. The ESMs with the highest GPP IAV in these regions do not necessarily have high IAV of soil moisture. From this, I conclude that the above-average GPP IAV in Australia and Southern Africa is not caused by a high variability of meteorological input, but by a high sensitivity of GPP to soil moisture variability.

Due to the differences in IAV patterns, the areas that contribute to the predictability of CO_2 (pc) also differ among ESMs. From these high predictability grid cells (top 20*th* percentile of pc), 74% are unique to only one ESM, and less than 8% of high predictability grid cells occur in three or more ESMs.

Differences in IAV limit predictability

So why is the predictive skill of atmospheric CO_2 comparable among ESMs, despite these fundamental differences in

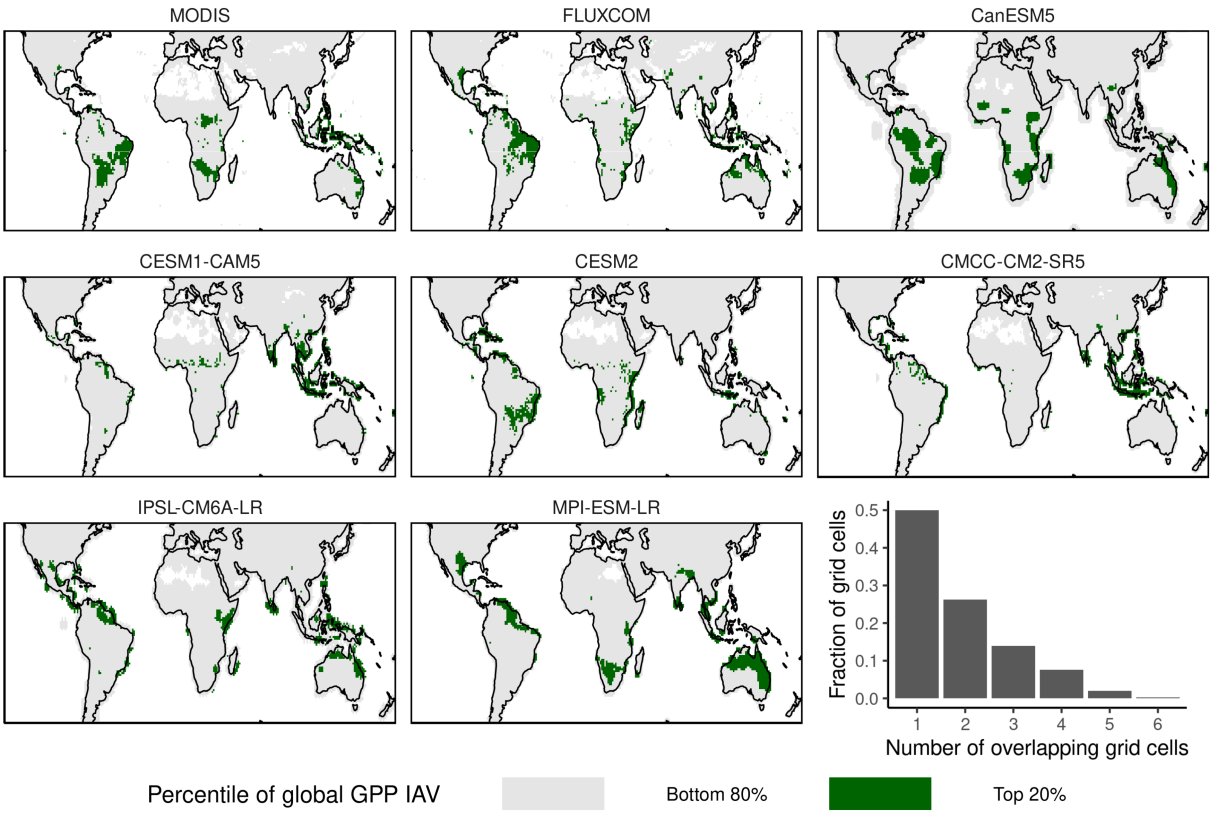

Figure 3.2: The area responsible for the top 20th percentile of GPP variability in MODIS, FLUXCOM and six ESMs. The frequency distribution of the number of overlapping grid cells is shown in the bar chart. More than half of the top 20th percentile grid cells are unique to one model and do not have any overlap.

ENSO – the great equalizer

GPP IAV? For one, although the locations of IAV hotspots differ, the predictable fraction of IAV is similar across the ESMs. This means that anomalies already present at the start of the simulation will have a similar predictability. Another reason for the similar predictive skill of atmospheric CO_2 is ENSO. The ENSO-related climate patterns are often simulated with differences among ESMs (Beobide-Arsuaga et al., 2021; Tedeschi and Collins, 2016). These ENSO-related climate patterns contribute to the observed deviations in GPP IAV. From the CO_2 perspective, however, it does not matter where the ENSO-related GPP patterns are: An El Niño year will create predominantly warm and dry conditions somewhere in the tropics – leading to reduced global GPP. As long as the SST patterns of ENSO are predicted sufficiently, the anomaly of accumulated carbon fluxes

will be similar among ESMs, even if the anomalies originate from different regions.

Conclusions

The ESMs are similar in their ability to predict themselves, suggesting that the processes which provide memory are represented similarly in all ESMs. However, several land surface processes which control GPP remain poorly constrained. As a result, there are large differences in the spatial patterns of GPP IAV among ESMs that drive differences in the predictability patterns. The differences in IAV are driven by differences in the limiting factors of GPP and how sensitive GPP is to these factors. From the atmospheric perspective, the implication is that the ups and downs in CO_2 are caused by different regions and for different reasons. The inability of ESMs to reproduce the IAV of GPP also reveals that there are regions where potential predictability does not resemble the actual predictive skill. Further work on improving the predictability of the terrestrial carbon cycle ought therefore rather to focus on the processes creating variability, than on the processes providing predictability.

4

ENSO-INDUCED VARIABILITY PATTERNS

ENSO as a driver of global GPP

The relationship between ENSO and atmospheric CO_2 observations at Mauna Loa was first discovered by Bacastow (1976). Altered atmospheric circulation patterns during El Niño events cause warm and dry conditions across the tropics, leading to a reduction of GPP (Qian, Joseph, and Zeng, 2008). ENSO has a significant impact on the GPP of 32% of the vegetated land area and can explain up to 26% of interannual variation of global GPP (Zhang et al., 2019). El Niño events can be severe enough to turn the Amazon Basin, a carbon sink of global importance, into a net source of carbon (Tian et al., 1998).

ENSO as a chance for predictability

But not only does ENSO play a large role in the terrestrial carbon cycle, it is also the main source of predictability (Manzanas et al., 2014; Zeng et al., 2008). Global carbon fluxes lag behind ENSO by around five months (Qian, Joseph, and Zeng, 2008), meaning that even without further knowledge on the evolution of ENSO, we are able to restrict GPP variability based on present observations. On top of this lag effect, simulations starting in winter can predict ENSO for around one year (Barnston et al., 2019).

Further memory is added to the system by the land surface, which prolongs the ENSO-induced climatic anomalies. The larger the climatic anomaly, the longer it will take for soil moisture conditions to return to normality – and ENSO years are described as "spectacular" or "catastrophic" and can be among the most extreme years of variability (Holmgren et al., 2001). Large anomalies also increase the chances of increased predictability due to the synchronization of ensemble members at the saturated or depleted state.

Even longer predictability mechanisms might be triggered through vegetation dynamics (Holmgren et al., 2001). This can happen in dry years through the lasting impact of defoliation and tree mortality (Santos et al., 2018; Wigneron et al., 2020), or through wildfire, which requires decades of recovery (Silva et al., 2018). Wet events, on the other hand, can cause excess plant growth that exhausts the carrying capacity of ecosystems, leading to lasting degradation (Zhang, Keenan, and Zhou, 2021). Not yet implemented in ESMs, but with a great potential for

long-term predictability, is plant recruitment in semi-arid ecosystems (Holmgren et al., 2001). Extreme events play a crucial role in the vegetation dynamics of these ecosystems, where the establishment of trees and shrubs needs sustained wet conditions (Holmgren et al., 2001).

I showed in Chapter 3 that the limiting factor of GPP predictability is in the uncertainty of IAV patterns. Now we have to ask how ENSO – one of the largest drivers of carbon flux IAV – contributes to these uncertainties. The teleconnections of ENSO create a patchwork of diverse climatic anomalies, with most continents having regions of increased and decreased plant growth during a single event (Holmgren et al., 2001; Zhang et al., 2019). As ENSO provides a unique chance of predictability, it is particularly important that these spatial patterns of ENSO-induced GPP anomalies are reproduced well by ESMs (Manzanas et al., 2014).

ENSO intercomparison

With this work, I want to quantify the deviations in ENSO-induced GPP anomalies among ESMs and determine the causing factors of these deviations:

1. **How much do the ENSO-induced GPP anomalies differ among ESMs?**

2. **Are the differences due to climate forcing or due to the sensitivity of GPP to climate?**

Using control simulations for large ENSO sample size

To study the relationship between ENSO, soil moisture and GPP, I use unforced control simulations of 17 CMIP6 (Coupled Model Intercomparison Project Phase 6) ESMs. The ESMs are compared with results from upscaled flux tower measurements (FLUXCOM version RS + METEO, Jung et al. 2019) and SST reanalysis data (HadISST, Rayner et al. 2003).

ENSO and global GPP

The sensitivity of global GPP to a 1°C SST anomaly in the Niño3.4 region is between -0.7 and -2.4 PgC yr^{-1} in the ESMs (Fig. 4.1). However, some of the differences in GPP sensitivity among the ESMs are balanced by differences in ENSO amplitude. The IAV of Niño3.4 SST tends to be higher for the models with a low sensitivity, leading to larger events in these ESMs. The mean IAV of Niño3.4 SST is close to the observed standard deviation of 0.75°C, while the FLUXCOM GPP sensitivity of -0.2 PgC yr^{-1} is below the ESM mean. However, this is in accordance with the underestimation of GPP IAV by FLUXCOM, as described in chapter 1.2.

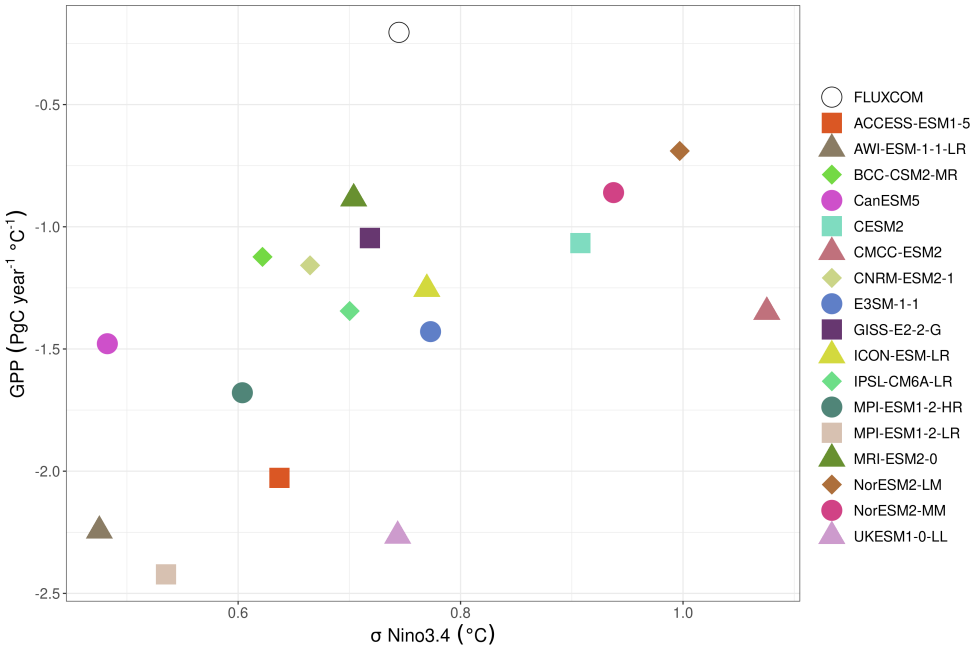

Figure 4.1: ENSO strength and sensitivity of global GPP to ENSO in 17 ESMs and FLUXCOM. A correlation between ENSO amplitude (x axis) and GPP sensitivity to ENSO (y axis) is balancing some of the differences between ESMs.

ESMs disagree on the role of the two major ENSO regions

The large overall differences in the effect of ENSO on GPP make it difficult to compare the differences in spatial patterns. To make this comparison feasible, I create a composite of El Niño events for all ESMs and FLUXCOM, and scaled the results to the same total GPP anomaly. I use the IPCC climate reference regions to quantify the spatial differences (Iturbide et al., 2020). Figure 4.2 shows the GPP anomalies of the scaled El Niño events in the six reference regions with the largest deviations among the ESMs. The largest GPP anomalies and deviations between the models are in Southeast Asia (SEA) and Northern South America (NSA). These two regions are responsible for 58% of the global GPP anomalies, but the values of individual ESMs range between 26% and 75%. GPP anomalies in both regions have large deviations among the ESMs, with a standard deviation of around 50% of the mean anomalies. Although the mean ESM anomaly of SEA is 42% larger than the mean anomaly in NSA, five of the 17 ESMs have larger anomalies in NSA than SEA.

ENSO drives climate – climate drives GPP

What is causing these large deviations in the ENSO-induced GPP anomalies? To answer this question, I examine the two consecutive processes that determine the size of the GPP anomalies: How large are the ENSO-induced climate anomalies, and how

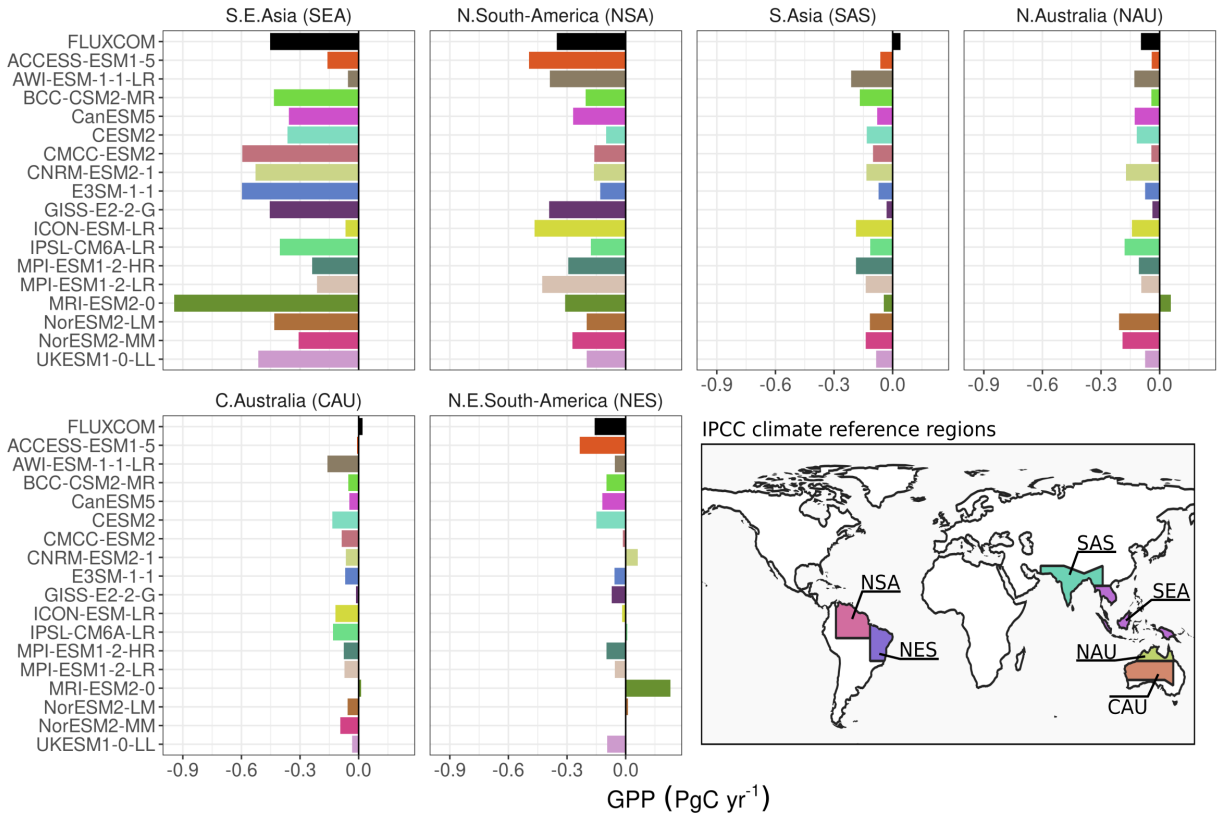

Figure 4.2: GPP anomalies of an El Niño event in the six regions with the highest deviations among ESMs. All events are scaled to a total of -1 PgC. The boundaries of the regions are shown on the map.

sensitive is GPP to climatic anomalies. Soil moisture anomalies are used here to substitute climatic anomalies because they correlate well with precipitation and temperature. I use regression analysis to calculate the soil moisture anomalies caused by a 1°C warming in the Niño3.4 region and the GPP sensitivity to a 1 kg soil moisture anomaly.

Causes of spatial mismatch

Although there are small regional differences, both processes contribute equally to the variations in ENSO-induced GPP anomalies. On the global average, ENSO-induced climate anomalies and GPP sensitivity have similar variations among the ESMs. To determine the biases of individual ESMs in these two processes, I scale the results by regions, so that the sensitivities are not dominated by the region with the strongest anomalies. Figure 4.3 shows the scaled biases of ENSO-induced climate anomalies and GPP sensitivity among the ESMs (this Figure shows absolute scales – high values mean a strong reaction in either direction). The balancing effect is also present here, as there

is a negative correlation between ENSO climatic anomalies and GPP sensitivity. In the extremes, we find UKESM1-0-LL, which has both strong ENSO climate anomalies and GPP sensitivity, and E3SM-1-1, which is on the low end of the spectra.

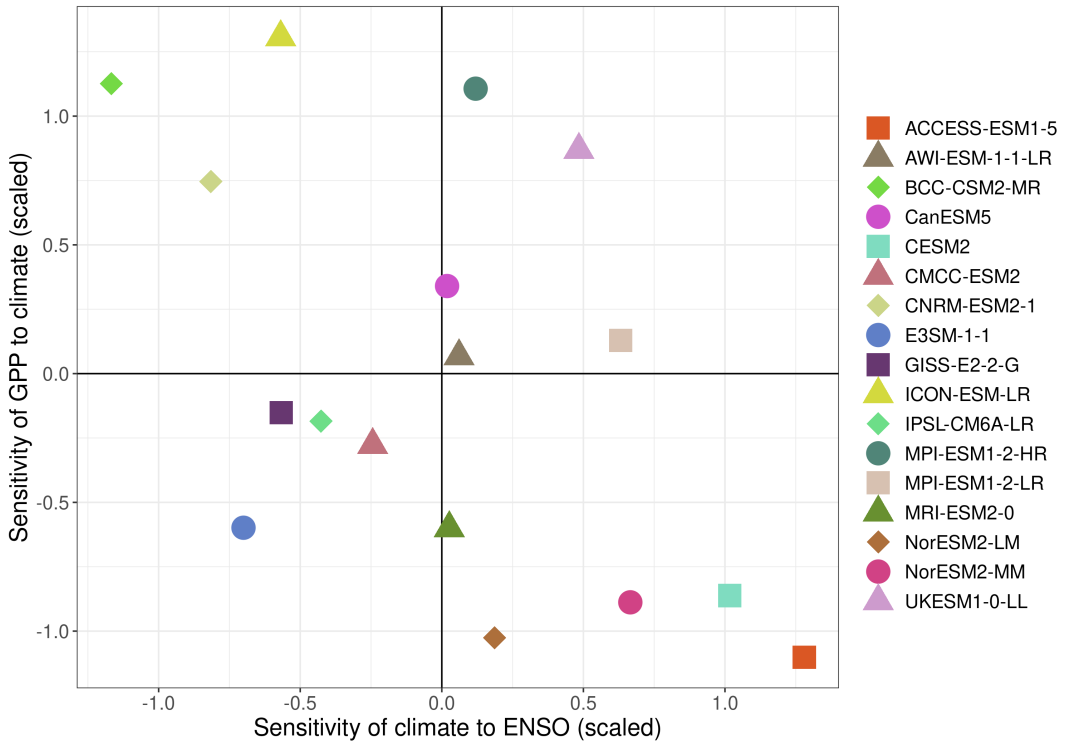

Figure 4.3: Biases of 17 ESMs in their reproduction of the ENSO-GPP relationship. The x axis shows the scaled sensitivity of climate anomalies to ENSO and the y axis the scaled sensitivity of GPP to climate anomalies.

Why ENSO patterns matter for predictability

All tested ESMs are capable to predict globally accumulated ENSO-related GPP anomalies, given the predominantly warm and dry (cold and wet) conditions that prevail during El Niño (La Niña). There is, however, a substantial disagreement in the regions contributing to these anomalies. Large uncertainties are on the role of SAE and NSA, which are caused by model biases in the strength of ENSO-induced climate anomalies and the sensitivity of GPP to climate. The advantage of fully coupled ESM simulations is the integration of initial conditions and the interaction between the land and the atmosphere. However, the interaction of ENSO with initial conditions becomes misleading, if the ENSO-induced anomalies are not where they are supposed to be. In the worst case, this makes ESMs no better than statistical models in predicting atmospheric CO_2. Statistical models

have much lower resource requirements than ESMs, and predict atmospheric CO_2 by using an ENSO forecast and the observed relationship between ENSO and atmospheric CO_2 (Betts et al., 2016).

Broader implications of differing ENSO patterns

Another problem with the mismatch of ENSO patterns is the different response mechanisms of the affected ecosystems. Most of the ENSO anomalies are in the tropics but fall in a wide range of moisture regimes. The key ENSO regions analysed here have tropical rainforest, tropical savanna, steppe, and desert (Iturbide et al., 2020). Because these biomes differ in the factors which limit GPP, they also differ in the immediate reaction to the anomalies. But more importantly, the long-term effects of the ENSO anomalies are also determined by the biomes under their influence. El Niño events in SEA are more likely to cause disturbance by wildfire than in NSA (Le Page et al., 2008; Liu et al., 2017), leading to long recovery times in the affected regions. Similarly, the duration of ENSO anomalies is determined by the water-holding capacity and soil moisture memory of the regions receiving the anomalies. This effect can cause a discrepancy between potential predictability and actual predictive skill. Potential predictability is artificially inflated if the ENSO anomalies fall into regions with a naturally high soil moisture memory, or vice versa.

The benchmark potential of ENSO

To summarize, there are differences in the patterns of ENSO-induced GPP anomalies, and these differences have large implications on the predictability of the terrestrial carbon cycle. However, these differences can be seen as an untapped potential to benchmark and constrain the terrestrial carbon cycle. While we still lack observations that reproduce the IAV of the global carbon cycle, quantifying the large-scale patterns of ENSO-induced carbon fluxes is a more achievable goal. The data presented here provide information on the model biases that are hindering the reproduction of these large-scale ENSO-induced GPP patterns.

5

SUMMARY AND CONCLUSIONS

In this chapter, I summarize the research questions and key findings of my work. Afterwards, we take a step back, to look at the overall picture and identify the challenges and opportunities in the field.

MECHANISMS OF PREDICTABILITY

1st research topic

Previous studies identified that carbon flux predictability has spatial and temporal variability. Carbon fluxes are controlled by a variety of environmental drivers, but we do not yet understand the role of the individual drivers in providing carbon flux predictability and the variability of predictability. To analyse the mechanisms explaining the variations in predictability, I ask:

1. **How do the environmental drivers of carbon fluxes contribute to the patterns of carbon flux predictability?**

Spatial patterns of carbon flux predictability can often be attributed to one or two drivers. There are hotspots of carbon flux predictability, which are exclusively driven by the predictability of soil moisture or temperature.

2. **What mechanisms explain the seasonal variability and IAV of carbon flux predictability?**

I found that seasonal patterns of carbon flux predictability are caused by the changing limiting factors of carbon fluxes and because the environmental drivers differ in their predictability. The driver that limits a carbon flux passes on its predictability to the carbon flux. This establishes the idea that carbon flux predictability depends on the sensitivity of carbon fluxes to their drivers.

The IAV of carbon flux predictability is caused by hydrological conditions. Extreme climate conditions will lead to the synchronization of ensemble members in the saturated or depleted state. This reduces ensemble variability and increases carbon flux predictability.

2nd research topic

DRIVERS OF VARIABILITY

How much a region contributes to the predictability of CO_2 depends on the IAV of carbon fluxes, and how much of this IAV is predictable. In Chapter 2 we discussed how much of the carbon flux IAV can be predicted, but we have not considered the differences in IAV patterns yet. The IAV of GPP is poorly constrained, which raises the question of how much this affects predictability patterns. I analyse six ESMs to ask:

1. **What drives the differences in carbon flux predictability among ESMs?**

The studied ESMs are similar in the fraction of GPP IAV they can predict. Yet, there are differences in the regions which contribute to the predictability of CO_2. This is caused by differences in the spatial patterns of GPP IAV. The mismatch of IAV patterns is due to the different sensitivities of GPP to environmental drivers.

2. **How it is possible that the predictive skill of atmospheric CO_2 is similar among ESMs (Ilyina et al., 2021), while there are large uncertainties in the key processes controlling terrestrial carbon flux IAV?**

Although the ESMs differ in the regions contributing to CO_2 predictability, they can agree on what fraction of GPP IAV is predictable. This allows them to produce similar predictions due to two reasons:

- The anomalies in the initial conditions lead to similar predictabilities.
- The ESMs can predict global climate modes like ENSO. These climate modes produce global climate anomalies. The ENSO-induced climate patterns do not have to be similar among the ESMs to produce a coherent signal in atmospheric CO_2.

3nd research topic

ENSO-INDUCED VARIABILITY PATTERNS

ENSO is an integral part of the terrestrial carbon cycle. It drives the IAV of the global carbon cycle and offers multiple opportunities for predictability. However, the ability of ESMs to reproduce

ENSO teleconnections is limiting the predictive potential. I compare the role of ENSO on GPP in 17 CMIP6 ESMs to find out:

1. **How much do the ENSO-induced GPP anomalies differ among ESMs?**

There is a substantial difference in the ENSO-induced GPP patterns. The largest GPP anomalies are in Southeast Asia and northern South America. However, the total anomalies of these two regions range between 26% and 75% of global ENSO-related GPP anomalies among the 17 ESMs. There is also no unanimity on which region has the largest anomalies.

2. **Are the differences due to climate forcing or due to the sensitivity of GPP to climate?**

I simplify the cause of ENSO-related GPP anomalies as a two-step process: ENSO creates climatic anomalies, and GPP reacts to climatic anomalies. Both of these processes contribute equally to the uncertainty in the ENSO-related GPP patterns. The resulting data provides information on ESM biases.

CONCLUSIONS

With this work, I tested the ability of ESMs to predict the terrestrial carbon cycle. The two major topics I addressed are what mechanisms provide the memory, and how well is IAV of carbon fluxes is reproduced.

Memory

Focusing on the key regions

The two sources of memory in the system are climate predictability and land surface processes that prolong anomalies. Although the climate system is largely chaotic, there are certain regions with established predictability. These are the regions with ENSO teleconnections, northern South America, Australia, and some other parts of the tropics (Manzanas et al., 2014). The predictability from land surface processes is also not spread evenly. Australia and Southern Africa are hotspots of soil moisture driven predictability. To utilize the predictive performance of the earth system, these key regions ought to be in the focus of model parameterization.

Utilizing vegetation dynamics

Another land surface process with the potential to increase memory are long-term vegetation dynamics. Specifically, the

large and structural changes like mortality and recruitment. These processes only occur in extreme years and cause shifts in ecosystem states with long-lasting effects. Implementing these processes accurately in ESMs would allow ESMs to reproduce the low-frequency IAV of vegetation dynamics, thereby extending predictability.

Variability

I showed that carbon flux predictability is limited by the reproduction of carbon flux IAV. The largest differences appear in the semi-arid tropics. The role of semi-arid ecosystems in the global carbon cycle was known since the early 2000s (Knapp and Smith, 2001). But it was not until 2015 that the spotlight of the land carbon community was put on this topic with the pivotal publication by Anders Ahlström and colleagues:

Constraining semi-arid regions

> *Semi-arid regions have been the subject of relatively few targeted studies that place their importance in a global context. Our findings indicate that semiarid regions and their ecosystems merit increased attention as a key to understanding and predicting interannual to decadal variations in the global carbon cycle.*
>
> — Ahlström et al. (2015)

Although semi-arid ecosystems have started to receive more attention, they remain the least constrained ecosystems (Chen et al., 2017). A likely cause for these mismatches is the low number of flux towers in the semi-arid tropics (Zhang and Ye, 2021). Most measurements are based in non-water-limited (mesic) ecosystems. The discrepancies are created by applying the mechanisms studied in mesic environments to semi-arid ecosystems (Grünzweig et al., 2022). However, semi-arid ecosystems are governed by several dryland mechanisms that are not present in mesic ecosystems (Grünzweig et al., 2022). Consequently, we need a better quantification of semi-arid carbon fluxes and the implementation of necessary dryland mechanisms.

Predictability in a changing climate

But improving our understanding of semi-arid ecosystems is not only important because of their high IAV. As semi-arid ecosystems are spreading under climate change (Denissen et al., 2022), dryland mechanisms will become relevant in regions currently not limited by water (Grünzweig et al., 2022). How all of these changes will affect the predictability of the carbon cycle is yet unknown. On the one hand, we observe a widespread

shift from energy-limited to water-limited evapotranspiration (Denissen et al., 2022). This can increase predictability by shifting carbon flux sensitivity away from the less predictable radiation towards more predictable soil moisture. On the other hand, climate change increases the frequency of unpredictable extreme events (Harris et al., 2018). Extreme events have a disproportionally large role on the global carbon cycle, with few extreme events driving the global anomalies (Zscheischler et al., 2014).

The final limitation to predicting atmospheric CO_2 is the chaotic nature of weather and climate. Once this limitation is reached, further advancements will be infinitesimal. But currently, we are limited by the variability of terrestrial carbon fluxes. However large these uncertainties may be, we already have the tools to constrain them. This indicates that the potential to predict atmospheric CO_2 is not exploited yet.

APPENDIX

A

PROCESS-BASED ANALYSIS OF TERRESTRIAL CARBON FLUX PREDICTABILITY

The work in this appendix has been published as:

Dunkl, I., A. Spring, P. Friedlingstein, and V. Brovkin (2021). "Process-based analysis of terrestrial carbon flux predictability." *Earth System Dynamics* 12.4, pp. 1413–1426.

Author contributions:
ID and VB conceived the study. ID performed the simulations and analysis, created the figures and drafted the manuscript. AS, PF, and VB contributed to manuscript editing and providing feedback.

Data availability:
The data and scripts to reproduce this analysis are archived at http://hdl.handle.net/21.11116/0000-0009-7256-6

Process-based analysis of terrestrial carbon flux predictability

István Dunkl[1,2], **Aaron Spring**[1], **Pierre Friedlingstein**[3], **and Victor Brovkin**[1,4]

[1]Max Planck Institute for Meteorology, Hamburg, Germany
[2]International Max Planck Research School on Earth System Modelling, Hamburg, Germany
[3]College of Engineering, Mathematics and Physical Sciences, University of Exeter, Exeter, UK
[4]Center for Earth System Research and Sustainability, University of Hamburg, Hamburg, Germany

Received: 3 June 2021 – Revised: 24 September 2021
Accepted 4 October 2021 – 2 December 2021

Abstract

Despite efforts to decrease the discrepancy between simulated and observed terrestrial carbon fluxes, the uncertainty in trends and patterns of the land carbon fluxes remains high. This difficulty raises the question of the extent to which the terrestrial carbon cycle is predictable and which processes explain the predictability. Here, the perfect model approach is used to assess the potential predictability of net primary production (NPPpred) and heterotrophic respiration (Rhpred) by using ensemble simulations conducted with the Max Planck Institute Earth system model. In order to assess the role of local carbon flux predictability (CFpred) in the predictability of the global carbon cycle, we suggest a new predictability metric weighted by the amplitude of the flux anomalies. Regression analysis is used to determine the contribution of the predictability of different environmental drivers to NPPpred and Rhpred (soil moisture, air temperature, and radiation for NPP, and soil organic carbon, air temperature, and precipitation for Rh). Global NPPpred is driven to 62 % and 30 % by the predictability of soil moisture and temperature, respectively. Global Rhpred is driven to 52 % and 27 % by the predictability of soil organic carbon and temperature, respectively. The decomposition of predictability shows that the relatively high Rhpred compared to NPPpred is due to the generally high predictability of soil organic carbon. The seasonality in NPPpred and Rhpred patterns can be explained by the change in limiting factors over the wet and dry months. Consequently, CFpred is controlled by the predictability of the currently limiting environmental factor. Differences in CFpred between ensemble simulations can be attributed to the occurrence of wet and dry years, which influences the predictability of soil moisture and temperature. This variability of predictability is caused by the state dependency of ecosystem processes. Our results reveal the crucial regions and ecosystem processes to be considered when initializing a carbon prediction system.

A.1 INTRODUCTION

As a net sink for atmospheric CO_2, terrestrial ecosystems absorb around one-third of the anthropogenic emissions (Friedlingstein et al., 2020). Carbon fluxes between the land–atmosphere interface have a high interannual variability with a standard deviation (SD) of 0.7 $PgC\,yr^{-1}$ (Sitch et al., 2015) and cause the majority of the atmospheric CO_2 fluctuations (Ciais et al., 2013; Spring, Ilyina, and Marotzke, 2020). The high variability of terrestrial carbon fluxes can be attributed to the sensitivity of land surface processes to climatic drivers; however, the relative importance of temperature and precipitation are still debated (Bastos et al., 2018; Beer et al., 2010; Bloom et al., 2016; Fang et al., 2017; Jones et al., 2001; Jung et al., 2017). In accordance with the limited understanding of carbon flux variability, models are not able to fully reproduce the spatiotemporal patterns of the terrestrial carbon cycle. This is reflected in the poor representation of soil organic carbon (SOC) in Earth system models (ESMs), the inability to adequately model gross primary production (GPP) from eddy covariance flux tower sites (Luo, Keenan, and Smith, 2015), and the difficulty to detect the efforts taken in emission reduction due to internal variability of atmospheric CO_2 variability (Spring, Ilyina, and Marotzke, 2020). In order to produce more realistic predictions, efforts in model development have been directed towards using observations to constrain model parameters (Bloom et al., 2016; Chadburn et al., 2017; Mystakidis et al., 2016; Tziolas et al., 2020; Zeng et al., 2014) and to refine model structure to incorporate more processes and interactions (Krull, Baldock, and Skjemstad, 2003; Luo et al., 2016; Stockmann et al., 2013; Xu et al., 2014). While efforts in model development are continuing to narrow the gap between the simulated and observed carbon cycle, the lack of progress in improving the predictive ability of the models raises the question of the extent to which the terrestrial carbon cycle is predictable at all (Luo, Keenan, and Smith, 2015).

The potential predictability of a system can be estimated by using the perfect model framework. Ensemble simulations are initialized along a control run with each member of the ensemble having slightly perturbed initial conditions. The upper limits of predictability are then derived by analysing the divergence of the ensemble simulations. This method assumes (a) perfect model physics which are able to reproduce the full spectrum of natural variability and (b) perfect knowledge of the modelled

system and a model whose representation of the real world is "perfect enough" (Boer, Kharin, and Merryfield, 2013). Séférian, Berthet, and Chevallier (2018) used the perfect model framework to assess the potential predictability of terrestrial carbon fluxes (CFpred) at annual time steps. They estimated the predictive horizon of terrestrial carbon fluxes to be two years globally and up to three years in northern latitudes. The high variability of predictability among different initializations suggests a state dependence of CFpred, but no further mechanisms of predictability were investigated therein. Multiple processes can be regarded as the sources of CFpred. Due to the high sensitivity of the terrestrial carbon cycle to climate, climate predictability provides carbon fluxes with a basic prediction horizon. The main contributor to climate predictability is El Niño–Southern Oscillation (ENSO), which explains over 40 % of the variability in global net primary production (NPP) (Bastos et al., 2013) and a large fraction of CFpred (Zeng et al., 2008). El Niño events are associated with high temperatures and low precipitation in the tropics which cause a reduction of the land carbon sink of $1.8\,\mathrm{PgC\,yr^{-1}}$ per 1°C sea surface temperature (SST) anomaly in the Niño 3 region (Jones et al., 2001). This strong relationship between SST and the carbon cycle was used by Betts et al. (2016) to predict annual CO_2 growth. Their statistical model uses the annual average SST in the Niño 3.4 region to successfully predict the CO_2 rise with a precision of $0.53\,\mathrm{ppm\,yr^{-1}}$. Furthermore, Spring and Ilyina (2020) showed that ESM-based initialized predictions can predict atmospheric CO_2 variations up to three years in advance.

However, CFpred is extended beyond the predictability of climate by slowly varying land surface processes that filter out the high-frequency noise of the climate signal. As the most prominent process, soil moisture memory is known to increase the predictability of temperature (TEMPpred) and precipitation (PRECIPpred) by several months (Chikamoto et al., 2015), but memory can also be attributed to phenology (Weiss et al., 2014) and SOC (Lovenduski et al., 2019). Besides the slowly changing land state variables, the memory is further extended through land–atmosphere coupling which propagates soil anomalies back to the atmosphere by energy and water fluxes (Bellucci et al., 2015).

Previous studies that focus on the mechanisms of CFpred investigated the role of various land processes and how they contribute to the overall CFpred. Weiss et al. (2014) found in-

creased predictability of evaporation and to some extent temperature due to a dynamic simulation of leaf area index (LAI), which would also extend CFpred. The role of land surface initialization in CFpred was studied by Zeng et al. (2008) and Lovenduski et al. (2019). Zeng et al. (2008) isolated the fraction of CFpred which is based solely on initial conditions and compare fully coupled dynamic simulations with statistical models. Lovenduski et al. (2019) quantified the degree to which CFpred improves when the land surface is initialized. They also assessed the relative importance of the individual land surface processes for the variability of terrestrial carbon fluxes and found that CFpred depends on the correct initialization of vegetation carbon biomass and soil moisture rather than temperature. These studies have shown the significant advantage of dynamic forecasting systems, suggesting CFpred extends beyond the predictability of the forcing variables due to land surface processes. However, these studies were not focused on the contributions of individual drivers of carbon fluxes to CFpred or on processes responsible for maintaining CFpred.

Here, we use perfect model simulations conducted with an ESM to investigate the structure and mechanisms of the CFpred. Initialized ensemble simulations are created from a range of ENSO states. Analysed are the carbon fluxes with the highest contribution to the interannual variability of the land–atmosphere CO_2 exchange. These are NPP with an interannual SD of 0.99 PgC yr^{-1} and heterotrophic respiration (Rh) with an SD of 0.29 PgC yr^{-1} (Wang, Zeng, and Wang, 2016). The potential predictability of NPP (NPPpred) and Rh (Rhpred) is derived from the rate of divergence within the ensemble members. We evaluate the predictability data to find how NPPpred and Rhpred differ in their spatiotemporal patterns and variability. Lastly, we identify the key drivers of NPP and Rh and determine their contribution to NPPpred and Rhpred. We use this framework to explain the attained spatiotemporal patterns of CFpred and identify the underlying land system processes producing these patterns.

A.2 METHODS

A.2.1 *Earth system model*

This study is based on the output of the MPI-ESM version 1.2 developed for the Coupled Model Intercomparison Project 6

(Mauritsen et al., 2019). The model runs fully coupled in the LR configuration that uses the atmospheric component ECHAM 6.3.05 with a T63 spatial truncation and 47 atmospheric layers. The atmospheric model is directly coupled with the land model JSBACH 3.20 and uses an interactive carbon cycle, which means atmospheric CO_2 reacts to land and ocean carbon fluxes.

A.2.2 *Predictability metrics*

The control simulation used in this study is a 1000-year unforced simulation with a preindustrial CO_2 concentration of 285 ppm. A total of thirty-five 10-member ensemble simulations are initialized, each starting in January with a run time of two years. The unperturbed simulation of the control run is added to the ensembles as the 11th member. Initialization dates are selected manually in order to attain a diversity of ENSO states. The selected dates are grouped into three categories: El Niño, La Niña, or ENSO-neutral.

The potential predictability is assessed by using a correlation-based and a distance-based metric. The anomaly correlation coefficient (ACC) is a commonly used metric to measure forecast skill (Jolliffe and Stephenson, 2012) which calculates the correlation between predicted and observed anomalies as

$$\mathrm{ACC}_{j,t} = \frac{\mathrm{cov}(f, o)}{\sigma_f \cdot \sigma_o}, \tag{A.1}$$

where j and t are grid cell and lead time, cov is the covariance, and f and o are the forecast and validation anomalies. Similar to Collins and Sinha (2003) and Becker, Dool, and Peña (2013), the noise in the ACC is reduced by averaging over several ACC values. This is achieved by taking all 11 ensemble members as the validation in turn, while the mean of the remaining ensemble members serves as the forecast. Although the ACC is an intuitive metric which is calculated from all initializations and thus provides a robust estimation of the predictability, it does not allow us to investigate the variability of predictability between initializations. The comparison of predictabilities between initialization is achieved by the use of a distance-based metric which is computed for all initializations individually. The distance-based metric used here is the normalized ensemble variance ($V(t)$) based on the method proposed by Griffies and

Bryan (1997). Predictability is defined as the ensemble variance normalized by the variance of the climatology as

$$V(t) = \frac{\frac{1}{M}\sum_{i=1}^{M}\left[X_i(t) - \overline{X}(t)\right]^2}{\sigma^2}, \tag{A.2}$$

where t is lead time, M the number of ensemble members, X_i the ith member, $\overline{X}$ the ensemble mean, and σ^2 the variance of the control simulation. In this study, the complement of the normalized ensemble variance is used as $V_c(t) = 1 - V(t)$. The resulting metric indicates perfect predictability at a value of 1 and an ensemble spread that exceeds the climatological variance for values below zero.

While ACC and V_c allow the estimation of regional predictability, these metrics are not suitable to evaluate the impact of local predictabilities on the predictability of the global carbon cycle. This is due to the disregard of the flux amplitude in the calculation of the metrics. Both of the metrics are prone to producing above-average predictabilities in regions where carbon fluxes are generally low or even close to zero, such as subtropical deserts. Here we propose a weighted predictability metric that allows us to assess local predictabilities with regard to their impact on the predictability of the global carbon cycle. V_c is weighted by using an approach similar to risk assessment, which is calculated as the product of likelihood and impact. Here a weighted predictability wV_c is calculated by multiplying V_c with the absolute carbon flux anomaly of the ensemble mean:

$$wV_c(t) = V_c(t) \times |\Delta\mathrm{FLUX}(t)|. \tag{A.3}$$

A.2.3 *Decomposition of predictability*

In order to investigate the drivers of CFpred, the V_c of NPP and Rh are decomposed into components contributing to the predictability of these fluxes similar to an approach used by Jung et al. (2017). They used regression analysis to determine the contribution of environmental variables to the anomalies in GPP and ecosystem respiration. Here the assumptions of Jung et al. (2017) are extended from carbon flux anomalies to CFpred: a high CFpred needs to be caused by a high predictability of one or more of its driving environmental variables. Using this assumption, NPPpred and Rhpred are modelled as the response to the predictability of the individual environmental drivers. Regression analysis is used to determine the contribution of the

predictability of the environmental variables to NPPpred and Rhpred. The drivers of NPPpred are selected following the drivers of GPP in Jung et al. (2017) as two layers of soil moisture (midSOILpred for 19–78 cm depth and deepSOILpred for 79–268 cm depth), air temperature (TEMPpred), and photosynthetically active radiation (PARpred). The drivers of Rhpred are based on the rate-modifying factors used in JSBACH to calculate Rh, which are TEMPpred, PRECIPpred, and SOCpred. Although precipitation has no direct relationship with Rh, the Rh submodel used in JSBACH is parameterized using precipitation because of its strong relationship with moisture in the uppermost soil layer where most of the respiration takes place. Instead of SOC, the content of the aboveground acid-hydrolysable carbon pool (here referred to as SOC) is used as a surrogate variable. The contribution of the predictability of the environmental drivers to the CFpred is calculated as

$$V_{\mathrm{c}}\mathrm{FLUX}_{j,t,i} = \sum_{k} \left[a_{j,t}^{\mathrm{DRI}_k} \times V_{\mathrm{c}}\mathrm{DRI}_{k,j,t,i} \right] + \epsilon_{j,t,i}, \tag{A.4}$$

with V_{c}FLUX being the complementary normalized ensemble variance of NPP or Rh, a^{DRI_k} the coefficient of the kth driver (for example TEMPpred), V_{c} DRI the predictability of the kth driver, and ϵ the residual error term. Grid cell, lead time, and initialization are denoted by the indices j, t, and i. The regression coefficients are calculated by using non-negative least squares (Mullen and Stokkum, 2012) for every grid cell and lead time by using the data from all initializations. After fitting the regression model to the data, the individual components of CFpred are calculated as

$$V_{\mathrm{c}}\mathrm{FLUX}_{i,t,s}^{\mathrm{DRI}_k} = a_{i,t}^{\mathrm{DRI}_k} \times V_{\mathrm{c}}\mathrm{DRI}_{k,i,t,s}, \tag{A.5}$$

where $V_{\mathrm{c}}\mathrm{FLUX}^{\mathrm{DRI}}$ describes the amount of predictability of FLUX that can be attributed to the driver k.

A.3 RESULTS AND DISCUSSION

Out of the 35 ensemble simulations initialized along the control run, 7 simulations are part of the El Niño and 8 simulations are part of the La Niña group (Fig. A.1). The El Niño simulations peak between September before initialization and January with peak values between 2.2 and 3.6°C (3-month running mean Niño 3.4 SST anomaly). They show a fast decline in the anomaly with most models having a negative anomaly in December of the

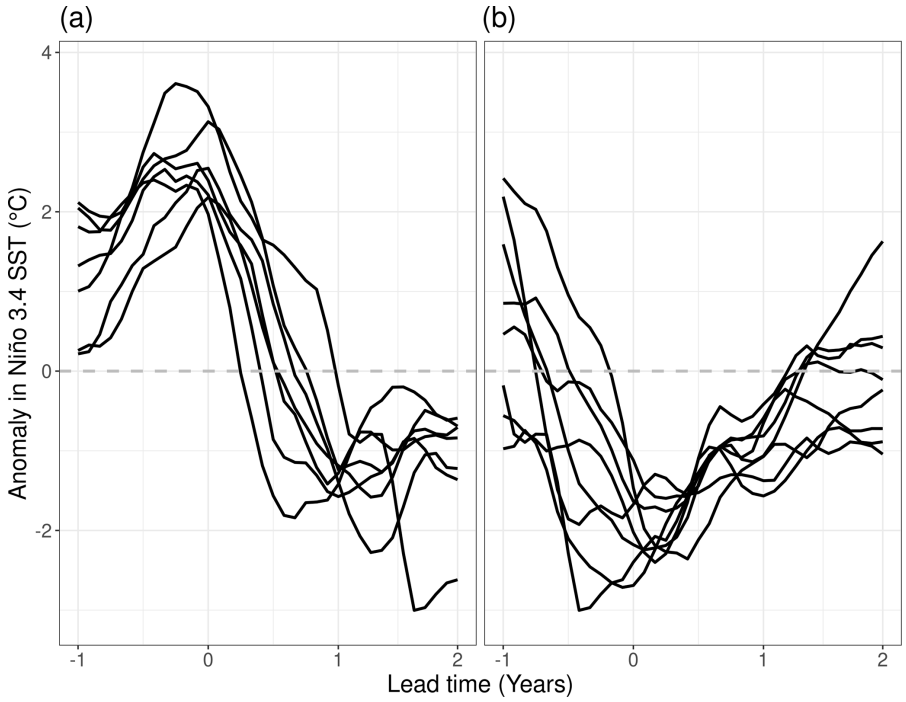

Figure A.1: Three-month running mean SST anomaly in the Niño 3.4 region of **(a)** seven El Niño and **(b)** eight La Niña simulations. Simulations are initialized at lead time 0 and run for 24 months. Lines show the Niño 3.4 SST of the control simulation.

first year and evolving into a La Niña event in the second year. Peaks of the La Niña simulations fall between September and June and, while their relative peak anomalies are smaller (-1.6 to $3.0°C$), the negative anomaly can be sustained well into the second year.

A.3.1 *Potential predictability*

The 35 perfect model simulations are used to assess potential NPPpred and Rhpred. Zonal means of the ACC are shown in Fig. A.2 (zonal plots of predictability are limited to 30°S to 30°N to highlight the areas of high predictability). NPPpred and Rhpred are highest in the tropics between 20°N and S, where carbon fluxes are at their global maximum. However, apart from the generally high predictability in the tropics, the patterns of NPPpred and Rhpred differ in several aspects. While the ACC of NPP has a slower temporal decline with values above 0.8 for 2 to 3 months around the Equator, the ACC of Rh drops below 0.5 within the first 2 months for most latitudes. However, Rh

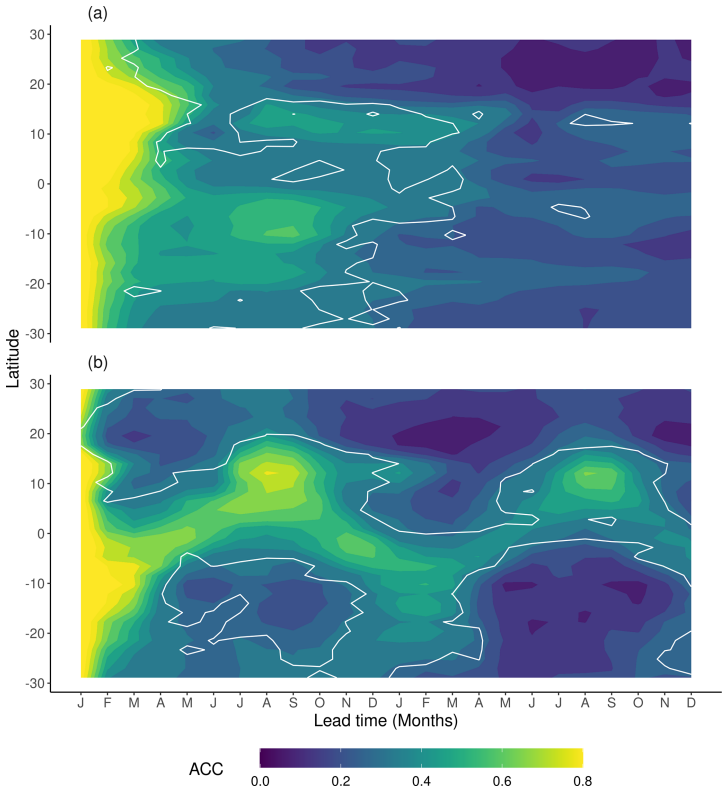

Figure A.2: Zonal means of ACC derived from 35 ensemble simulations starting in January for **(a)** NPP and **(b)** Rh. Contour lines indicate correlations above the 95 % confidence level.

shows much higher long-term predictability, especially in the second year of the simulation where Rhpred is much higher than NPPpred.

While both predictability patterns show signs of a seasonal cycle, they are out of phase, with Rhpred distinctly following the wet season and NPPpred appearing to be higher in the dry seasons of the first year. This has a large role in the comparability of NPPpred and Rhpred, since high NPPpred occurs at the time of the seasonal low of NPP fluxes, while high Rhpred is associated with the seasonal high. Another characteristic of the seasonal cycles is their continuity. Rhpred migrates continuously across the zones, while NPPpred demonstrates a sporadic behaviour with a high predictability at around 15°N in January to March and another one at 10°S from July to September.

The spatial patterns of ACC are shown in Fig. A.3 for March, June, and September of the first year and September of the second year. Rhpred shows a very coherent pattern with a band of high predictability migrating from south to north across all continents. The patterns of NPPpred appear to be less con-

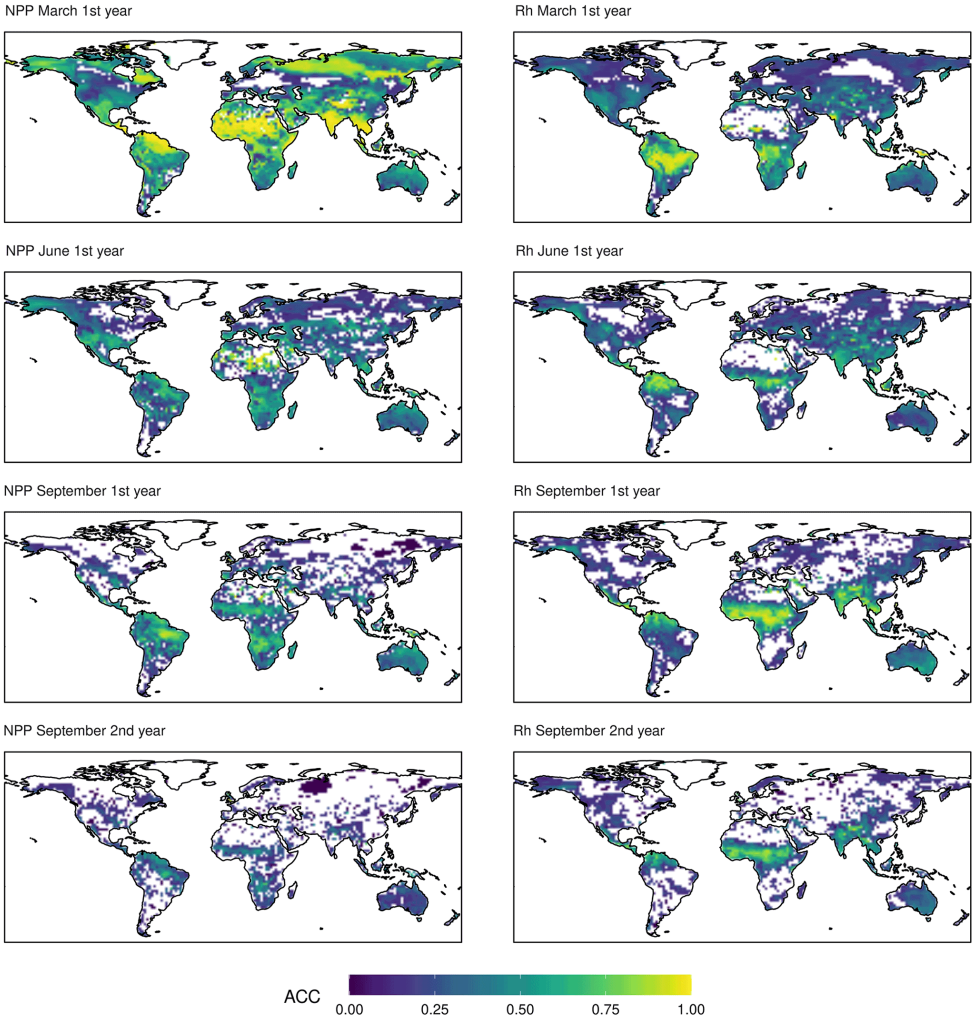

Figure A.3: ACC of NPP and Rh. The colour scale is cropped at zero. Only values above the 95 % confidence interval are shown.

strained by latitude. Although March predictability is dominated by the northern tropics and subtropics, there are other high-predictability regions based on initial memory, especially at high latitudes. As opposed to Rhpred, there is no high-predictability band moving across the zones. Instead, NPPpred is re-emerging south of the Equator in September in the southern Amazon Basin, southern Africa, and Southeast Asia. An aberration from the seasonal pattern is in the Sahel, which has a relatively high NPPpred throughout both years, except in June and July (not shown).

A large portion of the high NPPpred areas can be attributed to predictability gained by ENSO. These high-predictability areas are concurring with the carbon flux anomalies caused by ENSO-related climate variability (Bastos et al., 2013; Hashimoto et al.,

2004). A specific example of this is the disparity in NPPpred between the tropical rainforests of the Amazon and the Congo basins. It shows that the high NPPpred of the tropics is not an intrinsic property of these ecosystems. A reason for the relatively low NPPpred within the Congo Basin could be because it is not strongly impacted by ENSO (Holmgren et al., 2001). These findings highlight the importance of correctly simulating the ENSO process. Especially the localization of ENSO-related rainfall patterns is crucial since they provide a sustained and predictable anomaly in water availability.

Many of the identified spatial patterns of CFpred can be discovered in similar studies. Most models agree on the Amazon Basin as the global hotspot of CFpred (Ilyina et al., 2021; Zeng et al., 2008), and some reflect the increased predictability in Southeast Asia and southern Africa (Zeng et al., 2008), but the comparison of predictability horizons remain difficult due to the use of different predictability metrics.

The results reveal different areas in which an operational NPP forecast can be used to increase food security. The high NPPpred of the Sahel and Kalahari savanna ecosystems (Fig. A.3) could be used to plan stocking rates in order to avoid grassland degradation due to overgrazing in dry years (Tews et al., 2006). Other promising regions are northeast and central Brazil. The high NPPpred in these areas could be used to select crop varieties which are more or less drought tolerant depending on the given forecast.

A.3.2 *Composition of predictability*

CFpred is sufficiently captured by the regression models (Eq. A.4) with a correlation of 0.71 and 0.75 for NPP and Rh, respectively (averaged correlation between the V_c derived from the ensemble simulations and the V_c of the regression model for each grid cell and lead time, not shown). The contributors of CFpred show strong spatiotemporal heterogeneity with drivers alternating across seasons and regions. The temporally averaged contributions to weighted predictability are shown in Fig. A.4. The drivers of NPPpred are SOILpred (sum of midSOILpred and deepSOILpred) and TEMPpred, which explain 62 % and 30 % of the globally averaged NPPpred, respectively. PARpred only contributes 8 % to the NPPpred, most of it in the first month of the simulations. The NPPpred patterns of V_c explained by SOILpred and TEMPpred are similar to the patterns of ACC,

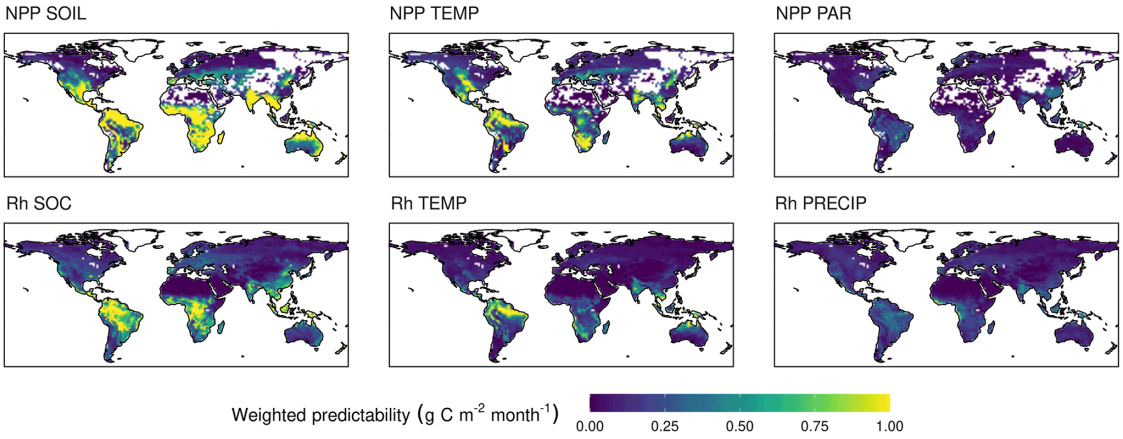

Figure A.4: Contributing components to the weighted predictability (wV_c) of NPP and Rh. The contributors to NPP predictability are the predictability of soil moisture (SOIL), temperature (TEMP), and photosynthetically active radiation (PAR). Contributors to Rh predictability are the predictability of soil organic carbon (SOC), TEMP, and precipitation (PRECIP). The averaged predictability of the first 12 months lead time weighted by carbon flux anomaly of the ensemble means. The sum of all components of a flux type gives the modelled total predictability of that flux.

although areas with low carbon flux densities are excluded through weighting by absolute flux anomaly. While the NPPpred explained by SOILpred has a spatial extent that broadly covers all regions of high NPPpred, TEMPpred is concentrated in certain areas. TEMPpred is high in a band extending from the Amazon Basin to northern South America, southern Africa, and Southeast Asia. The largest contributor to Rhpred is SOCpred (52 %) followed by TEMPpred (27 %). Similar to NPPpred, the temperature component is highest in the Amazon Basin, southern Africa, and Southeast Asia.

In order to facilitate a system for operational NPP prediction, a network of sensors could be installed to gather data on the initial condition of the land surface. The patterns of the role of soil moisture in predicting NPP (Fig. A.4) reveal the areas on which the efforts in establishing such a network should be focused to maximize the impact.

There are more variables that are regarded as key drivers of NPP variability and could have been regarded as predictors in the regression models. Most importantly, LAI and humidity play an important role in NPP variability (Schaefer et al., 2002). Several studies show the role of a dynamical simulation of LAI

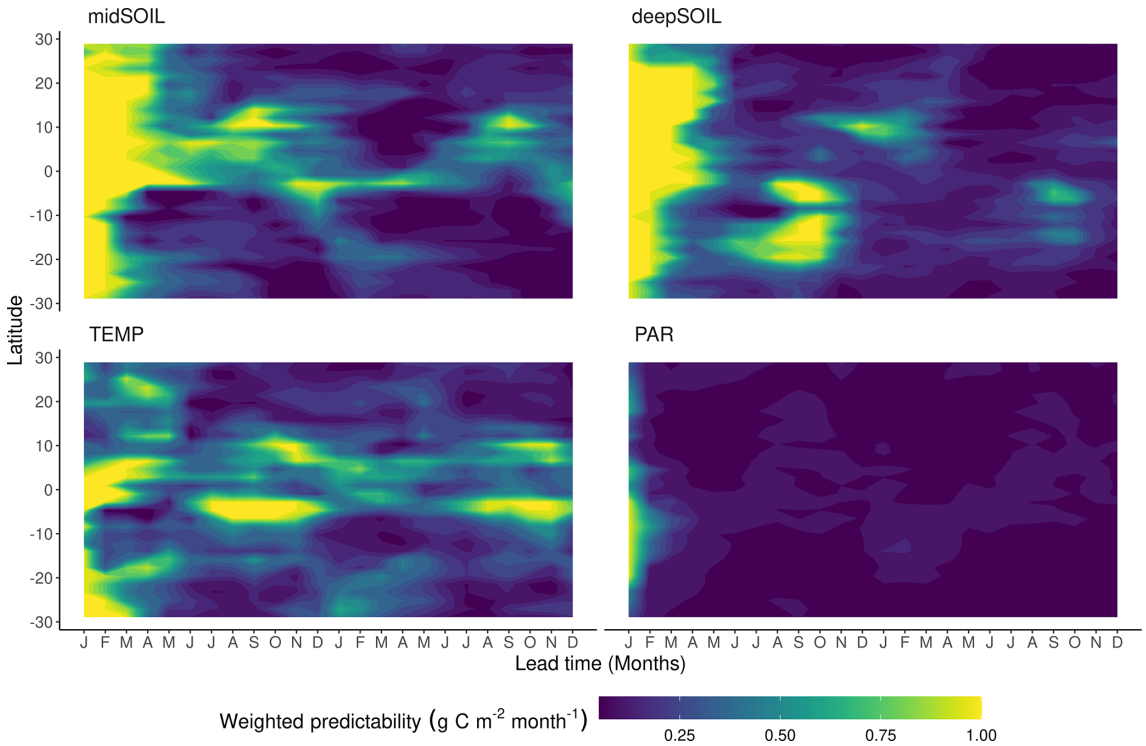

Figure A.5: Zonal means of contributing components to the weighted NPP predictability (wV_c). The contributing components are the predictability of soil moisture at 19–78 and 79–268 cm depth (midSOIL and deepSOIL), air temperature (TEMP), and photosynthetically active radiation (PAR).

in extending the predictability of land surface processes (Wang, Sun, and Mei, 2011; Wang et al., 2010; Weiss et al., 2012, 2014; Zeng et al., 1999). Here, the inclusion of LAI as a predictor is rejected because of the susceptibility of regression models to correlated predictors. The changing concentration of atmospheric CO_2 is causing trends in NPP as global atmospheric levels are rising (Winkler et al., 2021); however, we assumed that the interannual variability of CO_2 fertilization is below a meaningful contribution to overall variability. Although clay content plays a major role in carbon turnover rates in soil (Coleman et al., 1997), it is not considered in the JSBACH Rh submodel (Tuomi et al., 2009) and was not included in this study.

A.3.2.1 *Seasonality*

The seasonal patterns of NPPpred revealed in the ACC data (Figs. A.2 and A.3) are reproducible by the decomposed predictability metric V_c (Fig. A.5). They show the re-emergence of predictability in the dry season at various locations and reveal

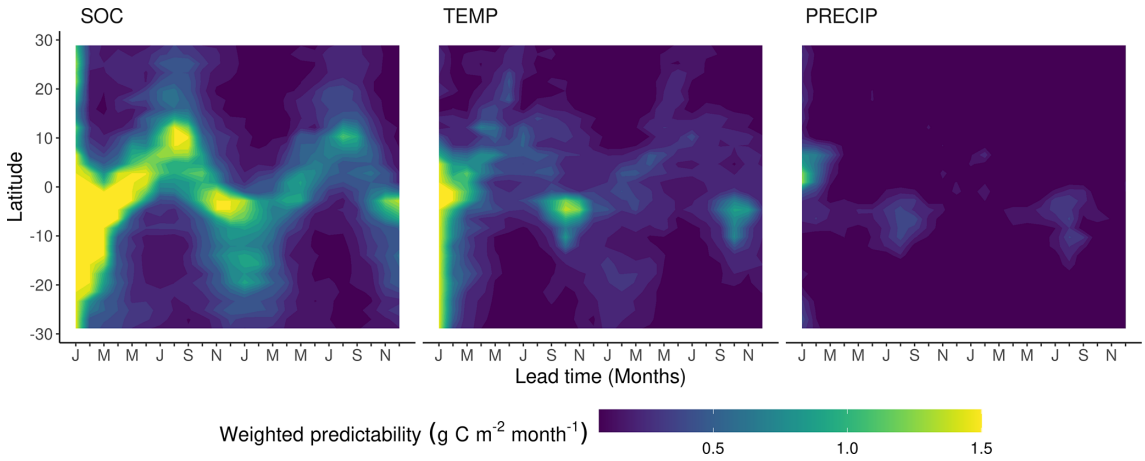

Figure A.6: Zonal means of contributing components to the weighted Rh predictability (wV_c). The contributing components are the predictability of soil organic matter (SOC), air temperature (TEMP), and precipitation (PRECIP).

that this phenomenon cannot be attributed to a single factor. The largest pattern is a re-emergence in July to November at 1 to 4°S, and this can be associated with the high NPPpred in the southern Amazon (Fig. A.3, NPP September first year). This pattern is due to increased TEMPpred throughout the dry season, which is extended by high deepSOILpred in September, and even reoccurs in the second year of the simulation. Another pattern explains the high NPPpred in southern Africa between August and October, which is due to deepSOILpred.

These cases of high dry-season NPPpred in the tropics are most likely due to the seasonally changing limitations of NPP. During the productive wet season, plant growth is limited by incoming radiation (Wang et al., 2010), which has little variability and poor predictability. Instead, most of the interannual variability of NPP can be explained by dry-season variability. One study found over 80 % of western Amazon NPP variability took place between July and September (Wang, Sun, and Mei, 2011). The water limitation of NPP during the dry season (Tian et al., 2000) not only introduces higher variability as compared with the energy-limited wet season, but the coupling of NPP to soil moisture also lends NPP the high predictability of soil moisture.

Although the seasonality of Rhpred shows a reverse tendency to NPPpred with higher predictability in the wet season, the mechanisms explaining the seasonality are similar. The seasonally varying Rhpred can be explained by the inherently different

predictability of the seasonally dominant limiting factor of Rh (Fig. A.6). During the dry season, the limiting factor of Rh is precipitation, which has a generally low predictability. The absence of precipitation for several weeks will inhibit soil respiration completely. There is a sharp increase in Rh variability in the dry–wet transition because the onset of precipitation is difficult to predict. As precipitation increases, the moisture constraint is asymptotically lifted and approaches zero. At this point, Rh becomes limited by substrate availability, which has a much higher predictability than climatic variables. The high SOCpred is due to the persistence of SOC anomalies because of the low decomposition rates and the pause of decomposition during dry seasons. Although TEMPpred is higher than PRECIPpred, it only plays a minor role in tropical Rhpred because tropical Rh has relatively low-temperature sensitivity (Meir et al., 2008).

These pronounced seasonal patterns of Rhpred hinge on the implementation of the precipitation sensibility function in MPI-ESM. The shape and parameterization of the rate-modifying function of decomposition to moisture sets Rh to be more sensible to precipitation in the dry than in the wet season. However, the relationship between Rh and moisture in the tropics is the highly debated subject of various studies coming to different conclusions. These studies suggest a parabolic or no relationship with soil moisture (Meir et al., 2008) or a linear increase with precipitation (Tian et al., 2000).

A.3.2.2 *Interannual variability*

Using the distance-based predictability metric V_c also allows us to evaluate the variability of predictability between different initializations. Among the regions with the highest interannual variability of NPPpred are the southern Amazon Basin (box in Fig. A.7), with a mean V_c of 0.24 and an SD of 0.32, and northwestern Australia, with a mean of 0.16 and an SD of 0.60 (23°S, 122°W). Figure A.7 shows how the interannual variability of NPPpred is affected by initial soil moisture. The majority of regions with a high NPPpred (Figs. A.3 and A.4) have a higher predictability in years initiated from wet states. Exceptions to this trend are India and northwestern Australia, where NPPpred is higher in dry years. The strongest difference in NPPpred is in the Amazon Basin, where overall NPPpred and interannual variability of predictability are also at the global maximum.

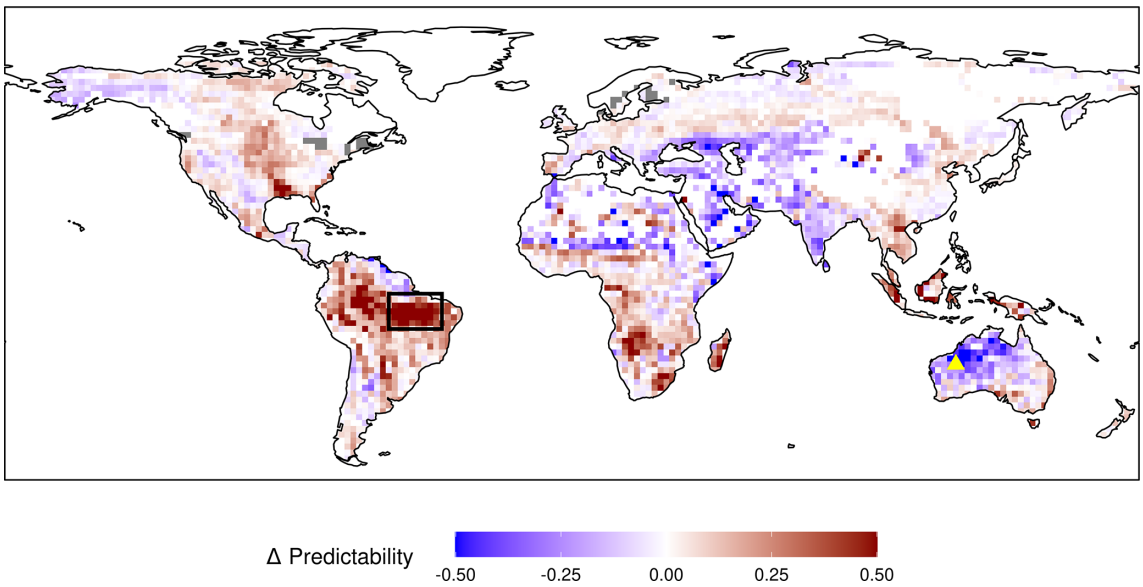

Figure A.7: Difference in NPP predictability (V_c) based on the initial soil moisture. The mean NPP predictability of the first year from the 20 % driest initializations are subtracted from the 20 % wettest initializations for every grid cell. Red colour means higher NPP predictability in wet years and blue colour a higher predictability in dry years. Soil moisture from 19–78 cm depth is used to determine initial conditions. A large fraction of years included in the initializations are ENSO years, where the initial anomaly is further extended through persisting oceanic forcing. The black box and yellow triangle stand for regions examined in the main text.

To determine the mechanisms responsible for this difference in predictability we focus on the composition of the NPPpred in the southern Amazon Basin (box in Fig. A.7). To represent wet and dry years, a composite analysis is used based on the ENSO states. (The El Niño years are the driest extremes at initialization, while soils are often saturated at the beginning of La Niña years.)

The different composition of NPPpred within the southern Amazon Basin is shown in Fig. A.8. La Niña years have an overall higher NPPpred, which even lasts throughout the second year of the simulations. However, the drivers causing the difference in increased La Niña predictability are changing over time. At the start of the growing season, which is between December and July, midSOILpred contributes largely to the increased La Niña predictability, while deepSOILpred gains in importance around June, when topsoils begin to dry out. An increase in

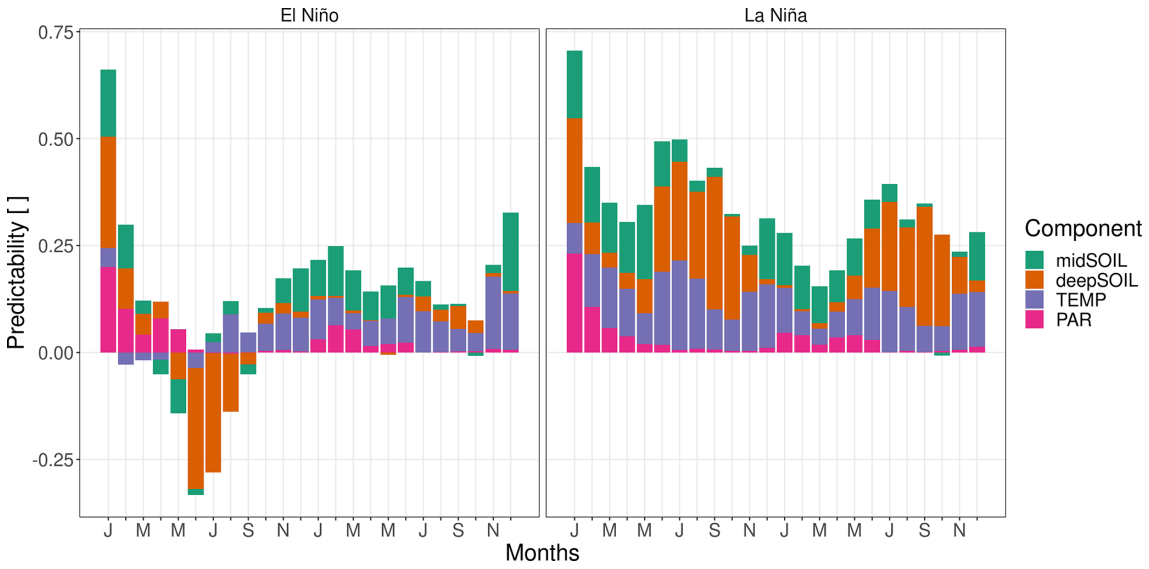

Figure A.8: The composition of NPP predictability (V_c) in the Amazon Basin by ENSO state. The contributing components are the predictability of soil moisture at 19–78 and 79–268 cm depth (midSOIL and deepSOIL), air temperature (TEMP), and photosynthetically active radiation (PAR). La Niña years have an overall higher predictability. Negative values mean an ensemble variance that is exceeding the climatological variance.

TEMPpred explains a large fraction of increased La Niña predictability throughout the first year.

The increase in midSOILpred during the growing season can be explained by the relationship between precipitation and the change in soil moisture in spring (Fig. A.9a). Although the variability of precipitation is comparable between the ENSO states, there is little change in soil moisture in the La Niña years, while the relationship between precipitation and soil moisture change is more pronounced in the El Niño years. The difference in this covariance between the ENSO states is linked to the initial water content (Fig. A.9b). The El Niño year is initialized at a depleted state, and precipitation is used to recharge midSOIL. This leads to the translation of the variability in precipitation to a variability in midSOIL. Since midSOIL is saturated at the initialization of the La Niña year, it is hardly affected by the variability of precipitation and the excess water leaves the system as runoff or drainage.

The same mechanism is responsible for the difference in deepSOILpred. As midSOIL dries out during the summer months, NPP is increasingly coupled to deepSOIL. Every ensemble mem-

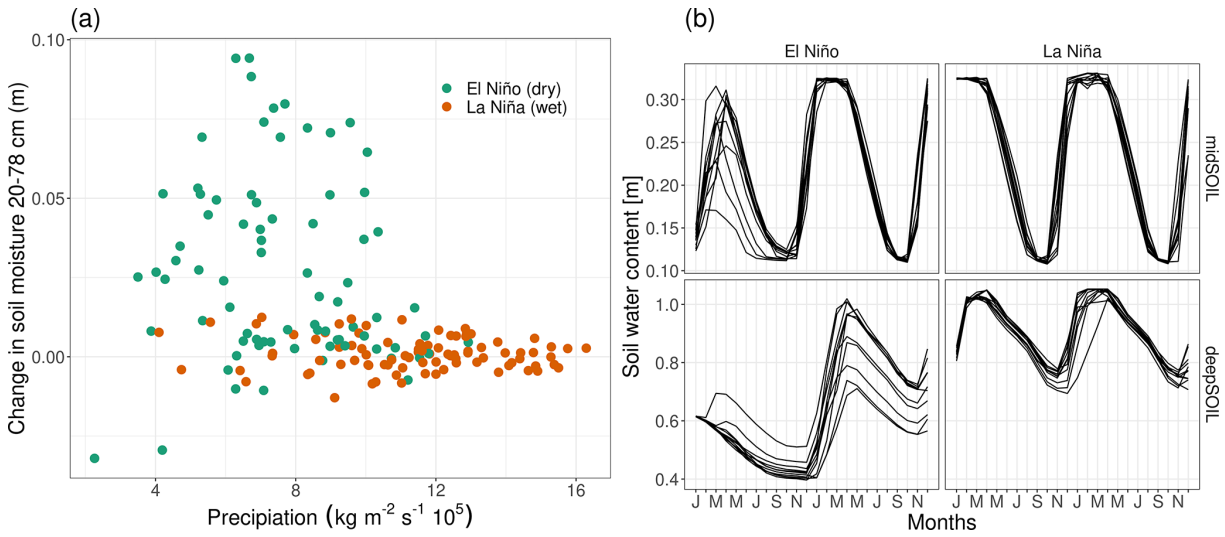

Figure A.9: Soil water dynamics of different ENSO states in the Amazon Basin at 8°S, 54°W. **(a)** Relationship between February precipitation and change in soil moisture from February to March. **(b)** Soil water content of the 11-member ensemble simulation for one specific El Niño and La Niña year (midSOIL and deepSOIL are the moisture content at 19–78 and 79–268 cm, respectively).

ber of the La Niña simulation receives enough precipitation to saturate deepSOIL, thereby reducing its variability, while none of the members in the El Niño year can recharge the soil water deficit.

Increased NPPpred in wet years due to TEMPpred can have multiple reasons which are difficult to disentangle. As soil moisture and surface temperature are coupled through evapotranspiration, a reduced variability in soil moisture suggests a reduced variability in temperature as well. Contributing to this effect is the nonlinear mechanism controlling evaporation. At the wet end of the spectrum, evaporation is not limited by soil moisture, meaning that a small variability in soil moisture of a wet soil does not affect evaporation. A counteractive process that might increase predictability in dry years is described by Koster et al. (2011). They suggested that in ecosystems which are generally at the wet end of the spectrum (which is the case for the Amazon Basin) land–atmosphere coupling is stronger in dry years when evaporation is limited by soil moisture. This increased coupling can extend TEMPpred by linking it to soil moisture. However, their study was conducted in North America, where land–atmosphere coupling is generally stronger than in tropical rainforests (Guo and Dirmeyer, 2013).

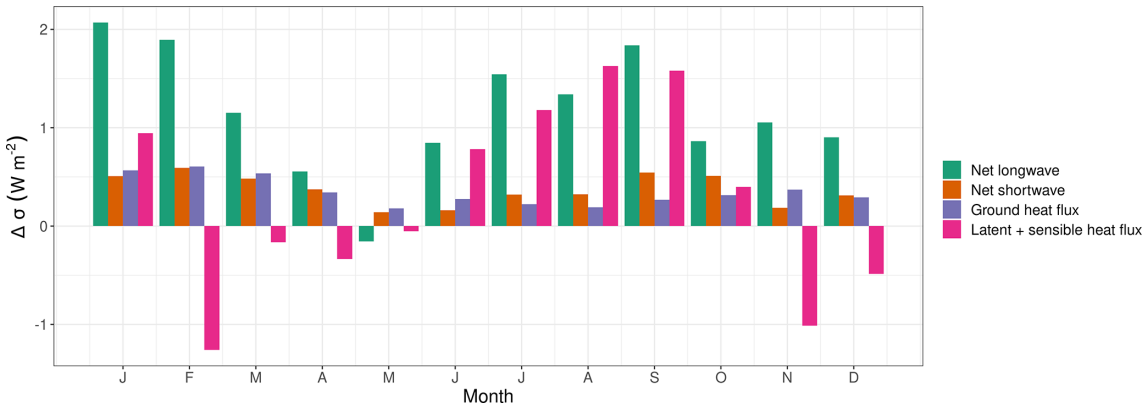

Figure A.10: Difference in standard deviation ($\Delta\sigma = \sigma$ El Niño – σ La Niña) of different components of the surface energy balance in the Amazon Basin. The latent and sensible heat fluxes are pooled because of their strong negative correlation.

To investigate processes behind the difference in temperature variability per ENSO state, we analysed the key elements of the surface energy balance. Almost all processes have a continuously higher variability in the El Niño years (Fig. A.10). The strongest difference in variability is in net longwave radiation, but this is most likely an effect of increased variability of surface temperature and not the cause. The SD of net shortwave radiation and ground heat flux are evenly increased by around 0.4 W m^{-2} across the first year. Except for some winter and spring months, the latent and sensible heat fluxes have an increased variability in the El Niño years. At the peak, the difference in variability in August is mostly due to increased variability in the latent heat flux.

As mentioned above, there are also certain regions with an inverse relationship between wetness and NPPpred. These are predominantly in arid regions like northwestern Australia, India, northern Caucasus, and the western US (Fig. A.7). The mechanisms explaining the increased NPPpred in dry years are exemplified using two initializations from the dry and wet spectrum in northwestern Australia at 23°S, 122°E (yellow triangle in Fig. A.7).

This higher NPPpred can be attributed to less variability in deepSOIL and PAR (Fig. A.11). The predictability-providing mechanism of deepSOIL is comparable with the process in the Amazon Basin. With soil moisture dynamics frequently operating at extreme ends of the water-holding capacity, the variance can be minimized by all ensemble members being

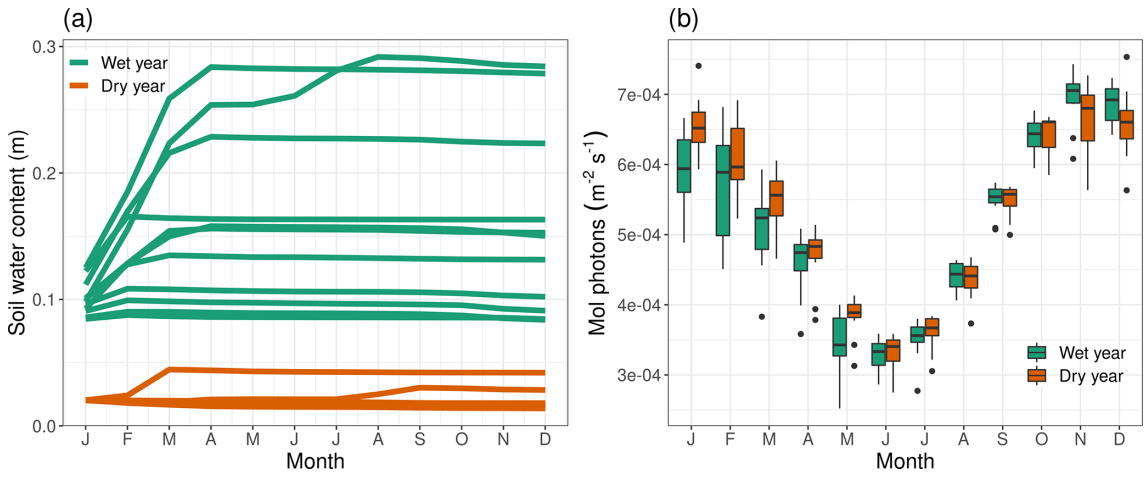

Figure A.11: Difference in ensemble member spread in northwestern Australia between a wet and a dry year for **(a)** deepSOIL and **(b)** PAR.

pushed against the boundaries of the system. As opposed to the Amazon Basin, in northwestern Australia the ensemble members are clustered at the dry end of the water-holding capacity (Fig. A.11a, dry years), while any introduction of soil moisture will increase the variability.

Another difference in NPPpred is caused by a differing variability of PAR (Fig. A.11b). Most dry years have little cloud cover and no restriction of incoming radiation. However, in wet years it is difficult to predict the extent of precipitation and cloud cover, which increases the variability of PAR.

The relationship between initial soil moisture and climate predictability is noted by others. Koster et al. (2011) have determined that, depending on the region, the direction of this relationship can go either way. This asymmetry of predictability is present in areas of high land–atmosphere coupling and is caused by the nonlinear relationship of evaporative fraction with soil moisture. Another study has investigated the predictability of European summer heat and found different weather regime frequencies in initially dry and wet conditions (Quesada et al., 2012). This study adds to the view that predictability is not a mere function of location but depends on the state of the system, and predictability, therefore, has a strong temporal variability.

A.4 CONCLUSIONS

In this study, we take a closer look at spatiotemporal patterns of terrestrial CFpred and identify the climatic and environmental

sources of predictability and the feedback mechanisms prolonging the memory of the system. We propose a metric of CFpred weighted by the amplitude of carbon flux anomalies. This metric allows us to evaluate the role of different regions and processes to the predictability of the global carbon cycle.

We find that the spatiotemporal patterns of NPPpred and Rhpred are determined by (a) the predictability of the carbon flux drivers, (b) the climatic anomalies caused by low-frequency climate modes such as ENSO, (c) the seasonal change in limiting factors, and (d) threshold processes and the nonlinearity of ecosystem responses.

On the global average, NPPpred is explained by SOILpred to 62 % and by TEMPpred to 30 %. Rhpred is explained by SOCpred and TEMPpred (50 % and 27 %) predictability. Decomposing the predictability signal shows there is a high spatiotemporal variability in the drivers of predictability. SOILpred and SOCpred are distributed across all areas of high CFpred, while TEMPpred is mostly to be found in the northern Amazon Basin for CFpred and southern Africa, North America, and Southeast Asia for NPPpred. Rhpred can outlast NPP predictability because SOC, its main driver, has a much higher anomaly persistence than the drivers of NPP. On the other hand, NPP is more directly affected by climatic drivers and is therefore able to benefit from the predictability of persisting climatic anomalies like the effects of ENSO. Intra-annual variability of CFpred is controlled by the seasonally specific limiting factor of NPP and Rh. This leads to NPP gaining predictability in the dry season when soil moisture replaces PAR as the limiting factor, while Rhpred has its peak in the wet season when SOC drives the carbon fluxes instead of precipitation in the dry season. This change in limiting factors is due to the nonlinear relationships of transpiration to soil moisture and Rh to precipitation. Both of these relationships describe a saturation point, at which the variability of moisture (precipitation) becomes insignificant to carbon fluxes. Lastly, interannual variability of NPPpred reveals an asymmetry of predictability driven by initial soil moisture and subsequent precipitation. This effect is caused by ecosystems operating at the boundary conditions of the soil moisture regime. The ensemble members of predominantly wet ecosystems are harmonized in wet years when precipitation exceeds the water-holding capacity and excess water is removed through runoff and drainage. The reverse effect applies to ecosystems op-

erating at the dry end of the spectrum. These processes reduce the covariance between precipitation and NPP.

Our results highlight the sources of CFpred and can be used for model development to improve the representation of the terrestrial carbon cycle. Further research could be directed towards the simulation of the ENSO imprint in climate models and the relationship between soil moisture and terrestrial carbon fluxes.

B

GPP AND THE PREDICTABILITY OF CO_2: MORE UNCERTAINTY IN WHAT WE PREDICT THAN HOW WELL WE PREDICT IT

The work in this appendix is scheduled for submission as:

Dunkl, I., N. Lovenduski, A. Collalti, V. K. Arora, T. Ilyina, and V. Brovkin (n.d.). "GPP and the predictability of CO_2: more uncertainty in what we predict than how well we predict it." *Ready for submission to Biogeosciences* ().

Author contributions:
ID, TI and VB conceived the study. ID performed the simulations and analysis, created the figures and drafted the manuscript. TI, VB, NL, AC, VA contributed to manuscript editing and providing feedback.

GPP and the predictability of CO_2: more uncertainty in what we predict than how well we predict it

István Dunkl[1,2], Nicole Lovenduski[3], Alessio Collalti[4], Vivek K. Arora[5], Tatiana Ilyina[1] and Victor Brovkin[1,6]

[1]Max Planck Institute for Meteorology, Hamburg, Germany
[2]International Max Planck Research School on Earth System Modelling, Hamburg, Germany
[3]Department of Atmospheric and Oceanic Sciences, University of Colorado, Boulder, CO, USA
[4]Forest Modelling Lab., Institute for Agriculture and Forestry Systems in the Mediterranean, National Research Council of Italy (CNR-ISAFOM), Perugia, Italy
[5]Canadian Centre for Climate Modelling and Analysis, Environment and Climate Change Canada, University of Victoria, Victoria, British Columbia, Canada
[6]Center for Earth System Research and Sustainability, University of Hamburg, Hamburg, Germany

Abstract

The prediction of atmospheric CO_2 concentrations is limited by the high interannual variability of gross primary production (GPP). Although Earth system models (ESMs) have a comparable prediction skill of land-atmosphere CO_2 fluxes, the spatial patterns and drivers of GPP variability show profound differences. This raises the question to what extent these predictions of CO_2 fluxes can be compared. Here, we dissect the role of GPP in the predictability of atmospheric CO_2 in six ESMs by viewing the GPP predictions within the context of the model specific variability. We analyse the spatial patterns of GPP variability using regression analysis to determine the role of the environmental drivers soil moisture, temperature and radiation, and assess the general ability of the ESMs to retain memory in hindcast systems. Lastly, we determine the origin of the predictable GPP variability that contributes to the prediction of atmospheric CO_2. The ESMs are similar in the share of GPP they can predict from their overall GPP variability. Between 13% and 24% of the GPP variability can be predicted one year in advance on a global average, with four out of six models between 19% and 24%. There is also conformity on the contribution of environmental drivers to the predictive performance. Up to 32% of the variability induced by soil moisture is predictable, while only 7% to 13% of the radiation-induced variability. However, there is less agreement on the spatial distribution of GPP variability. Although all ESMs agree on the high variability in the semi-arid tropics, several ESMs have unique hotspots responsible for a large fraction of their GPP variability. The main driver of GPP variability is temperature in the ESMs using the Community Land Model, and soil moisture in IPSL-CM6A-LR and MPI-ESM-LR, revealing underlying differences in the source of GPP variability among the models. The results show that while ESMs are fairly similar in their ability to predict themselves, their predicted contribution to the atmospheric CO_2 variability originates from different regions and is caused by different drivers. A higher coherence in atmospheric CO_2 predictability could be achieved by reducing uncertainties of GPP sensitivity to soil moisture, and by accurate observational products for GPP variability, which can be used during the model parameterization process.

B.1 INTRODUCTION

Year-to-year variations in land-atmosphere carbon fluxes generate substantial variability in the atmospheric CO_2 concentration, challenging our ability to quantify changes in fossil fuel-based emissions, including those stemming from carbon reduction policies (Friedlingstein et al., 2020; Peters et al., 2017). Seasonal-to-decadal (S2D) predictions of land-atmosphere CO_2 fluxes, specifically gross primary productivity (GPP), therefore, have the potential to accelerate the evaluation of carbon reduction policies (Piao et al., 2020).

The predictability of GPP can be assessed by using forecasts of the past (hindcast simulations), where an ensemble of simulations with an Earth system model (ESM) is initialized from quasi-identical conditions. In a system with little predictability, the spread across the ensemble will increase quickly until it reaches the climatological variability. However, certain processes have the ability to retain memory and provide predictability by hindering this divergence of the ensemble members. For example, the El Niño-Southern Oscillation (ENSO), produces a low-frequency variability of the global climate that leads to sustained GPP anomalies (Betts et al., 2016; Zeng et al., 2008). Other processes provide predictability by maintaining the initial conditions of the simulation. For example, soil hydrology acts as a buffer between the atmosphere and the vegetation by storing initial moisture anomalies (Bellucci et al., 2015). Soil moisture anomalies can be further extended through land-atmosphere coupling, by creating a feedback loop that enhances the persistence of these anomalies (Kumar et al., 2020). A similar phenomenon can arise through the lagged response of plant biomass growth to climatic conditions. The slowly reacting vegetation can cause precipitation anomalies or prolonged drought (Alessandri and Navarra, 2008; Zhang, Keenan, and Zhou, 2021).

As initialized ESMs are capable of making reliable predictions of climatic variables like global temperature anomalies or ENSO on S2D time scales (Meehl et al., 2021), these models should also be able to predict land-atmosphere carbon fluxes with sufficient skill. In fact, a multi-model analysis of land-atmosphere predictability found comparable predictability horizons of two years among many ESM prediction systems (Ilyina et al., 2021). However, several ecosystem processes that have a large impact on the carbon cycle are simulated differently across different model structures. This leads to substantial differences in the

reproduction GPP variability among the models. One of these deviations is in the extent of ecosystem boundaries and the related spatial distribution of plant productivity. The Amazon rainforest, for instance, is a hotspot of land-atmosphere carbon fluxes and provides a large contribution to the predictability of atmospheric CO_2 (Ilyina et al., 2021; Séférian, Berthet, and Chevallier, 2018; Zeng et al., 2008). However, the transition zone between the wet and semi-arid tropics within the Amazon basin varies among the models due to differences in their representation of land cover (Collier et al., 2018; Hu et al., 2022). Such differences in biome boundaries can also modify the impact of ENSO on the variability of land-atmosphere carbon fluxes. ENSO produces a distinct spatial pattern of climatic anomalies which significantly influences the GPP on 32% of the vegetated land area (Zhang et al., 2019). These ENSO-related climate patterns will have a different impact on GPP depending on the type of biomes under their influence.

In addition to the spatial variability, many ESMs struggle to reproduce the temporal variability of carbon fluxes, which can be seen in the various representations of phenology (Song et al., 2021). Several ESMs overestimate the seasonal amplitude of leaf area index (LAI) in the tropics, and mismatch the timing of LAI maxima and minima (Peano et al., 2019).

Further uncertainties in GPP predictability arise from the modelled sensitivity of ecosystem processes to environmental variables (Ahlström et al., 2015; Beer et al., 2010; Collalti et al., 2020; Jung et al., 2017; Piao et al., 2020). For example, global GPP increases with positive temperature anomalies in some models and decreases in others (Piao et al., 2013).

The different sensitivities of GPP to water availability across different models can be further exacerbated by the large disagreement in water storage anomalies (Wu, Lo, and Scanlon, 2021). The simulated annual cycle of water storage anomalies of major river basins is between 0.1 and 2 times that of the observed variability. These large deviations in hydrological variability between models are likely to cause similar deviations in the variability of GPP, especially in semi-arid watersheds.

All of these aspects of possible disagreement between ESMs lead to the assumption that the individual models are creating their very own version of GPP variability. With this in mind, we aimed to extend our view of GPP predictability by investigating not only how well ESMs are able to predict GPP, but also by comparing what these ESMs are predicting in the first place.

We compare the spatio-temporal patterns of GPP variability among six ESMs, and use regression analysis to identify the portions of the variability driven by soil moisture, temperature and radiation. The ESM's ability to retain memory is assessed by calculating the fraction of variability in the GPP predictions to overall GPP variability. Lastly, we determine the origin of the predictable GPP variability that contributes to the prediction of atmospheric CO_2. Thus, the aim of this work is to reveal the origin of differences in GPP predictions across models and to identify the areas of large discrepancies and determine factors contributing to the attached uncertainties.

B.2 METHODS

B.2.1 *Data sources*

We analyse model output from the Decadal Climate Prediction Project (DCPP, Boer et al. 2016). This protocol-driven multi-model approach aims at studying the decadal predictability of the earth system with hindcasts, quasi-real-time forecasts, and case studies on predictability mechanisms. The hindcasts are initialized annually from 1960 to 2017 or 2019 with the starting dates between November and January and at least 10 ensemble members. Simulations are driven by CMIP5 or CMIP6 historical forcing and extended by RCP4.5 or SSP2-4.5 afterwards. The DCPP framework does not prescribe any specific initialization or data assimilation methods and leaves these details to be decided by the respective modelling centres.

The CESM2 model output originates not from the DCPP, but rather from the Seasonal-to-Multiyear Large Ensemble (SMYLE) prediction system (Yeager et al., 2022). The SMYLE hindcasts ensembles are initialized four times per year with 20 ensemble members between 1970 and 2019. In this study, the November initializations are used to achieve the highest comparability with the DCPP hindcasts.

We compared the GPP of the ESMs against the GPP products from the Moderate Resolution Imaging Spectroradiometer (MODIS, MOD17A2H: (Running, Qiaozhen, and Zhao, 2019)).

B.2.2 *Model descriptions*

B.2.2.1 *CanESM5*

The Canadian Earth System Model version 5 (CanESM5; Swart et al. 2019) consists of the Canadian Land Surface Scheme (CLASS) and Canadian Terrestrial Ecosystem model (CTEM) with a T63 grid with an approximate resolution of 2.8°. The atmosphere is realized with the Canadian Atmospheric Model (CanAM5) with 49 vertical levels. Ocean physics are simulated with CanNEMO, on a tripolar grid with a resolution of 1° to 1/3° and 45 vertical levels, and ocean biogeochemistry is represented by the Canadian Model of Ocean Carbon (CMOC).

The CanESM5 hindcast simulations are part of the DCPP project and are initialized every January with 20 members between 1960 and 2017. 3D potential temperature and salinity of the global oceans are nudged toward monthly Ocean Reanalysis System 5 (ORAS5; Zuo et al. 2019). Sea surface temperatures are nudged to Extended Reconstructed Sea Surface Temperature (ERSSTv3; Xue, Smith, and Reynolds 2003; Smith et al. 2008) until 1981 and to the data from Optimum Interpolation Sea Surface Temperature (OISST; Banzon et al. 2016) afterwards. Sea ice concentration is nudged to the Hadley Centre Sea Ice and Sea Surface Temperature data set (HadISST.2; Titchner and Rayner 2014), and sea ice thickness to monthly climatology until 1988 and to the SMv3 statistical model of Dirkson, Merryfield, and Monahan (2017) afterwards. For the atmosphere, temperature, horizontal wind components and specific humidity are nudged to ERA40 (Uppala et al., 2005) until 1978 and to 6-hourly ERA-Interim data (Dee et al., 2011) afterwards.

B.2.2.2 *CESM1-CAM5*

The Community Earth System Model (CESM) version 1.1 (Hurrell et al., 2013) is used to produce 40-member simulations in the Decadal Prediction Large Ensemble (DPLE) project (Yeager et al., 2018). The model components are the Community Land Model version 4 (CLM4; Lawrence et al. 2011) with a 1° resolution, Community Atmosphere Model Version 5 (CAM5) with 30 vertical levels, the Parallel Ocean Program (POP2) with 60 vertical levels and sea ice with Community Ice Code (CICE4).

The CESM1-CAM5 hindcasts are initialized every November. There is no direct assimilation of observations to produce the initial conditions, instead ocean and sea ice are obtained from

simulation runs forced by historic atmospheric surface fields (Yeager et al., 2018). Initial conditions for the land and atmosphere components are obtained from ensemble member #34 of the CESM Large Ensemble (Kay et al., 2015; Lovenduski et al., 2019).

B.2.2.3 *CESM2*

CESM version 2 (Danabasoglu et al., 2020) is using a 1° horizontal resolution of all components. The atmosphere is simulated by the Community Atmosphere Model Version 6 (CAM6) with 32 vertical levels. The ocean model is Parallel Ocean Program version 2 (POP2) with 60 vertical levels, with the biogeochemistry from the Marine Biogeochemistry Library and sea ice by CICE version 5.1.2 (CICE5) with 8 vertical layers. The land component is simulated by the Community Land Model version 5 (CLM5; Lawrence et al. 2019), which has several updates to its predecessor CLM4 and CLM4.5, leading to a better representation of the global carbon cycle in benchmarks (Bonan et al., 2019).

Hindcasts are initialized on the 1st of every November, February, May and August, and run for 24 months. Only the November initializations are used in this analysis to increase comparability with the DCPP simulations. Initial conditions for the atmosphere, ocean and sea-ice stem from the Japanese 55-year Reanalysis (JRA-55; Kobayashi et al. 2015, and JRA55do; Tsujino et al. 2018). The land surface and biogeochemistry are initialized from forced CLM5 simulations.

B.2.2.4 *CMCC-CM2-SR5*

The Euro-Mediterranean Centre on Climate Change coupled climate model (CMCC-CM2, Cherchi et al. 2019, Lovato et al. 2022) is based on CESM and consists of the Community Land Model (CLM4.5) with a 1° resolution, the atmospheric model CAM5.3 with 30 vertical levels. The distinguishing element of CMCC-CM is the ocean, which is simulated by NEMO3.6 while sea ice is modelled by CICE4.

The 10-member hindcast simulations are initialized every November. Initial conditions of ocean and sea ice states are derived from an assimilation run using the same method as the CESM1-CAM5 hindcast.

Because the CMCC-CM2-SR5 fields containing land-atmosphere carbon fluxes are not exported for the DCPP runs, historical

simulations have been used to infer the relationship between environmental drivers and carbon fluxes.

B.2.2.5 *IPSL-CM6A-LR*

The Earth System Model developed by the Institute Pierre Simon Laplace (IPSL; Boucher et al. 2020) uses the ORCHIDEE v2.0 (Cheruy et al., 2020) land surface model (LSM) with an average resolution of 157 km. The atmosphere is simulated at the same resolution by LMDZ6 with 79 vertical levels, the ocean with NEMO-OPA with a 1° resolution and 75 vertical levels and ocean biogeochemistry with PISCESv2.

The hindcast simulations of IPSL-CM6A-LR come from the DCPP project. The 10-member ensembles start annually in January between 1960 and 2016. The hindcasts are initiated from an assimilation run with EN4 sea surface temperatures (Good, Martin, and Rayner, 2013) and Atlantic sea surface salinity (Estella-Perez et al., 2020). Subsurface ocean, sea ice and atmosphere are not assimilated.

B.2.2.6 *MPI-ESM-LR*

MPI-ESM-LR is the Max Planck Earth System Model (MPI-ESM1.1; Giorgetta et al. 2013) used in a low-resolution configuration. The land is simulated by JSBACH with dynamic vegetation (Reick et al., 2013). The ocean component is MPIOM with a horizontal resolution of about 150 km and 40 vertical levels. The atmosphere is simulated by ECHAM at a T63 resolution with 47 vertical layers, and ocean biogeochemistry is represented by HAMOCC.

The utilized hindcast simulations of MPI-ESM-LR are conducted within the MiKlip project (Marotzke et al., 2016). The decadal prediction system are 10-member ensembles starting every January between 1961 and 2014. Ocean temperature and salinity are initialized from the Ocean Reanalysis System 4 (ORAS4; Balmaseda, Mogensen, and Weaver 2013) and the atmosphere by ERA-40 (Uppala et al., 2005) from 1960 to 1998 and ERA-Interim (Dee et al., 2011) from 1990 to 2014.

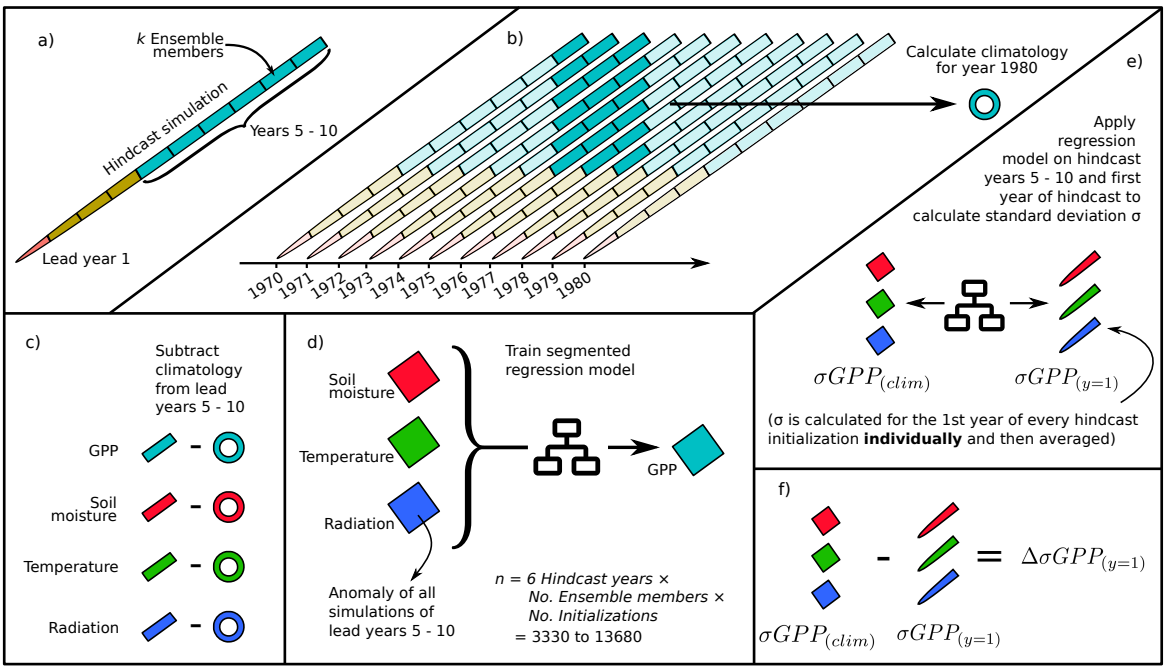

Figure B.1: Workflow of the statistical analysis: a) Structure of the hindcast simulations. The predictability is derived by comparing the variability within the ensemble members of lead year 1 with the variability derived from lead years 5 to 10. b) The climatology is calculated for every year based on a rolling window within lead years 5 to 10 (all simulations within the green block). c) The anomalies of all lead years 5 to 10 are calculated by subtracting the monthly mean climatology. d) A segmented regression model is trained for every grid cell and month of the year. e) The fitted models are applied to the anomalies of the lead years 5 to 10 and to the anomalies of the first lead year to calculate the multi-year standard deviation (SD) $\sigma GPP_{(clim)}$ and the SD within the ensemble members of the first lead year $\sigma GPP_{(y=1)}$. f) The predictable component is assessed through the difference between multi-year SD and the first year SD.

B.2.3 *Statistical approach*

B.2.3.1 *Overview*

An overview of the statistical analysis is shown in Figure B.1. Every hindcast simulation is initialized with >10 simulation members from quasi-identical conditions. With the increasing lead-time, the variability within the hindcast ensemble (spread across the ensemble members for a given time, σ) increases too,

until it reaches the climatic variability (Fig. B.8). Based on this assumption, the hindcast simulations are split into two groups by lead-time (lead year one and lead years five to ten). For the lead years five to ten, the effects of initialization are assumed to be negligible. These years are used to calculate the monthly mean climatology, which is removed from both groups to obtain the anomalies. The anomalies of the lead years five to ten are used in a regression analysis to derive the sensitivity of GPP to the environmental variables i.e. soil moisture, temperature and radiation. The regression model is applied to the anomalies of both groups to calculate the amount of GPP variability caused by each environmental driver. We derive the predictability of GPP by comparing the ensemble variability of the first lead year with the variability in lead years five to ten.

B.2.3.2 *Climatology and sensitivity*

The monthly mean climatologies are calculated from the lead years five to ten, with a moving window approach for every calendar year (Fig. B.1 b). Because the moving window method is not applicable for the first decade of hindcast initializations, the monthly climatology for the 1960s (1970s for CESM2) is calculated based on all lead time years 5 to 10 within the 1960s (or 1970s). Anomalies of all input fields are calculated by subtracting the monthly climatologies from the hindcast data. The obtained anomalies of lead years 5 to 10 make up a data set of n simulation years:

$$n = 6\,\mathit{hindcast\ years} \times \mathit{No.\ ensemble\ members} \times \mathit{No.\ initializations}. \tag{B.1}$$

With 10 to 40 ensemble members and 56 to 58 initializations resulting in sample sizes of 3330 to 13680. Because the hindcast length is only two years in the SMYLE framework, a different approach is used in the case of CESM2. Instead of lead years five to ten, only the second lead year is selected and only five random ensemble members are used from every hindcast, to reduce the number of simulations with the same initial conditions. To offset the reduced number of data points, five random simulations are added from the hindcast simulations initialized in February, May, and August as well.

The resulting data set of anomalies is used to derive the sensitivity of GPP to the environmental variables (ENV: soil moisture, temperature and radiation) by fitting a regression

model for every grid cell and month of the year (Fig. B.1 d). The relationship between GPP and the environmental drivers is frequently non-linear, sometimes due to specific break points in the functional representation of GPP (Fig. B.9). For this reason, segmented linear regression (SLR) is used to model GPP from the environmental variables (Muggeo, 2008). In addition to ordinary regression models, SLR finds breakpoints in the predictor space, splitting it into multiple ranges and fitting an individual regression model to each of the data ranges. Here, a single breakpoint is determined for each of the three predictor variables.

Because environmental drivers have some degree of collinearity, the regression analysis will not be able to fully attribute the GPP anomalies to their specific causes. Therefore, the resulting sensitivities should be taken as a "contributive", and not a "true" effect of the environmental drivers (Wang, Zeng, and Wang, 2016).

B.2.3.3 *Variability and predictability*

With the relationship between environmental variables and GPP established, the SLR is now applied to the individual simulations. We use it to determine the component of the GPP anomaly that is attributed to each of the environmental variables (for every grid cell and month of the year):

$$\Delta GPP \approx \Delta GPP^{Soil\ moisture} + \Delta GPP^{Temerature} + \Delta GPP^{Radiation}. \tag{B.2}$$

The three components of GPP anomalies (ΔGPP^{ENV}) are calculated for every simulation with the hindcast lead time five to ten. From the results, we calculate the interannual variability (IAV) of the components ($\sigma GPP^{ENV}_{(clim)}$, Fig. B.1 e). Similarly, the SLR is applied to the anomalies of all ensemble members of the first hindcast years, to calculate the standard deviation within every hindcast simulation. Averaging over the standard deviations of every first hindcast year returns the variability of the first hindcast year ($\sigma GPP^{ENV}_{(y=1)}$).

The predictability is assessed by comparing the variability of the first hindcast year to the IAV (Fig. B.1 f). A high predictability of an input field means, that its variability is restricted for some time after the hindcast initialization, and does not reach the IAV immediately. Because the hindcast simulations are not evaluated against observations, the calculated metrics reflect the potential

predictability. Here, we refer to them as predictability for the ease of reading.

In order to take different aspects of predictability into account, we calculate a relative and an absolute predictability metric.

As the absolute metric, we calculate the predictable component $\Delta\sigma GPP$. It is the difference between IAV and ensemble variability (Fig. B.2):

$$\Delta\sigma GPP^{ENV}_{(y=1)} = \sigma GPP^{ENV}_{(clim)} - \sigma GPP^{ENV}_{(y=1)}. \tag{B.3}$$

The predictable component can be interpreted as the amount of variability that is predictable. It allows quantifying the regional contribution to atmospheric CO_2 predictability. However, $\Delta\sigma GPP$ is strongly related to the overall magnitude of interannual GPP variability and does not give us an insight on how well memory is stored in the system. Therefore, the predictable fraction (pfGPP) is calculated as the fraction of $\Delta\sigma GPP$ to IAV:

$$pfGPP^{ENV}_{(y=1)} = \frac{\Delta\sigma GPP^{ENV}_{(y=1)}}{\sigma GPP^{ENV}_{(clim)}}. \tag{B.4}$$

This is a relative metric and allows assessing how well memory is retained in the system.

B.3 RESULTS AND DISCUSSION

B.3.1 *GPP variability*

In order to understand the base from which the models are predicting, we start with analysing the patterns of GPP variability. We find agreement in the large-scale patterns of GPP variability, while there are local differences and differences in the overall magnitude of variability (Fig. B.3), with CanESM5, CMCC-CM2-SR5, and IPSL-CM6A-LR at the lower, and CESM2 and MPI-ESM-LR at the higher end of the variability spectrum. Factors that could explain some of the differences in the overall magnitude of variability are the relatively weak ENSO teleconnection in CanESM5 (Swart et al., 2019), or the low total GPP in CMCC-CM2-SR5 (Lovato et al., 2022). The models agree well on the seasonality of variability in the Northern Hemisphere, with variability peaking between June and July. Variability peaks in the Southern Hemisphere in December (CMCC-CM2-SR5), January (MODIS, CESM1-CAM5, CESM2), February (IPSL-CM6A-LR, MPI-ESM-LR) and March (CanESM5). Most of the GPP

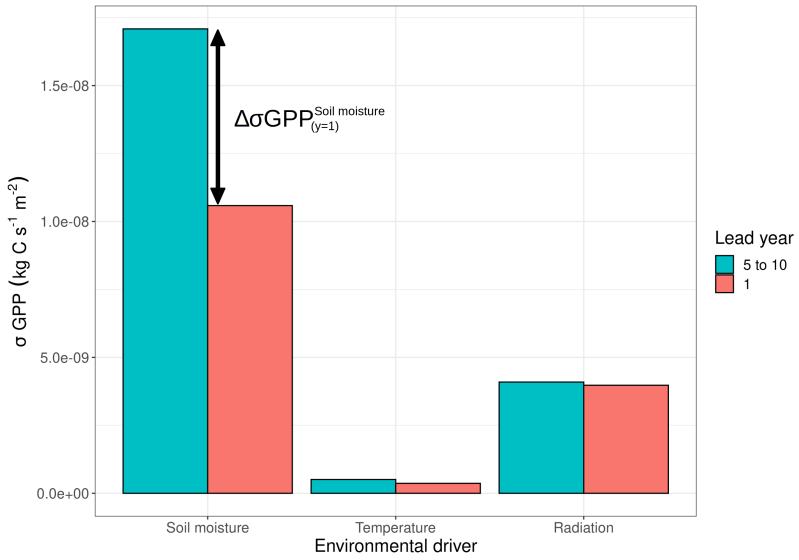

Figure B.2: The exemplary composition of GPP variability of MPI-ESM-LR in the Amazon Basin in April. The interannual GPP variability is calculated as the standard deviation from the model output from the lead years 5 to 10 of the hindcast simulations and split into the contribution of environmental drivers ($\sigma GPP_{(clim)}$, green bars). The red bars show the standard deviation of the ensemble members in lead year 1 ($\sigma GPP_{(y=1)}$). The predictable component ($\Delta\sigma GPP_{(y=1)}$) results from the difference between interannual and ensemble variability. The predictable fraction is the ratio of predictable component to interannual variability. In this region, most of the variability is caused by soil moisture and radiation, while GPP is not restricted by temperature. Predictability is exclusively provided through soil moisture.

variability of ESMs is in the semi-arid tropics of South America, Africa, South Asia, and Australia, but also in southern North America. The variability in MODIS is located in the wet tropics, eastern Asia and central South America. MODIS IAV is generally much lower than the GPP variability of ESMs (Anav et al., 2015; Zhang and Ye, 2022) and not fully capable of capturing tropical variability due to its algorithm (Chen et al., 2017).

A closer examination of the GPP variability patterns reveals that the models have little agreement in the regions that contribute most to the variability, especially in the semi-arid tropics. For a better quantification of this disagreement, we isolated the land area responsible for the top 20% of GPP variability (Fig. B.4). More than half of the grid cells within these high

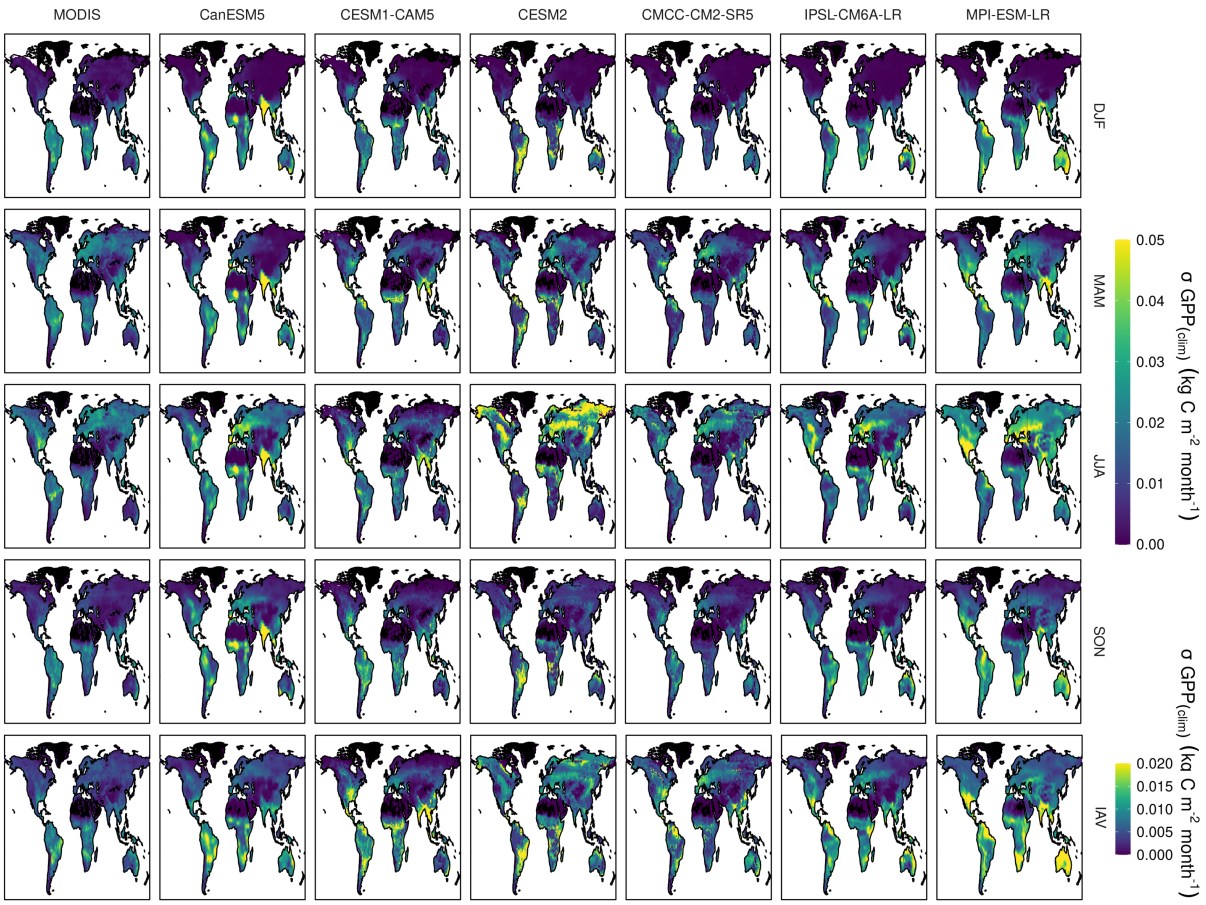

Figure B.3: Mean monthly standard deviation of GPP, averaged over seasons in MODIS and six ESMs, and the IAV of GPP.

variability regions can only be found in one model, while there is not a single grid cell that is in the high variability area of all models. Some models have large patches of high variability regions which are unique to them. Most of the variability in CanESM5 comes from two patches in India and western Africa, In CESM2, high variability occurs in central South America, in IPSL-CM6A-LR the high variability regions are in the Horn of Africa and Southern Africa, while MPI-ESM-LR and IPSL-CM6A-LR are the only models that have large fractions of their variability originating in Australia. We find more agreement on the high contribution of the northeastern coast of South America, which is a high variability region in MODIS, CESM1-CAM5, CMCC-CM2-SR5, IPSL-CM6A-LR, and MPI-ESM-LR.

The spatial patterns of GPP variability revealed here correspond with that reported in the literature, which suggests that the semi-arid tropics, tropical forests, grasslands and croplands are the main drivers of global GPP IAV (Ahlström et al., 2015;

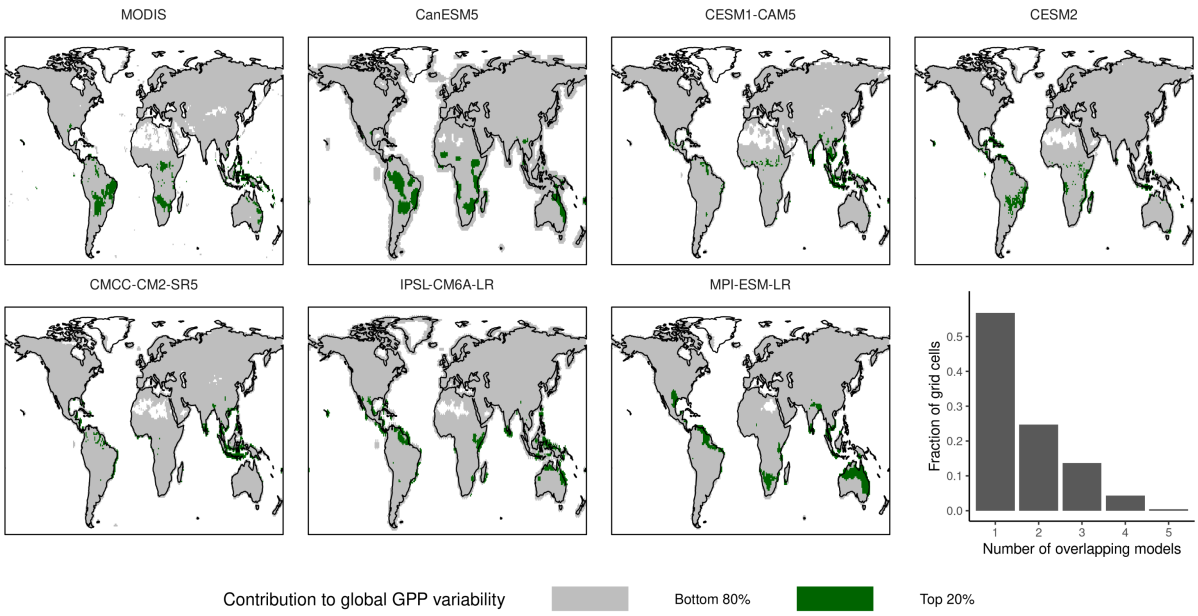

Figure B.4: The area responsible for the top 20% of GPP variability in MODIS and six ESMs. The frequency distribution of the number of overlapping grid cells is shown in the bar chart. More than half of the top 20% grid cells are unique to one model and don't have any overlap.

O'Sullivan et al., 2020; Piao et al., 2020). However, the literature also reflects the large uncertainty in the contribution of the individual semi-arid regions to GPP IAV between the models, and in particular the uncertain role of Australia. In an ensemble of eight LSMs, Australia contributed 39%, semi-arid tropical Africa 32%, and Southeast Asia 10% to global GPP IAV, while temperate South America only contributed 2% (Chen et al., 2017). Although Australia has the highest mean model IAV, the variability of IAV between the models is also the largest, with the standard deviations of GPP ranging between 0.26 and 1.01 Pg C $yr^{-}1$. ESMs are likely to underestimate the role of tropical forests in GPP IAV, due to a misrepresentation of photosynthesis (O'Sullivan et al., 2020). In this study, this is especially evident for CESM2, where GPP IAV increases abruptly outside the boundaries of tropical forests.

The wide divergence in GPP variability across different model structures is caused by three factors: the sensitivity of carbon fluxes to climatic drivers (Piao et al., 2020) (discussed in section 3.2), phenology (Chen et al., 2017; Peano et al., 2019; Peano et al., 2021), and meteorological input (Anav et al., 2015). The role of phenology is crucial because the amount and quality of leaves

determine the exchange of water, CO_2 and energy between the land and the atmosphere (Peano et al., 2021). Most LSMs tend to have a better representation of the growing season type, and growing season boundaries in the wet than in the semi-arid tropics. Peano et al. (2021) analysed the start- and ending months of growing seasons (GSS and GSE) in eight LSMs under the same climate forcing and found several regions with a wide range of growing season boundaries, mostly in semi-arid environments. GSS ranges from February to October in Australia, and from March to October in Southern Africa, while GSE ranged from March to September in Africa between 0 and 15°N. The vegetation types with the largest uncertainty in growing season timing are broadleaf deciduous shrubs, which are mostly located in Northern Australia, Southern Hemisphere crops, and broadleaf evergreen trees and grasses. The better-performing models have a high number of plant functional types, or more complex phenology schemes, while the difficulties in semi-arid regions originate from the response of photosynthesis to soil moisture. Although evergreen tropical forests are generally better represented than the semi-arid tropics, the area of the evergreen tropics is underestimated in JSBACH. A reason for this might be caused by an overestimation of the seasonality in the tropics, as it becomes visible in the strong seasonal cycle of Northern Hemisphere tropical LAI in MPI-ESM-LR (Song et al., 2021). This amplification of the equatorial dry season might lead to the high GPP IAV in the Northern Amazon and contribute to the overall high IAV in MPI-ESM-LR (Wang, Sun, and Mei, 2011).

To examine the role of climate forcing in driving the differences in GPP variability across different model structures, we compare soil moisture IAV (Figure B.5) with GPP IAV. Notable is the relationship between soil moisture and GPP variability in Australia and Southern Africa. MPI-ESL-LR and IPSL-CM6A-LR which have the highest GPP IAV in Australia, have low soil moisture IAV compared to the CLM family. We see similar results for Southern Africa, where all models but CMCC-CM2-SR5 and IPSL-CM6A-LR have relatively high soil moisture IAV, however, GPP IAV is low in the CLM family and high in IPSL-CM6A-LR. This disagreement between the variability of GPP and its forcing is in accordance with the findings of Peano et al. (2021), supporting the assumption that the response of GPP to soil moisture is not well constrained in semi-arid ecosystems. In CESM2, the high soil moisture variability in Australia and Southern Africa

despite low GPP IAV results from its low climate sensitivity (Wieder et al., 2021).

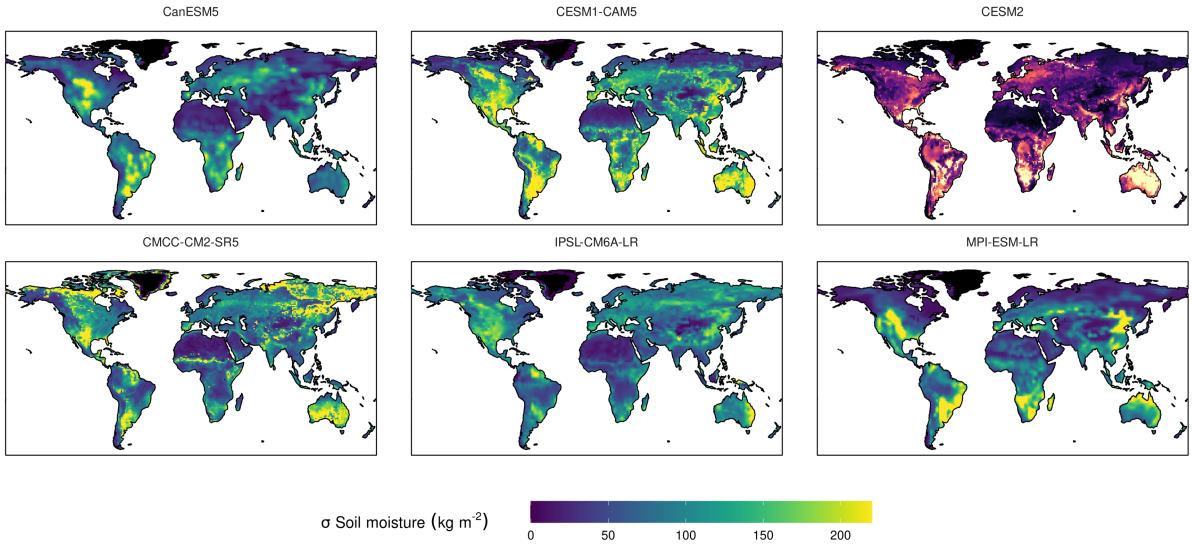

Figure B.5: Interannual variability of soil moisture in 6 ESMs. Note that CESM2 calculates soil moisture over a deeper soil column, hence the variability of CESM2 is scaled to a similar range as the other models.

B.3.2 *Drivers of GPP variability*

We analysed the sensitivity of GPP to environmental drivers by using regression analysis. The globally averaged contribution of the drivers to GPP variability is shown as the bars in Figure B.6. The CLM family and CanESM5 show similar patterns, with temperature dominating, or being on par with soil moisture. IPSL-CM6A-LR and MPI-EMS-LR show a distinctly different pattern, where soil moisture dominates variability and radiation contributes equally or more than temperature. A reason for the large contribution of soil moisture to GPP IAV in IPSL-CM6A-LR and MPI-ESM-LR could be that both ESMs are at the high end of soil moisture IAV for deep soil layers in the Southern Hemisphere (Qiao, Zuo, and Xiao, 2022), where many of the water-limited semi-arid ecosystems are located that contribute most to GPP IAV. Another explanation could be that from eleven CMIP6 models, IPSL-CM6A-LR and MPI-ESM-LR have the lowest warm-season soil moisture (Padrón et al., 2022). This increase in dryness can lead to a larger extent of semi-arid ecosystems with a generally higher GPP variability. Another

effect of the reduced warm-season soil moisture can be an increase in land-atmosphere coupling strength (Santanello et al., 2018). This would explain the higher correlation between soil moisture and temperature in these models (Padrón et al., 2022), and make the regression coefficients shift towards the stronger predictor – soil moisture.

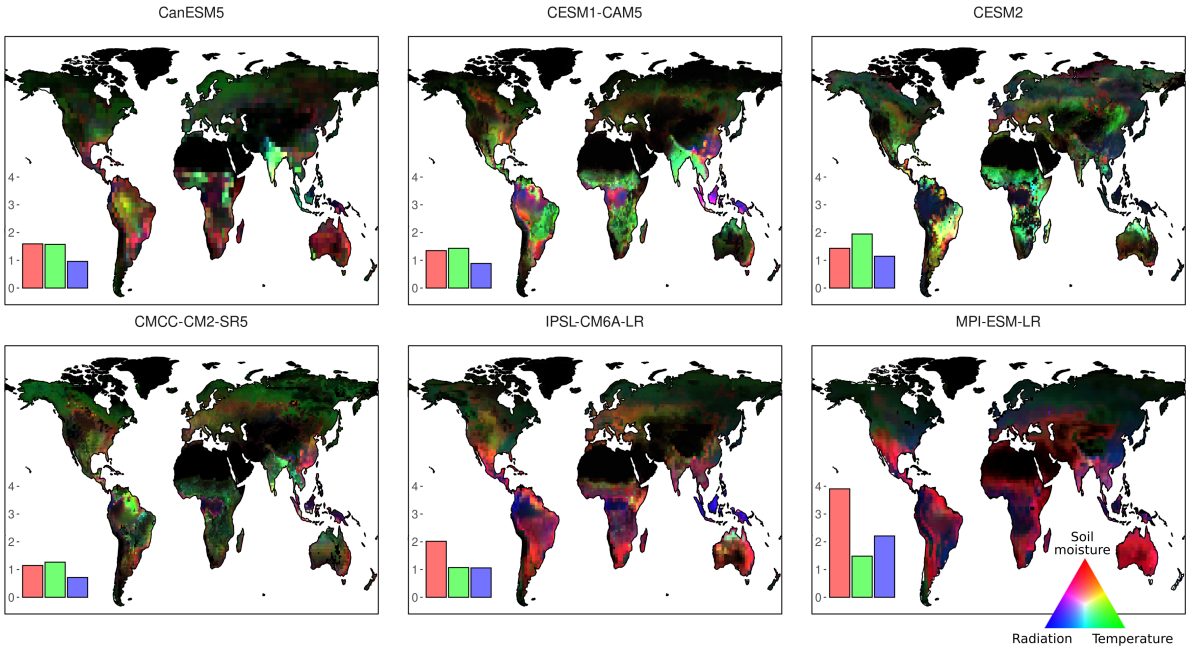

Figure B.6: The contribution of environmental variables to GPP variability ($\sigma GPP^{ENV}_{(clim)}$). Colour intensity stands for higher GPP variability. The data is scaled to every model in order to highlight regional differences and not the absolute differences. Bars represent the mean contribution of environmental variables to global GPP variability (kg C s^{-1} m^{-2} 10^{-13}).

The spatial drivers of GPP variability show agreements in equatorial and arid tropics, while there is less consistency in the transition zones. In many models, the variability in the wet tropics, and eastern China is induced by radiation, while soil moisture becomes more prevalent along the aridity gradient, and is driving variability in Southern Africa, Southern South America, and Australia (Fig. B.6). Variability on the remaining land surface is driven predominantly by soil moisture in IPSL-CM6A-LR and MPI-ESM-LR and by a combination of temperature and soil moisture in the remaining models.

Multi models averages and observations of GPP sensitivity agree with the larger role of temperature in tropical forests, radi-

ation in western Amazonia, and the importance of precipitation in the semi-arid tropics (Anav et al., 2015; O'Sullivan et al., 2020). However, the role of water on carbon fluxes increases when soil moisture is used instead of precipitation in sensitivity studies (Piao et al., 2020). This can be observed in the sensitivity of net biome productivity (NBP), showing a more balanced contribution of soil moisture and temperature in the tropical forests (Padrón et al., 2022; Piao et al., 2020). Although the comparison of GPP and NBP imposes limitations, GPP explains the majority of tropical NBP (Ahlström et al., 2015). This suggests, that the low water sensitivity of tropical GPP might explain the lower than expected GPP variability of tropical forests.

B.3.3 *Predictability of GPP*

To analyse the role of GPP in the predictability of atmospheric CO_2, we assessed GPP predictability using two metrics. The predictable fraction (pfGPP) is the ratio of predictable variability to IAV and illustrates how well information from the initialization is retained. Although this metric can be used to compare the predictive performance of different biomes, for example, it is not suitable to assess the predictability of cumulative carbon fluxes, since the atmospheric variability of CO_2 is determined by a few regions with high variability. Biomes like deserts, for example, have a very high predictable fraction, however, their carbon fluxes contribute little to the variability of atmospheric CO_2. To assess the predictability of cumulative GPP fluxes, the predictable component ($\Delta\sigma$GPP) is used. Calculated as the difference between ensemble variability and IAV, it provides a measure of absolute predictable variability.

There is relatively high consistency among the pfGPP of the environmental drivers across the models ($pf\text{GPP}^{Soil\ moisture} > pf\text{GPP}^{Temperature} > pf\text{GPP}^{Radiation}$, numbers above the bars in Fig. B.7). This pattern reflects the anticipated differences in predictability among the drivers. Atmospheric anomalies have a low persistence, leading to a low predictability of two weeks for most regions (Zeng et al., 2008). Soil hydrology, on the other hand, acts as a low-pass filter which removes the unpredictable high-frequency variability of precipitation and allows a predictability of soil moisture of around two years (Chikamoto et al., 2017). Temperature gains most of its predictability through sea surface temperature (SST) forcing in the equatorial regions (Feng, Del-

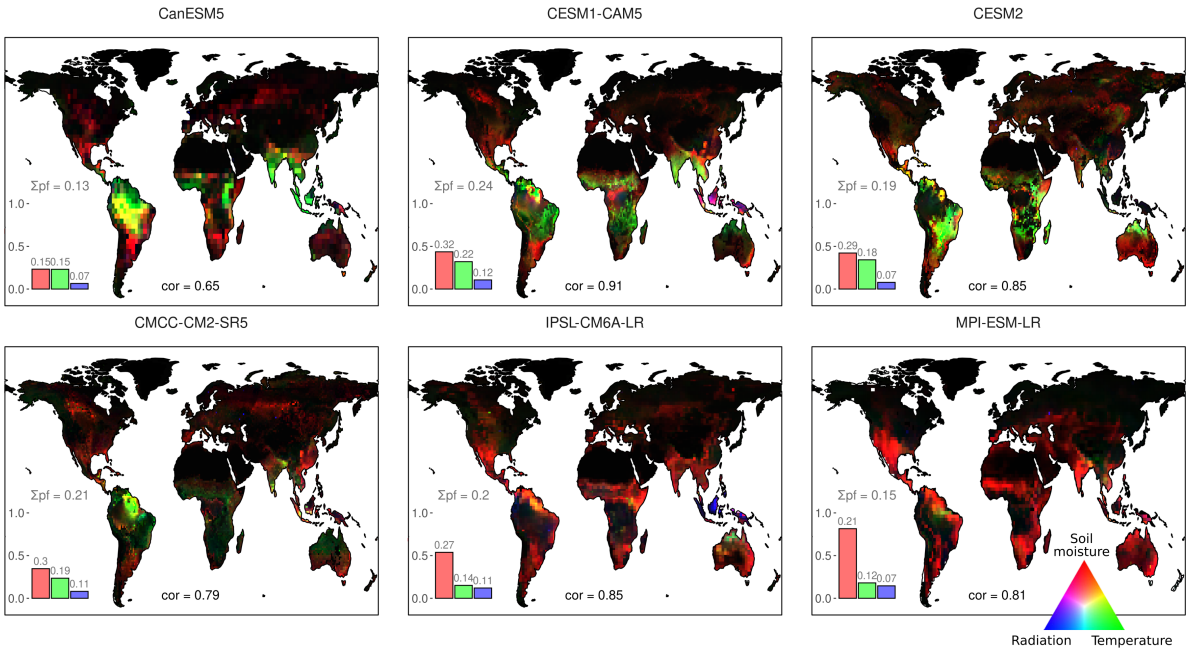

Figure B.7: The contribution of environmental variables to the predictable component of GPP ($\Delta\sigma GPP^{ENV}_{(y=1)}$). The contribution is calculated as the difference between the climatological variability and the variability within the first year of the hindcast experiments. Values are scaled for each model. Bars represent the mean contribution of environmental variables to the predictable component ($\Delta\sigma$ GPP in kg C s^{-1} m^{-2} 10^{-13}). Numbers on top of the bars show the predictable fraction (pf), which is the share of the predictable component to overall variability. The correlation between GPP variability and the predictable component is shown at the bottom of the plots.

Sole, and Houser, 2011), and land-atmosphere coupling in the semi-arid tropics (Seo et al., 2019).

The overall pfGPP of CESM2, CMCC-CM2-SR5 and IPSL-CM6A-LR falls into a narrow window of 0.19 to 0.21. With a value of 0.24, CESM1-CAM5 has the highest pfGPP among the models. It is likely that this increased share of predictable variance is not due to differences in model structure, but due to the large number of 40 ensemble members. Most other models in this study have only ten ensemble members, which is not enough to capture the difference in variability between hindcast and model climatology, so that an increase in ensemble members leads to an increase in prediction skill (Meehl et al., 2021). However, despite having 20 ensemble members, CanESM5 has the lowest pfGPP among the models. A possible explanation

could be its poor representation of soil moisture (Qiao, Zuo, and Xiao, 2022). In particular, the low variability of deep soil moisture in CanESM5 could hinder the persistence of the initial climatic conditions. On the other hand, a high variability of soil moisture does not guarantee a high pfGPP, as seen by the example of MPI-ESM-LR. Another strong controller of overall pfGPP is the sensitivity of GPP to radiation. Because only 7% to 12% of the radiation-induced variability is predictable, a high share of $\sigma GPP^{Radiation}$ reduces the predictability of GPP. This phenomenon explains the low pfGPP in MPI-ESM-LR, in which the share of $\sigma GPP^{Radiation}$ is 20% higher than in the other models.

We find a high overlap in the regions contributing to cumulative GPP predictability and GPP variability. The correlation between predictable component and variability exceeds 0.79 in all models but CanESM5. Indeed, these high correlations between predictability and variability align with our understanding. Under a constant predictable fraction, the predictable component would grow linearly with an increasing variability, leading to a perfect correlation. However, these high correlations show that the predictability of atmospheric CO_2 is determined more by the differences in GPP variability than the differences in the predictable fraction of GPP. While the pfGPP values show that the different ESMs have a similar degree of memory retention, there are few overlaps in the spatial distribution of the predictive component. To quantify the disagreement in predictability patterns, we separated the top 20% of grid cells contributing to the predictable component of GPP, as we did with variability in section 3.1. With 74% of high-predictability grid cells unique to only one model, overlap in high-predictability areas is even lower than the overlap of high-variability areas.

Although the spatial patterns of the predictable component broadly resemble the patterns of GPP variability, there are some slight differences between these fields. The predictable component is relatively high along the northeastern coast of South America in most ESMs. This could be due to the high climate predictability caused by slowly evolving Atlantic SST patterns (Dirmeyer, Halder, and Bombardi, 2018). Other systematic differences can be explained by the differing predictable components of the environmental drivers. The most evident is the difference between variability and predictability in regions where GPP variability is driven by radiation. This leads to relatively low predictability in the tropical rainforests of the western Amazon

basin and the Congo basin. An exception is the predictability provided through radiation on the Southeast Asian islands in IPSL-CM6A-LR and CESM1-CAM5. A plausible explanation is the proximity to the ENSO region. Strong and predictable SST anomalies in the tropical Pacific that surround the islands could have a direct influence on the cloud cover over land as well. The predictable component is also higher over areas where variability is driven by soil moisture rather than temperature. In many ESMs, this leads to a high predictable component in the semiarid regions of South America, Africa and India.

B.4 CONCLUSIONS

As the dominating driver of atmospheric CO_2 variability, the accurate representation of terrestrial GPP and its predictability are conducive to a variety of applications concerning the IAV of atmospheric CO_2 concentrations. Differences in GPP predictions produced by ESMs can not only be caused by how well the models are able to retain memory, but also by what these models are predicting in the first place. Indeed, the fraction of GPP variability which can be predicted is relatively consistent among models. Between 13% and 24% of the GPP variability can be predicted one year in advance on a global average among the models, with four out of six models between 19% and 24%. The predictable fraction is up to 32% for the GPP variability caused by soil moisture, while only 7% to 12% of the variability caused by radiation is predictable.

However, there is less agreement in the spatial distribution and the drivers of GPP variability. Although in all ESMs the semi-arid tropics are causing most GPP variability, the models have their own high-variability regions with little overlap. We find large disparities in the role of Australia, Southern Africa and central South America on GPP variability. Consequentially, when ESMs are used to predict the atmospheric growth rate of CO_2, their predictions are originating from different parts of the globe. The leading cause of the uncertainties in GPP variability are differences in the response to soil moisture. These differences materialize through the direct effect of soil moisture on photosynthesis and through the role of soil moisture on phenology.

While the distribution of mean GPP has long been used to parameterize ESMs, future efforts should also be directed towards tuning the variability of GPP in order to increase the predictive

performance of ESMs. A missing piece towards this goal, however, is a robust and independent product that quantifies global GPP variability.

B.5 SUPPLEMENTS

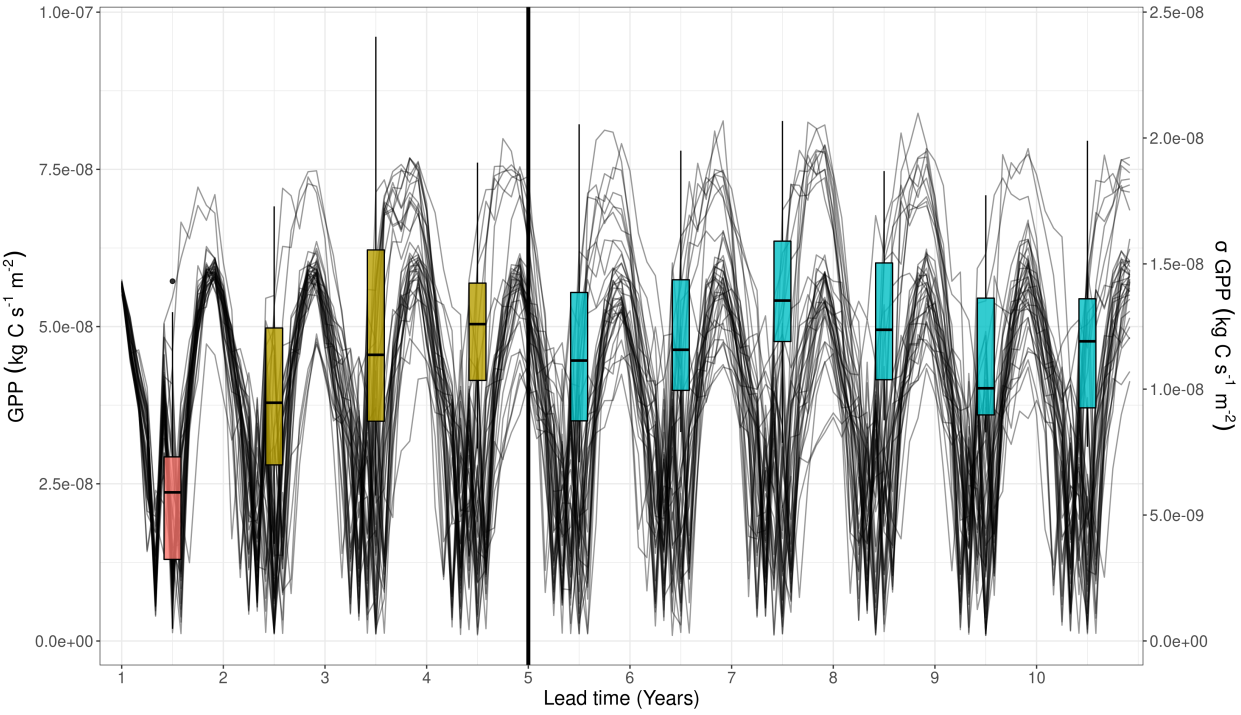

Figure B.8: Exemplary GPP hindcast from CESM1-CAM5 in India; a region with high predictability. The lines show the temporal evolution of 40 ensemble members. The ensemble variability at every lead years is shown as the boxes (Monthly standard deviation of ensemble averaged over every lead year. Axis on the right.). Even in regions with good predictability, the ensemble variability reaches the plateau after three to four years. In this analysis, the model climatology is calculated from the lead years 5 to 10 of the hindcast simulations (On the right of the black vertical line).

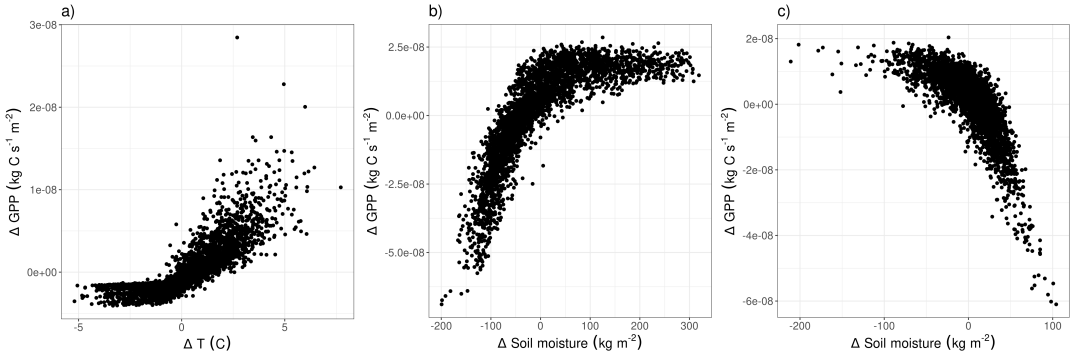

Figure B.9: Examples of a non-linear relationship of GPP with environmental drivers in IPSL-CM6A-LR. The examples are from the GPP in June in a) northern Canada, where plant growth can be halted by subzero temperatures, b) Venezuela and c) Indonesia where GPP has a nonlinear relationship with soil moisture. All axis show anomalies.

C

ENSO-INDUCED PATTERNS OF GROSS PRIMARY PRODUCTION

The work in this appendix describes the methods used for the results of chapter 4.

ENSO-induced Patterns of Gross Primary Production

C.1 METHODS

I compare the role of El Niño Southern Oscillation (ENSO) on gross primary production (GPP) in different Earth system models (ESMs). In order to have a large sample size of ENSO events, I use unforced piControl simulations. The list of ESMs and variant labels are listed in Table C.1. The ESMs are compared with results from upscaled flux tower measurements (FLUXCOM version: RS_METEO.FP-ALL.MLM-ALL.METEO-ERA5, Jung et al. 2019), and SST reanalysis data (HadISST, Rayner et al. 2003)

Some of the piControl simulations showed spin-up effects or strong decadal variability. To remove this unwanted variability, I calculated the 30-year running mean of all input fields. The FLUXCOM and HadISST data are linearly detrended. To quantify the strength of ENSO, I calculated the mean annual surface temperature in the Niño3.4 region.

I use linear regression to calculate the sensitivity of globally accumulated GPP to 1°C SST anomaly in the Niño3.4 region.

For all ESMs, I create a composite El Niño event, by averaging all years that I classified as an El Niño year. I did not use a temperature threshold for El Niño classification, because of the different SST ranges between the ESMs. Instead, I select all years, in which the Niño3.4 SST anomaly falls in the top 10% quantile. Because the interest of this analysis is on regional differences rather than absolute differences, all composites are scaled to a global GPP anomaly of -1 PgC. I use the IPCC climate reference regions to quantify the spatial differences (Iturbide et al., 2020) and select the six regions with the largest standard deviation among the ESMs for the remaining analysis.

To calculate the ENSO-induced changes in soil moisture, and the sensitivity of GPP to soil moisture, I calculate the annual anomalies of all fields by subtracting the climatology. Then, I use regression analysis with zero intercept to calculate the change in soil moisture to 1°C SST anomaly in the Niño3.4 region and the change in GPP to 1 kg soil moisture anomaly. I average the resulting sensitivities for every ESM and region. To calculate

their relative contribution to the uncertainties, I compare the coefficient of variation for both sensitivities in all regions.

Table C.1: The ESMs and their experiment IDs used in this study.

ESM	Variant label	Reference
ACCESS-ESM1-5	r1i1p1f1	Ziehn et al. (2020)
AWI-ESM-1-1-LR	r1i1p1f1	Shi et al. (2020)
BCC-CSM2-MR	r1i1p1f1	Wu et al. (2019)
CanESM5	r1i1p1f1	Swart et al. (2019)
CESM2	b.e21.B1850.f09_g17	Danabasoglu et al. (2020)
	CMIP6-piControl.001	
CMCC-ESM2	r1i1p1f1	Cherchi et al. (2019)
CNRM-ESM2-1	r1i1p1f2	Séférian et al. (2019)
E3SM-1-1	r1i1p1f1	Golaz et al. (2019)
GISS-E2-2-G	r1i1p1f1	Orbe et al. (2020)
ICON-ESM-LR	r1i1p1f1	Jungclaus et al. (2022)
IPSL-CM6A-LR	r1i1p1f1	Boucher et al. (2020)
MPI-ESM1-2-HR	r1i1p1f1	Müller et al. (2018)
MPI-ESM1-2-LR	r1i1p1f1	Mauritsen et al. (2019)
MRI-ESM2-0	r1i2p1f1	Yukimoto et al. (2019)
NorESM2-LM	r1i1p1f1	Seland et al. (2020)
NorESM2-MM	r1i1p1f1	Seland et al. (2020)
UKESM1-0-LL	r1i1p1f2	Sellar et al. (2019)

BIBLIOGRAPHY

Ahlström, A., M. R. Raupach, G. Schurgers, B. Smith, A. Arneth, M. Jung, M. Reichstein, J. G. Canadell, P. Friedlingstein, A. K. Jain, E. Kato, B. Poulter, S. Sitch, B. D. Stocker, N. Viovy, Y. P. Wang, A. Wiltshire, S. Zaehle, and N. Zeng (2015). "The dominant role of semi-arid ecosystems in the trend and variability of the land CO2 sink." *Science*. DOI: 10.1126/science.aaa1668.

Alessandri, A. and A. Navarra (2008). "On the coupling between vegetation and rainfall inter-annual anomalies: Possible contributions to seasonal rainfall predictability over land areas." *Geophysical Research Letters* 35.2. DOI: https://doi.org/10.1029/2007GL032415.

Anav, A., P. Friedlingstein, C. Beer, P. Ciais, A. Harper, C. Jones, G. Murray-Tortarolo, D. Papale, N. C. Parazoo, P. Peylin, S. Piao, S. Sitch, N. Viovy, A. Wiltshire, and M. Zhao (2015). "Spatiotemporal patterns of terrestrial gross primary production: A review." *Reviews of Geophysics* 53.3, pp. 785–818. DOI: https://doi.org/10.1002/2015RG000483.

Ardilouze, C., L. Batté, F. Bunzel, D. Decremer, M. Déqué, F. J. Doblas-Reyes, H. Douville, D. Fereday, V. Guemas, C. MacLachlan, W. Müller, and C. Prodhomme (2017). "Multi-model assessment of the impact of soil moisture initialization on mid-latitude summer predictability." *Climate Dynamics* 49.11, pp. 3959–3974. DOI: 10.1007/s00382-017-3555-7.

Aubry-Kientz, M., V. Rossi, F. Wagner, and B. Hérault (2015). "Identifying climatic drivers of tropical forest dynamics." *Biogeosciences* 12.19, pp. 5583–5596. DOI: 10.5194/bg-12-5583-2015.

Bacastow, R. B. (1976). "Modulation of atmospheric carbon dioxide by the Southern Oscillation." *Nature* 261.5556, pp. 116–118. DOI: 10.1038/261116a0.

Baldocchi, D., H. Chu, and M. Reichstein (2018). "Inter-annual variability of net and gross ecosystem carbon fluxes: A review." *Agricultural and Forest Meteorology* 249, pp. 520–533. DOI: 10.1016/j.agrformet.2017.05.015.

Baldocchi, D., R. Valentini, S. Running, W. Oechel, and R. Dahlman (1996). "Strategies for measuring and modelling carbon dioxide and water vapour fluxes over terrestrial ecosystems."

Global Change Biology 2.3, pp. 159–168. DOI: https://doi.org/10.1111/j.1365-2486.1996.tb00069.x.

Balmaseda, M. A., K. Mogensen, and A. T. Weaver (2013). "Evaluation of the ECMWF ocean reanalysis system ORAS4." *Quarterly Journal of the Royal Meteorological Society* 139.674, pp. 1132–1161. DOI: https://doi.org/10.1002/qj.2063.

Banzon, V., T. M. Smith, T. M. Chin, C. Liu, and W. Hankins (2016). "A long-term record of blended satellite and in situ sea-surface temperature for climate monitoring, modeling and environmental studies." *Earth System Science Data* 8.1, pp. 165–176. DOI: 10.5194/essd-8-165-2016.

Barnston, A. G., M. K. Tippett, M. Ranganathan, and M. L. L'Heureux (2019). "Deterministic skill of ENSO predictions from the North American Multimodel Ensemble." *Climate Dynamics* 53.12, pp. 7215–7234. DOI: 10.1007/s00382-017-3603-3.

Bastos, A., S. W. Running, C. Gouveia, and R. M. Trigo (2013). "The global NPP dependence on ENSO: La Niña and the extraordinary year of 2011." *Journal of Geophysical Research: Biogeosciences* 118.3, pp. 1247–1255. DOI: https://doi.org/10.1002/jgrg.20100.

Bastos, A., P. Friedlingstein, S. Sitch, C. Chen, A. Mialon, J.-P. Wigneron, V. K. Arora, P. R. Briggs, J. G. Canadell, P. Ciais, F. Chevallier, L. Cheng, C. Delire, V. Haverd, A. K. Jain, F. Joos, E. Kato, S. Lienert, D. Lombardozzi, J. R. Melton, R. Myneni, J. E. M. S. Nabel, J. Pongratz, B. Poulter, C. Rödenbeck, R. Séférian, H. Tian, C. van Eck, N. Viovy, N. Vuichard, A. P. Walker, A. Wiltshire, J. Yang, S. Zaehle, N. Zeng, and D. Zhu (2018). "Impact of the 2015/2016 El Niño on the terrestrial carbon cycle constrained by bottom-up and top-down approaches." *Philosophical Transactions of the Royal Society B: Biological Sciences* 373.1760, p. 20170304. DOI: 10.1098/rstb.2017.0304.

Becker, E. J., H. van den Dool, and M. Peña (2013). "Short-Term Climate Extremes: Prediction Skill and Predictability." *Journal of Climate* 26.2, pp. 512–531. DOI: 10.1175/JCLI-D-12-00177.1.

Beer, C., M. Reichstein, E. Tomelleri, P. Ciais, M. Jung, N. Carvalhais, C. Rödenbeck, M. A. Arain, D. Baldocchi, G. B. Bonan, A. Bondeau, A. Cescatti, G. Lasslop, A. Lindroth, M. Lomas, S. Luyssaert, H. Margolis, K. W. Oleson, O. Roupsard, E. Veenendaal, N. Viovy, C. Williams, F. I. Woodward, and D. Papale (2010). "Terrestrial Gross Carbon Dioxide Uptake:

Global Distribution and Covariation with Climate." *Science*. DOI: 10.1126/science.1184984.

Bellucci, A., R. Haarsma, N. Bellouin, B. Booth, C. Cagnazzo, B. v. d. Hurk, N. Keenlyside, T. Koenigk, F. Massonnet, S. Materia, and M. Weiss (2015). "Advancements in decadal climate predictability: The role of nonoceanic drivers." *Reviews of Geophysics* 53.2, pp. 165–202. DOI: https://doi.org/10.1002/2014RG000473.

Beobide-Arsuaga, G., T. Bayr, A. Reintges, and M. Latif (2021). "Uncertainty of ENSO-amplitude projections in CMIP5 and CMIP6 models." *Climate Dynamics* 56.11, pp. 3875–3888. DOI: 10.1007/s00382-021-05673-4.

Berkelhammer, M., D. Asaf, C. Still, S. Montzka, D. Noone, M. Gupta, R. Provencal, H. Chen, and D. Yakir (2014). "Constraining surface carbon fluxes using in situ measurements of carbonyl sulfide and carbon dioxide." *Global Biogeochemical Cycles* 28.2, pp. 161–179. DOI: https://doi.org/10.1002/2013GB004644.

Betts, R. A., C. D. Jones, J. R. Knight, R. F. Keeling, and J. J. Kennedy (2016). "El Niño and a record CO2 rise." *Nature Climate Change* 6.9, pp. 806–810. DOI: 10.1038/nclimate3063.

Bloom, A. A., J.-F. Exbrayat, I. R. van der Velde, L. Feng, and M. Williams (2016). "The decadal state of the terrestrial carbon cycle: Global retrievals of terrestrial carbon allocation, pools, and residence times." *Proceedings of the National Academy of Sciences of the United States of America* 113.5, pp. 1285–1290. DOI: 10.1073/pnas.1515160113.

Boer, G. J., V. V. Kharin, and W. J. Merryfield (2013). "Decadal predictability and forecast skill." *Climate Dynamics* 41.7-8, pp. 1817–1833. DOI: 10.1007/s00382-013-1705-0.

Boer, G. J., D. M. Smith, C. Cassou, F. Doblas-Reyes, G. Danabasoglu, B. Kirtman, Y. Kushnir, M. Kimoto, G. A. Meehl, R. Msadek, W. A. Mueller, K. E. Taylor, F. Zwiers, M. Rixen, Y. Ruprich-Robert, and R. Eade (2016). "The Decadal Climate Prediction Project (DCPP) contribution to CMIP6." *Geoscientific Model Development* 9.10, pp. 3751–3777. DOI: 10.5194/gmd-9-3751-2016.

Bonan, G. B. and S. C. Doney (2018). "Climate, ecosystems, and planetary futures: The challenge to predict life in Earth system models." *Science*. DOI: 10.1126/science.aam8328.

Bonan, G. B., D. L. Lombardozzi, W. R. Wieder, K. W. Oleson, D. M. Lawrence, F. M. Hoffman, and N. Collier (2019). "Model Structure and Climate Data Uncertainty in Histori-

cal Simulations of the Terrestrial Carbon Cycle (1850–2014)." *Global Biogeochemical Cycles* 33.10, pp. 1310–1326. DOI: https://doi.org/10.1029/2019GB006175.

Boucher, O., J. Servonnat, A. L. Albright, O. Aumont, Y. Balkanski, V. Bastrikov, S. Bekki, R. Bonnet, S. Bony, L. Bopp, P. Braconnot, P. Brockmann, P. Cadule, A. Caubel, F. Cheruy, F. Codron, A. Cozic, D. Cugnet, F. D'Andrea, P. Davini, C. d. Lavergne, S. Denvil, J. Deshayes, M. Devilliers, A. Ducharne, J.-L. Dufresne, E. Dupont, C. Éthé, L. Fairhead, L. Falletti, S. Flavoni, M.-A. Foujols, S. Gardoll, G. Gastineau, J. Ghattas, J.-Y. Grandpeix, B. Guenet, L. Guez E., E. Guilyardi, M. Guimberteau, D. Hauglustaine, F. Hourdin, A. Idelkadi, S. Joussaume, M. Kageyama, M. Khodri, G. Krinner, N. Lebas, G. Levavasseur, C. Lévy, L. Li, F. Lott, T. Lurton, S. Luyssaert, G. Madec, J.-B. Madeleine, F. Maignan, M. Marchand, O. Marti, L. Mellul, Y. Meurdesoif, J. Mignot, I. Musat, C. Ottlé, P. Peylin, Y. Planton, J. Polcher, C. Rio, N. Rochetin, C. Rousset, P. Sepulchre, A. Sima, D. Swingedouw, R. Thiéblemont, A. K. Traore, M. Vancoppenolle, J. Vial, J. Vialard, N. Viovy, and N. Vuichard (2020). "Presentation and Evaluation of the IPSL-CM6A-LR Climate Model." *Journal of Advances in Modeling Earth Systems* 12.7, e2019MS002010. DOI: https://doi.org/10.1029/2019MS002010.

Brady, R. and A. Spring (2021). "climpred: Verification of weather and climate forecasts." *Journal of Open Source Software* 6.59, p. 2781. DOI: 10.21105/joss.02781.

Carrassi, A., M. Bocquet, L. Bertino, and G. Evensen (2018). "Data assimilation in the geosciences: An overview of methods, issues, and perspectives." *WIREs Climate Change* 9.5, e535. DOI: https://doi.org/10.1002/wcc.535.

Chadburn, S. E., E. J. Burke, P. M. Cox, P. Friedlingstein, G. Hugelius, and S. Westermann (2017). "An observation-based constraint on permafrost loss as a function of global warming." *Nature Climate Change* 7.5, pp. 340–344. DOI: 10.1038/nclimate3262.

Chen, M., R. Rafique, G. R. Asrar, B. Bond-Lamberty, P. Ciais, F. Zhao, C. P. O. Reyer, S. Ostberg, J. Chang, A. Ito, J. Yang, N. Zeng, E. Kalnay, T. West, G. Leng, L. Francois, G. Munhoven, A. Henrot, H. Tian, S. Pan, K. Nishina, N. Viovy, C. Morfopoulos, R. Betts, S. Schaphoff, J. Steinkamp, and T. Hickler (2017). "Regional contribution to variability and trends of global gross primary productivity." *Environmental Research Letters* 12.10, p. 105005. DOI: 10.1088/1748-9326/aa8978.

Chen, S., Y. Huang, J. Zou, Q. Shen, Z. Hu, Y. Qin, H. Chen, and G. Pan (2010). "Modeling interannual variability of global soil respiration from climate and soil properties." *Agricultural and Forest Meteorology* 150.4, pp. 590–605. DOI: 10.1016/j.agrformet.2010.02.004.

Chen, W. Y. and H. M. V. d. Dool (1997). "Atmospheric Predictability of Seasonal, Annual, and Decadal Climate Means and the Role of the ENSO Cycle: A Model Study." *Journal of Climate* 10.6, pp. 1236–1254. DOI: 10.1175/1520-0442(1997)010<1236:APOSAA>2.0.CO;2.

Cherchi, A., P. G. Fogli, T. Lovato, D. Peano, D. Iovino, S. Gualdi, S. Masina, E. Scoccimarro, S. Materia, A. Bellucci, and A. Navarra (2019). "Global Mean Climate and Main Patterns of Variability in the CMCC-CM2 Coupled Model." *Journal of Advances in Modeling Earth Systems* 11.1, pp. 185–209. DOI: https://doi.org/10.1029/2018MS001369.

Cheruy, F., A. Ducharne, F. Hourdin, I. Musat, Vignon, G. Gastineau, V. Bastrikov, N. Vuichard, B. Diallo, J.-L. Dufresne, J. Ghattas, J.-Y. Grandpeix, A. Idelkadi, L. Mellul, F. Maignan, M. Ménégoz, C. Ottlé, P. Peylin, J. Servonnat, F. Wang, and Y. Zhao (2020). "Improved Near-Surface Continental Climate in IPSL-CM6A-LR by Combined Evolutions of Atmospheric and Land Surface Physics." *Journal of Advances in Modeling Earth Systems* 12.10, e2019MS002005. DOI: https://doi.org/10.1029/2019MS002005.

Chikamoto, Y., A. Timmermann, S. Stevenson, P. DiNezio, and S. Langford (2015). "Decadal predictability of soil water, vegetation, and wildfire frequency over North America." *Climate Dynamics* 45.7, pp. 2213–2235. DOI: 10.1007/s00382-015-2469-5.

Chikamoto, Y., A. Timmermann, M. J. Widlansky, M. A. Balmaseda, and L. Stott (2017). "Multi-year predictability of climate, drought, and wildfire in southwestern North America." *Scientific Reports* 7.1, p. 6568. DOI: 10.1038/s41598-017-06869-7.

Ciais, P. et al. (2013). *Carbon and Other Biogeochemical Cycles*. Cambridge University Press. ISBN: 978-1-107-05799-9.

Coleman, K., D. S. Jenkinson, G. J. Crocker, P. R. Grace, J. Klír, M. Körschens, P. R. Poulton, and D. D. Richter (1997). "Simulating trends in soil organic carbon in long-term experiments using RothC-26.3." *Geoderma*. Evaluation and Comparison of Soil Organic Matter Models 81.1, pp. 29–44. DOI: 10.1016/S0016-7061(97)00079-7.

Collalti, A., A. Ibrom, A. Stockmarr, A. Cescatti, R. Alkama, M. Fernández-Martínez, G. Matteucci, S. Sitch, P. Friedlingstein, P. Ciais, D. S. Goll, J. E. M. S. Nabel, J. Pongratz, A. Arneth, V. Haverd, and I. C. Prentice (2020). "Forest production efficiency increases with growth temperature." *Nature Communications* 11.1, p. 5322. DOI: 10.1038/s41467-020-19187-w.

Collier, N., F. M. Hoffman, D. M. Lawrence, G. Keppel-Aleks, C. D. Koven, W. J. Riley, M. Mu, and J. T. Randerson (2018). "The International Land Model Benchmarking (ILAMB) System: Design, Theory, and Implementation." *Journal of Advances in Modeling Earth Systems* 10.11, pp. 2731–2754. DOI: https://doi.org/10.1029/2018MS001354.

Collins, M. and B. Sinha (2003). "Predictability of decadal variations in the thermohaline circulation and climate." *Geophysical Research Letters* 30.6. DOI: https://doi.org/10.1029/2002GL016504.

Danabasoglu, G., J.-F. Lamarque, J. Bacmeister, D. A. Bailey, A. K. DuVivier, J. Edwards, L. K. Emmons, J. Fasullo, R. Garcia, A. Gettelman, C. Hannay, M. M. Holland, W. G. Large, P. H. Lauritzen, D. M. Lawrence, J. T. M. Lenaerts, K. Lindsay, W. H. Lipscomb, M. J. Mills, R. Neale, K. W. Oleson, B. Otto-Bliesner, A. S. Phillips, W. Sacks, S. Tilmes, L. v. Kampenhout, M. Vertenstein, A. Bertini, J. Dennis, C. Deser, C. Fischer, B. Fox-Kemper, J. E. Kay, D. Kinnison, P. J. Kushner, V. E. Larson, M. C. Long, S. Mickelson, J. K. Moore, E. Nienhouse, L. Polvani, P. J. Rasch, and W. G. Strand (2020). "The Community Earth System Model Version 2 (CESM2)." *Journal of Advances in Modeling Earth Systems* 12.2, e2019MS001916. DOI: https://doi.org/10.1029/2019MS001916.

Dee, D. P., S. M. Uppala, A. J. Simmons, P. Berrisford, P. Poli, S. Kobayashi, U. Andrae, M. A. Balmaseda, G. Balsamo, P. Bauer, P. Bechtold, A. C. M. Beljaars, L. v. d. Berg, J. Bidlot, N. Bormann, C. Delsol, R. Dragani, M. Fuentes, A. J. Geer, L. Haimberger, S. B. Healy, H. Hersbach, E. V. Hólm, L. Isaksen, P. Kållberg, M. Köhler, M. Matricardi, A. P. McNally, B. M. Monge-Sanz, J.-J. Morcrette, B.-K. Park, C. Peubey, P. d. Rosnay, C. Tavolato, J.-N. Thépaut, and F. Vitart (2011). "The ERA-Interim reanalysis: configuration and performance of the data assimilation system." *Quarterly Journal of the Royal Meteorological Society* 137.656, pp. 553–597. DOI: https://doi.org/10.1002/qj.828.

Denissen, J. M. C., A. J. Teuling, A. J. Pitman, S. Koirala, M. Migliavacca, W. Li, M. Reichstein, A. J. Winkler, C. Zhan, and

R. Orth (2022). "Widespread shift from ecosystem energy to water limitation with climate change." *Nature Climate Change* 12.7, pp. 677–684. DOI: 10.1038/s41558-022-01403-8.

DiNezio, P. N., C. Deser, A. Karspeck, S. Yeager, Y. Okumura, G. Danabasoglu, N. Rosenbloom, J. Caron, and G. A. Meehl (2017). "A 2 Year Forecast for a 60–80% Chance of La Niña in 2017–2018." *Geophysical Research Letters* 44.22, pp. 11,624–11,635. DOI: https://doi.org/10.1002/2017GL074904.

Dirkson, A., W. J. Merryfield, and A. Monahan (2017). "Impacts of Sea Ice Thickness Initialization on Seasonal Arctic Sea Ice Predictions." *Journal of Climate* 30.3, pp. 1001–1017. DOI: 10.1175/JCLI-D-16-0437.1.

Dirmeyer, P. A., S. Halder, and R. Bombardi (2018). "On the Harvest of Predictability From Land States in a Global Forecast Model." *Journal of Geophysical Research: Atmospheres* 123.23, pp. 13,111–13,127. DOI: https://doi.org/10.1029/2018JD029103.

Donohue, R. J., M. L. Roderick, T. R. McVicar, and G. D. Farquhar (2013). "Impact of CO2 fertilization on maximum foliage cover across the globe's warm, arid environments." *Geophysical Research Letters* 40.12, pp. 3031–3035. DOI: https://doi.org/10.1002/grl.50563.

Estella-Perez, V., J. Mignot, E. Guilyardi, D. Swingedouw, and G. Reverdin (2020). "Advances in reconstructing the AMOC using sea surface observations of salinity." *Climate Dynamics* 55.3, pp. 975–992. DOI: 10.1007/s00382-020-05304-4.

Fang, Y., A. M. Michalak, C. R. Schwalm, D. N. Huntzinger, J. A. Berry, P. Ciais, S. Piao, B. Poulter, J. B. Fisher, R. B. Cook, D. Hayes, M. Huang, A. Ito, A. Jain, H. Lei, C. Lu, J. Mao, N. C. Parazoo, S. Peng, D. M. Ricciuto, X. Shi, B. Tao, H. Tian, W. Wang, Y. Wei, and J. Yang (2017). "Global land carbon sink response to temperature and precipitation varies with ENSO phase." *Environmental Research Letters* 12.6, p. 064007. DOI: 10.1088/1748-9326/aa6e8e.

Feng, X., T. DelSole, and P. Houser (2011). "Bootstrap estimated seasonal potential predictability of global temperature and precipitation." *Geophysical Research Letters* 38.7. DOI: https://doi.org/10.1029/2010GL046511.

Flato, G. M. (2011). "Earth system models: an overview." *WIREs Climate Change* 2.6, pp. 783–800. DOI: https://doi.org/10.1002/wcc.148.

Friedlingstein, P., M. O'Sullivan, M. W. Jones, R. M. Andrew, J. Hauck, A. Olsen, G. P. Peters, W. Peters, J. Pongratz, S. Sitch, C. Le Quéré, J. G. Canadell, P. Ciais, R. B. Jackson, S. Alin,

L. E. O. C. Aragão, A. Arneth, V. Arora, N. R. Bates, M. Becker, A. Benoit-Cattin, H. C. Bittig, L. Bopp, S. Bultan, N. Chandra, F. Chevallier, L. P. Chini, W. Evans, L. Florentie, P. M. Forster, T. Gasser, M. Gehlen, D. Gilfillan, T. Gkritzalis, L. Gregor, N. Gruber, I. Harris, K. Hartung, V. Haverd, R. A. Houghton, T. Ilyina, A. K. Jain, E. Joetzjer, K. Kadono, E. Kato, V. Kitidis, J. I. Korsbakken, P. Landschützer, N. Lefèvre, A. Lenton, S. Lienert, Z. Liu, D. Lombardozzi, G. Marland, N. Metzl, D. R. Munro, J. E. M. S. Nabel, S.-I. Nakaoka, Y. Niwa, K. O'Brien, T. Ono, P. I. Palmer, D. Pierrot, B. Poulter, L. Resplandy, E. Robertson, C. Rödenbeck, J. Schwinger, R. Séférian, I. Skjelvan, A. J. P. Smith, A. J. Sutton, T. Tanhua, P. P. Tans, H. Tian, B. Tilbrook, G. van der Werf, N. Vuichard, A. P. Walker, R. Wanninkhof, A. J. Watson, D. Willis, A. J. Wiltshire, W. Yuan, X. Yue, and S. Zaehle (2020). "Global Carbon Budget 2020." *Earth System Science Data* 12.4, pp. 3269–3340. DOI: 10.5194/essd-12-3269-2020.

Giorgetta, M. A., J. Jungclaus, C. H. Reick, S. Legutke, J. Bader, M. Böttinger, V. Brovkin, T. Crueger, M. Esch, K. Fieg, K. Glushak, V. Gayler, H. Haak, H.-D. Hollweg, T. Ilyina, S. Kinne, L. Kornblueh, D. Matei, T. Mauritsen, U. Mikolajewicz, W. Mueller, D. Notz, F. Pithan, T. Raddatz, S. Rast, R. Redler, E. Roeckner, H. Schmidt, R. Schnur, J. Segschneider, K. D. Six, M. Stockhause, C. Timmreck, J. Wegner, H. Widmann, K.-H. Wieners, M. Claussen, J. Marotzke, and B. Stevens (2013). "Climate and carbon cycle changes from 1850 to 2100 in MPI-ESM simulations for the Coupled Model Intercomparison Project phase 5." *Journal of Advances in Modeling Earth Systems* 5.3, pp. 572–597. DOI: https://doi.org/10.1002/jame.20038.

Golaz, J.-C., P. M. Caldwell, L. P. V. Roekel, M. R. Petersen, Q. Tang, J. D. Wolfe, G. Abeshu, V. Anantharaj, X. S. Asay-Davis, D. C. Bader, S. A. Baldwin, G. Bisht, P. A. Bogenschutz, M. Branstetter, M. A. Brunke, S. R. Brus, S. M. Burrows, P. J. Cameron-Smith, A. S. Donahue, M. Deakin, R. C. Easter, K. J. Evans, Y. Feng, M. Flanner, J. G. Foucar, J. G. Fyke, B. M. Griffin, C. Hannay, B. E. Harrop, M. J. Hoffman, E. C. Hunke, R. L. Jacob, D. W. Jacobsen, N. Jeffery, P. W. Jones, N. D. Keen, S. A. Klein, V. E. Larson, L. R. Leung, H.-Y. Li, W. Lin, W. H. Lipscomb, P.-L. Ma, S. Mahajan, M. E. Maltrud, A. Mametjanov, J. L. McClean, R. B. McCoy, R. B. Neale, S. F. Price, Y. Qian, P. J. Rasch, J. E. J. R. Eyre, W. J. Riley, T. D. Ringler, A. F. Roberts, E. L. Roesler, A. G. Salinger, Z. Shaheen, X. Shi, B. Singh, J. Tang, M. A. Taylor, P. E. Thornton,

A. K. Turner, M. Veneziani, H. Wan, H. Wang, S. Wang, D. N. Williams, P. J. Wolfram, P. H. Worley, S. Xie, Y. Yang, J.-H. Yoon, M. D. Zelinka, C. S. Zender, X. Zeng, C. Zhang, K. Zhang, Y. Zhang, X. Zheng, T. Zhou, and Q. Zhu (2019). "The DOE E3SM Coupled Model Version 1: Overview and Evaluation at Standard Resolution." *Journal of Advances in Modeling Earth Systems* 11.7, pp. 2089–2129. DOI: https://doi.org/10.1029/2018MS001603.

Good, S. A., M. J. Martin, and N. A. Rayner (2013). "EN4: Quality controlled ocean temperature and salinity profiles and monthly objective analyses with uncertainty estimates." *Journal of Geophysical Research: Oceans* 118.12, pp. 6704–6716. DOI: https://doi.org/10.1002/2013JC009067.

Griffies, S. M. and K. Bryan (1997). "A predictability study of simulated North Atlantic multidecadal variability." *Climate Dynamics* 13.7-8, pp. 459–487. DOI: 10.1007/s003820050177.

Grünzweig, J. M., H. J. De Boeck, A. Rey, M. J. Santos, O. Adam, M. Bahn, J. Belnap, G. Deckmyn, S. C. Dekker, O. Flores, D. Gliksman, D. Helman, K. R. Hultine, L. Liu, E. Meron, Y. Michael, E. Sheffer, H. L. Throop, O. Tzuk, and D. Yakir (2022). "Dryland mechanisms could widely control ecosystem functioning in a drier and warmer world." *Nature Ecology & Evolution* 6.8, pp. 1064–1076. DOI: 10.1038/s41559-022-01779-y.

Guo, Z. and P. A. Dirmeyer (2013). "Interannual Variability of Land–Atmosphere Coupling Strength." *Journal of Hydrometeorology* 14.5, pp. 1636–1646. DOI: 10.1175/JHM-D-12-0171.1.

Hagemann, S. and T. Stacke (2015). "Impact of the soil hydrology scheme on simulated soil moisture memory." *Climate Dynamics* 44.7, pp. 1731–1750. DOI: 10.1007/s00382-014-2221-6.

Harris, R. M. B., L. J. Beaumont, T. R. Vance, C. R. Tozer, T. A. Remenyi, S. E. Perkins-Kirkpatrick, P. J. Mitchell, A. B. Nicotra, S. McGregor, N. R. Andrew, M. Letnic, M. R. Kearney, T. Wernberg, L. B. Hutley, L. E. Chambers, M.-S. Fletcher, M. R. Keatley, C. A. Woodward, G. Williamson, N. C. Duke, and D. M. J. S. Bowman (2018). "Biological responses to the press and pulse of climate trends and extreme events." *Nature Climate Change* 8.7, pp. 579–587. DOI: 10.1038/s41558-018-0187-9.

Hashimoto, H., R. R. Nemani, M. A. White, W. M. Jolly, S. C. Piper, C. D. Keeling, R. B. Myneni, and S. W. Running (2004). "El Niño–Southern Oscillation–induced variability in terres-

trial carbon cycling." *Journal of Geophysical Research: Atmospheres* 109.D23. DOI: 10.1029/2004JD004959.

Holmgren, M., M. Scheffer, E. Ezcurra, J. R. Gutiérrez, and G. M. J. Mohren (2001). "El Niño effects on the dynamics of terrestrial ecosystems." *Trends in Ecology & Evolution* 16.2, pp. 89–94. DOI: 10.1016/S0169-5347(00)02052-8.

Hu, Q., T. Li, X. Deng, T. Wu, P. Zhai, D. Huang, X. Fan, Y. Zhu, Y. Lin, X. Xiao, X. Chen, X. Zhao, L. Wang, and Z. Qin (2022). "Intercomparison of global terrestrial carbon fluxes estimated by MODIS and Earth system models." *Science of The Total Environment* 810, p. 152231. DOI: 10.1016/j.scitotenv.2021.152231.

Hurrell, J. W., M. M. Holland, P. R. Gent, S. Ghan, J. E. Kay, P. J. Kushner, J.-F. Lamarque, W. G. Large, D. Lawrence, K. Lindsay, W. H. Lipscomb, M. C. Long, N. Mahowald, D. R. Marsh, R. B. Neale, P. Rasch, S. Vavrus, M. Vertenstein, D. Bader, W. D. Collins, J. J. Hack, J. Kiehl, and S. Marshall (2013). "The Community Earth System Model: A Framework for Collaborative Research." *Bulletin of the American Meteorological Society* 94.9, pp. 1339–1360. DOI: 10.1175/BAMS-D-12-00121.1.

Ilyina, T., H. Li, A. Spring, W. A. Müller, L. Bopp, M. O. Chikamoto, G. Danabasoglu, M. Dobrynin, J. Dunne, F. Fransner, P. Friedlingstein, W. Lee, N. S. Lovenduski, W. J. Merryfield, J. Mignot, J. Y. Park, R. Séférian, R. Sospedra-Alfonso, M. Watanabe, and S. Yeager (2021). "Predictable Variations of the Carbon Sinks and Atmospheric CO2 Growth in a Multi-Model Framework." *Geophysical Research Letters* 48.6, e2020GL090695. DOI: https://doi.org/10.1029/2020GL090695.

Iturbide, M., J. M. Gutiérrez, L. M. Alves, J. Bedia, R. Cerezo-Mota, E. Cimadevilla, A. S. Cofiño, A. Di Luca, S. H. Faria, I. V. Gorodetskaya, M. Hauser, S. Herrera, K. Hennessy, H. T. Hewitt, R. G. Jones, S. Krakovska, R. Manzanas, D. Martínez-Castro, G. T. Narisma, I. S. Nurhati, I. Pinto, S. I. Seneviratne, B. van den Hurk, and C. S. Vera (2020). "An update of IPCC climate reference regions for subcontinental analysis of climate model data: definition and aggregated datasets." *Earth System Science Data* 12.4, pp. 2959–2970. DOI: 10.5194/essd-12-2959-2020.

Jolliffe, I. T. and D. B. Stephenson (2012). *Forecast Verification: A Practitioner's Guide in Atmospheric Science*. 2nd. Chichester: John Wiley & Sons. ISBN: 978-1-119-96107-9.

Jones, C. D., M. Collins, P. M. Cox, and S. A. Spall (2001). "The Carbon Cycle Response to ENSO: A Coupled Climate–Carbon

Cycle Model Study." *Journal of Climate* 14.21, pp. 4113–4129. DOI: 10.1175/1520-0442(2001)014<4113:TCCRTE>2.0.CO;2.

Jung, M., S. Koirala, U. Weber, K. Ichii, F. Gans, G. Camps-Valls, D. Papale, C. Schwalm, G. Tramontana, and M. Reichstein (2019). "The FLUXCOM ensemble of global land-atmosphere energy fluxes." *Scientific Data* 6.1, p. 74. DOI: 10.1038/s41597-019-0076-8.

Jung, M., M. Reichstein, H. A. Margolis, A. Cescatti, A. D. Richardson, M. A. Arain, A. Arneth, C. Bernhofer, D. Bonal, J. Chen, D. Gianelle, N. Gobron, G. Kiely, W. Kutsch, G. Lasslop, B. E. Law, A. Lindroth, L. Merbold, L. Montagnani, E. J. Moors, D. Papale, M. Sottocornola, F. Vaccari, and C. Williams (2011). "Global patterns of land-atmosphere fluxes of carbon dioxide, latent heat, and sensible heat derived from eddy covariance, satellite, and meteorological observations." *Journal of Geophysical Research: Biogeosciences* 116.G3. DOI: https://doi.org/10.1029/2010JG001566.

Jung, M., M. Reichstein, C. R. Schwalm, C. Huntingford, S. Sitch, A. Ahlström, A. Arneth, G. Camps-Valls, P. Ciais, P. Friedlingstein, F. Gans, K. Ichii, A. K. Jain, E. Kato, D. Papale, B. Poulter, B. Raduly, C. Rödenbeck, G. Tramontana, N. Viovy, Y.-P. Wang, U. Weber, S. Zaehle, and N. Zeng (2017). "Compensatory water effects link yearly global land CO2 sink changes to temperature." *Nature* 541.7638, pp. 516–520. DOI: 10.1038/nature20780.

Jungclaus, J. H., S. J. Lorenz, H. Schmidt, V. Brovkin, N. Brüggemann, F. Chegini, T. Crüger, P. De-Vrese, V. Gayler, M. A. Giorgetta, O. Gutjahr, H. Haak, S. Hagemann, M. Hanke, T. Ilyina, P. Korn, J. Kröger, L. Linardakis, C. Mehlmann, U. Mikolajewicz, W. A. Müller, J. E. M. S. Nabel, D. Notz, H. Pohlmann, D. A. Putrasahan, T. Raddatz, L. Ramme, R. Redler, C. H. Reick, T. Riddick, T. Sam, R. Schneck, R. Schnur, M. Schupfner, J.-S. v. Storch, F. Wachsmann, K.-H. Wieners, F. Ziemen, B. Stevens, J. Marotzke, and M. Claussen (2022). "The ICON Earth System Model Version 1.0." *Journal of Advances in Modeling Earth Systems* 14.4, e2021MS002813. DOI: https://doi.org/10.1029/2021MS002813.

Kaisermann, A., F. T. d. Vries, R. I. Griffiths, and R. D. Bardgett (2017). "Legacy effects of drought on plant–soil feedbacks and plant–plant interactions." *New Phytologist* 215.4, pp. 1413–1424. DOI: https://doi.org/10.1111/nph.14661.

Kataoka, T., H. Tatebe, H. Koyama, T. Mochizuki, K. Ogochi, H. Naoe, Y. Imada, H. Shiogama, M. Kimoto, and M. Watan-

abe (2020). "Seasonal to Decadal Predictions With MIROC6: Description and Basic Evaluation." *Journal of Advances in Modeling Earth Systems* 12.12, e2019MS002035. DOI: https://doi.org/10.1029/2019MS002035.

Kay, J. E., C. Deser, A. Phillips, A. Mai, C. Hannay, G. Strand, J. M. Arblaster, S. C. Bates, G. Danabasoglu, J. Edwards, M. Holland, P. Kushner, J.-F. Lamarque, D. Lawrence, K. Lindsay, A. Middleton, E. Munoz, R. Neale, K. Oleson, L. Polvani, and M. Vertenstein (2015). "The Community Earth System Model (CESM) Large Ensemble Project: A Community Resource for Studying Climate Change in the Presence of Internal Climate Variability." *Bulletin of the American Meteorological Society* 96.8, pp. 1333–1349. DOI: 10.1175/BAMS-D-13-00255.1.

Knapp, A. K. and M. D. Smith (2001). "Variation Among Biomes in Temporal Dynamics of Aboveground Primary Production." *Science*. DOI: 10.1126/science.291.5503.481.

Kobayashi, S., Y. Ota, Y. Harada, A. Ebita, M. Moriya, H. Onoda, K. Onogi, H. Kamahori, C. Kobayashi, H. Endo, K. Miyaoka, and K. Takahashi (2015). "The JRA-55 Reanalysis: General Specifications and Basic Characteristics." *Journal of the Meteorological Society of Japan. Ser. II* 93.1, pp. 5–48. DOI: 10.2151/jmsj.2015-001.

Koster, R. D., S. P. P. Mahanama, T. J. Yamada, G. Balsamo, A. A. Berg, M. Boisserie, P. A. Dirmeyer, F. J. Doblas-Reyes, G. Drewitt, C. T. Gordon, Z. Guo, J.-H. Jeong, W.-S. Lee, Z. Li, L. Luo, S. Malyshev, W. J. Merryfield, S. I. Seneviratne, T. Stanelle, B. J. J. M. van den Hurk, F. Vitart, and E. F. Wood (2011). "The Second Phase of the Global Land–Atmosphere Coupling Experiment: Soil Moisture Contributions to Subseasonal Forecast Skill." *Journal of Hydrometeorology* 12.5, pp. 805–822. DOI: 10.1175/2011JHM1365.1.

Krull, E. S., J. A. Baldock, and J. O. Skjemstad (2003). "Importance of mechanisms and processes of the stabilisation of soil organic matter for modelling carbon turnover." *Functional Plant Biology* 30.2, pp. 207–222. DOI: 10.1071/fp02085.

Kumar, A., P. Peng, and M. Chen (2014). "Is There a Relationship between Potential and Actual Skill?" *Monthly Weather Review* 142.6, pp. 2220–2227. DOI: 10.1175/MWR-D-13-00287.1.

Kumar, S., M. Newman, D. M. Lawrence, M.-H. Lo, S. Akula, C.-W. Lan, B. Livneh, and D. Lombardozzi (2020). "The GLACE-Hydrology Experiment: Effects of Land–Atmosphere Coupling on Soil Moisture Variability and Predictability." *Journal*

of Climate 33.15, pp. 6511–6529. DOI: 10.1175/JCLI-D-19-0598.1.

Lawrence, D. M., R. A. Fisher, C. D. Koven, K. W. Oleson, S. C. Swenson, G. Bonan, N. Collier, B. Ghimire, L. v. Kampenhout, D. Kennedy, E. Kluzek, P. J. Lawrence, F. Li, H. Li, D. Lombardozzi, W. J. Riley, W. J. Sacks, M. Shi, M. Vertenstein, W. R. Wieder, C. Xu, A. A. Ali, A. M. Badger, G. Bisht, M. v. d. Broeke, M. A. Brunke, S. P. Burns, J. Buzan, M. Clark, A. Craig, K. Dahlin, B. Drewniak, J. B. Fisher, M. Flanner, A. M. Fox, P. Gentine, F. Hoffman, G. Keppel-Aleks, R. Knox, S. Kumar, J. Lenaerts, L. R. Leung, W. H. Lipscomb, Y. Lu, A. Pandey, J. D. Pelletier, J. Perket, J. T. Randerson, D. M. Ricciuto, B. M. Sanderson, A. Slater, Z. M. Subin, J. Tang, R. Q. Thomas, M. V. Martin, and X. Zeng (2019). "The Community Land Model Version 5: Description of New Features, Benchmarking, and Impact of Forcing Uncertainty." *Journal of Advances in Modeling Earth Systems* 11.12, pp. 4245–4287. DOI: https://doi.org/10.1029/2018MS001583.

Lawrence, D. M., K. W. Oleson, M. G. Flanner, P. E. Thornton, S. C. Swenson, P. J. Lawrence, X. Zeng, Z.-L. Yang, S. Levis, K. Sakaguchi, G. B. Bonan, and A. G. Slater (2011). "Parameterization improvements and functional and structural advances in Version 4 of the Community Land Model." *Journal of Advances in Modeling Earth Systems* 3.1. DOI: https://doi.org/10.1029/2011MS00045.

Le Page, Y., J. M. C. Pereira, R. Trigo, C. da Camara, D. Oom, and B. Mota (2008). "Global fire activity patterns (1996–2006) and climatic influence: an analysis using the World Fire Atlas." *Atmospheric Chemistry and Physics* 8.7, pp. 1911–1924. DOI: 10.5194/acp-8-1911-2008.

Lee, E., F.-W. Zeng, R. D. Koster, B. Weir, L. E. Ott, and B. Poulter (2018). "The impact of spatiotemporal variability in atmospheric CO_2 concentration on global terrestrial carbon fluxes." *Biogeosciences* 15.18, pp. 5635–5652. DOI: 10.5194/bg-15-5635-2018.

Li, H., T. Ilyina, T. Loughran, A. Spring, and J. Pongratz (2022). "Reconstructions and predictions of the global carbon budget with an emission-driven Earth System Model." *Earth System Dynamics Discussions*, pp. 1–26. DOI: 10.5194/esd-2022-37.

Liu, J., K. W. Bowman, D. S. Schimel, N. C. Parazoo, Z. Jiang, M. Lee, A. A. Bloom, D. Wunch, C. Frankenberg, Y. Sun, C. W. O'Dell, K. R. Gurney, D. Menemenlis, M. Gierach, D. Crisp, and A. Eldering (2017). "Contrasting carbon cycle responses

of the tropical continents to the 2015–2016 El Niño." *Science*. DOI: 10.1126/science.aam5690.

Lovato, T., D. Peano, M. Butenschön, S. Materia, D. Iovino, E. Scoccimarro, P. G. Fogli, A. Cherchi, A. Bellucci, S. Gualdi, S. Masina, and A. Navarra (2022). "CMIP6 Simulations With the CMCC Earth System Model (CMCC-ESM2)." *Journal of Advances in Modeling Earth Systems* 14.3, e2021MS002814. DOI: https://doi.org/10.1029/2021MS002814.

Lovenduski, N. S., G. B. Bonan, S. G. Yeager, K. Lindsay, and D. L. Lombardozzi (2019). "High predictability of terrestrial carbon fluxes from an initialized decadal prediction system." *Environmental Research Letters* 14.12, p. 124074. DOI: 10.1088/1748-9326/ab5c55.

Lozano, Y. M., C. A. Aguilar-Trigueros, J. M. Ospina, and M. C. Rillig (2022). "Drought legacy effects on root morphological traits and plant biomass via soil biota feedback." *New Phytologist*. DOI: https://doi.org/10.1111/nph.18327.

Luo, Y., A. Ahlström, S. D. Allison, N. H. Batjes, V. Brovkin, N. Carvalhais, A. Chappell, P. Ciais, E. A. Davidson, A. Finzi, K. Georgiou, B. Guenet, O. Hararuk, J. W. Harden, Y. He, F. Hopkins, L. Jiang, C. Koven, R. B. Jackson, C. D. Jones, M. J. Lara, J. Liang, A. D. McGuire, W. Parton, C. Peng, J. T. Randerson, A. Salazar, C. A. Sierra, M. J. Smith, H. Tian, K. E. O. Todd-Brown, M. Torn, K. J. v. Groenigen, Y. P. Wang, T. O. West, Y. Wei, W. R. Wieder, J. Xia, X. Xu, X. Xu, and T. Zhou (2016). "Toward more realistic projections of soil carbon dynamics by Earth system models." *Global Biogeochemical Cycles* 30.1, pp. 40–56. DOI: https://doi.org/10.1002/2015GB005239.

Luo, Y., T. F. Keenan, and M. Smith (2015). "Predictability of the terrestrial carbon cycle." *Global Change Biology* 21.5, pp. 1737–1751. DOI: https://doi.org/10.1111/gcb.12766.

Magnusson, L., M. Alonso-Balmaseda, S. Corti, F. Molteni, and T. Stockdale (2013). "Evaluation of forecast strategies for seasonal and decadal forecasts in presence of systematic model errors." *Climate Dynamics* 41.9, pp. 2393–2409. DOI: 10.1007/s00382-012-1599-2.

Manzanas, R., M. D. Frías, A. S. Cofiño, and J. M. Gutiérrez (2014). "Validation of 40 year multimodel seasonal precipitation forecasts: The role of ENSO on the global skill." *Journal of Geophysical Research: Atmospheres* 119.4, pp. 1708–1719. DOI: https://doi.org/10.1002/2013JD020680.

Marotzke, J., W. A. Müller, F. S. E. Vamborg, P. Becker, U. Cubasch, H. Feldmann, F. Kaspar, C. Kottmeier, C. Marini,

I. Polkova, K. Prömmel, H. W. Rust, D. Stammer, U. Ulbrich, C. Kadow, A. Köhl, J. Kröger, T. Kruschke, J. G. Pinto, H. Pohlmann, M. Reyers, M. Schröder, F. Sienz, C. Timmreck, and M. Ziese (2016). "MiKlip: A National Research Project on Decadal Climate Prediction." *Bulletin of the American Meteorological Society* 97.12, pp. 2379–2394. DOI: 10.1175/BAMS-D-15-00184.1.

Mauritsen, T., J. Bader, T. Becker, J. Behrens, M. Bittner, R. Brokopf, V. Brovkin, M. Claussen, T. Crueger, M. Esch, I. Fast, S. Fiedler, D. Fläschner, V. Gayler, M. Giorgetta, D. S. Goll, H. Haak, S. Hagemann, C. Hedemann, C. Hohenegger, T. Ilyina, T. Jahns, D. Jimenéz-de-la-Cuesta, J. Jungclaus, T. Kleinen, S. Kloster, D. Kracher, S. Kinne, D. Kleberg, G. Lasslop, L. Kornblueh, J. Marotzke, D. Matei, K. Meraner, U. Mikolajewicz, K. Modali, B. Möbis, W. A. Müller, J. E. M. S. Nabel, C. C. W. Nam, D. Notz, S.-S. Nyawira, H. Paulsen, K. Peters, R. Pincus, H. Pohlmann, J. Pongratz, M. Popp, T. J. Raddatz, S. Rast, R. Redler, C. H. Reick, T. Rohrschneider, V. Schemann, H. Schmidt, R. Schnur, U. Schulzweida, K. D. Six, L. Stein, I. Stemmler, B. Stevens, J.-S. v. Storch, F. Tian, A. Voigt, P. Vrese, K.-H. Wieners, S. Wilkenskjeld, A. Winkler, and E. Roeckner (2019). "Developments in the MPI-M Earth System Model version 1.2 (MPI-ESM1.2) and Its Response to Increasing CO2." *Journal of Advances in Modeling Earth Systems* 11.4, pp. 998–1038. DOI: 10.1029/2018MS001400.

McKinley, G. A., A. R. Fay, N. S. Lovenduski, and D. J. Pilcher (2017). "Natural Variability and Anthropogenic Trends in the Ocean Carbon Sink." *Annual Review of Marine Science* 9.1, pp. 125–150. DOI: 10.1146/annurev-marine-010816-060529.

Meehl, G. A., J. H. Richter, H. Teng, A. Capotondi, K. Cobb, F. Doblas-Reyes, M. G. Donat, M. H. England, J. C. Fyfe, W. Han, H. Kim, B. P. Kirtman, Y. Kushnir, N. S. Lovenduski, M. E. Mann, W. J. Merryfield, V. Nieves, K. Pegion, N. Rosenbloom, S. C. Sanchez, A. A. Scaife, D. Smith, A. C. Subramanian, L. Sun, D. Thompson, C. C. Ummenhofer, and S.-P. Xie (2021). "Initialized Earth System prediction from subseasonal to decadal timescales." *Nature Reviews Earth & Environment* 2.5, pp. 340–357. DOI: 10.1038/s43017-021-00155-x.

Meir, P, D. Metcalfe, A. Costa, and R. Fisher (2008). "The fate of assimilated carbon during drought: impacts on respiration in Amazon rainforests." *Philosophical Transactions of the Royal Society B: Biological Sciences* 363.1498, pp. 1849–1855. DOI: 10.1098/rstb.2007.0021.

Merryfield, W. J., J. Baehr, L. Batté, E. J. Becker, A. H. Butler, C. A. S. Coelho, G. Danabasoglu, P. A. Dirmeyer, F. J. Doblas-Reyes, D. I. V. Domeisen, L. Ferranti, T. Ilynia, A. Kumar, W. A. Müller, M. Rixen, A. W. Robertson, D. M. Smith, Y. Takaya, M. Tuma, F. Vitart, C. J. White, M. S. Alvarez, C. Ardilouze, H. Attard, C. Baggett, M. A. Balmaseda, A. F. Beraki, P. S. Bhattacharjee, R. Bilbao, F. M. d. Andrade, M. J. DeFlorio, L. B. Díaz, M. A. Ehsan, G. Fragkoulidis, S. Grainger, B. W. Green, M. C. Hell, J. M. Infanti, K. Isensee, T. Kataoka, B. P. Kirtman, N. P. Klingaman, J.-Y. Lee, K. Mayer, R. McKay, J. V. Mecking, D. E. Miller, N. Neddermann, C. H. J. Ng, A. Ossó, K. Pankatz, S. Peatman, K. Pegion, J. Perlwitz, G. C. Recalde-Coronel, A. Reintges, C. Renkl, B. Solaraju-Murali, A. Spring, C. Stan, Y. Q. Sun, C. R. Tozer, N. Vigaud, S. Woolnough, and S. Yeager (2020). "Current and Emerging Developments in Subseasonal to Decadal Prediction." *Bulletin of the American Meteorological Society* 101.6, E869–E896. DOI: 10.1175/BAMS-D-19-0037.1.

Muggeo, V. (2008). "Segmented: An R Package to Fit Regression Models With Broken-Line Relationships." *R News* 8, pp. 20–25.

Mullen, K. M. and I. H. M. van Stokkum (2012). *The Lawson-Hanson algorithm for non-negative least squares (NNLS)*. https://cran.r-project.org/web/packages/nnls/index.html.

Mystakidis, S., E. L. Davin, N. Gruber, and S. I. Seneviratne (2016). "Constraining future terrestrial carbon cycle projections using observation-based water and carbon flux estimates." *Global Change Biology* 22.6, pp. 2198–2215. DOI: 10.1111/gcb.13217.

Müller, W. A., J. H. Jungclaus, T. Mauritsen, J. Baehr, M. Bittner, R. Budich, F. Bunzel, M. Esch, R. Ghosh, H. Haak, T. Ilyina, T. Kleine, L. Kornblueh, H. Li, K. Modali, D. Notz, H. Pohlmann, E. Roeckner, I. Stemmler, F. Tian, and J. Marotzke (2018). "A Higher-resolution Version of the Max Planck Institute Earth System Model (MPI-ESM1.2-HR)." *Journal of Advances in Modeling Earth Systems* 10.7, pp. 1383–1413. DOI: https://doi.org/10.1029/2017MS001217.

Niu, S., Z. Fu, Y. Luo, P. C. Stoy, T. F. Keenan, B. Poulter, L. Zhang, S. Piao, X. Zhou, H. Zheng, J. Han, Q. Wang, and G. Yu (2017). "Interannual variability of ecosystem carbon exchange: From observation to prediction." *Global Ecology and Biogeography* 26.11, pp. 1225–1237. DOI: https://doi.org/10.1111/geb.12633.

O'Sullivan, M., W. K. Smith, S. Sitch, P. Friedlingstein, V. K. Arora, V. Haverd, A. K. Jain, E. Kato, M. Kautz, D. Lombar-

dozzi, J. E. M. S. Nabel, H. Tian, N. Vuichard, A. Wiltshire, D. Zhu, and W. Buermann (2020). "Climate-Driven Variability and Trends in Plant Productivity Over Recent Decades Based on Three Global Products." *Global Biogeochemical Cycles* 34.12, e2020GB006613. DOI: https://doi.org/10.1029/2020GB006613.

Orbe, C., D. Rind, J. Jonas, L. Nazarenko, G. Faluvegi, L. T. Murray, D. T. Shindell, K. Tsigaridis, T. Zhou, M. Kelley, and G. A. Schmidt (2020). "GISS Model E2.2: A Climate Model Optimized for the Middle Atmosphere—2. Validation of Large-Scale Transport and Evaluation of Climate Response." *Journal of Geophysical Research: Atmospheres* 125.24, e2020JD033151. DOI: https://doi.org/10.1029/2020JD033151.

Padrón, R. S., L. Gudmundsson, L. Liu, V. Humphrey, and S. I. Seneviratne (2022). "Controls of intermodel uncertainty in land carbon sink projections." *Biogeosciences Discussions*, pp. 1–20. DOI: 10.5194/bg-2022-92.

Paris Agreement (2015). *United Nations Treaty Collection, Chapter XXVII 7. d*.

Peano, D., S. Materia, A. Collalti, A. Alessandri, A. Anav, A. Bombelli, and S. Gualdi (2019). "Global Variability of Simulated and Observed Vegetation Growing Season." *Journal of Geophysical Research: Biogeosciences* 124.11, pp. 3569–3587. DOI: https://doi.org/10.1029/2018JG004881.

Peano, D., D. Hemming, S. Materia, C. Delire, Y. Fan, E. Joetzjer, H. Lee, J. E. M. S. Nabel, T. Park, P. Peylin, D. Wårlind, A. Wiltshire, and S. Zaehle (2021). "Plant phenology evaluation of CRESCENDO land surface models – Part 1: Start and end of the growing season." *Biogeosciences* 18.7, pp. 2405–2428. DOI: 10.5194/bg-18-2405-2021.

Peters, G. P., C. Le Quéré, R. M. Andrew, J. G. Canadell, P. Friedlingstein, T. Ilyina, R. B. Jackson, F. Joos, J. I. Korsbakken, G. A. McKinley, S. Sitch, and P. Tans (2017). "Towards real-time verification of CO2 emissions." *Nature Climate Change* 7.12, pp. 848–850. DOI: 10.1038/s41558-017-0013-9.

Piao, S., S. Luyssaert, P. Ciais, I. A. Janssens, A. Chen, C. Cao, J. Fang, P. Friedlingstein, Y. Luo, and S. Wang (2010). "Forest annual carbon cost: a global-scale analysis of autotrophic respiration." *Ecology* 91.3, pp. 652–661. DOI: https://doi.org/10.1890/08-2176.1.

Piao, S., S. Sitch, P. Ciais, P. Friedlingstein, P. Peylin, X. Wang, A. Ahlström, A. Anav, J. G. Canadell, N. Cong, C. Huntingford, M. Jung, S. Levis, P. E. Levy, J. Li, X. Lin, M. R. Lomas, M. Lu,

Y. Luo, Y. Ma, R. B. Myneni, B. Poulter, Z. Sun, T. Wang, N. Viovy, S. Zaehle, and N. Zeng (2013). "Evaluation of terrestrial carbon cycle models for their response to climate variability and to CO2 trends." *Global Change Biology* 19.7, pp. 2117–2132. DOI: https://doi.org/10.1111/gcb.12187.

Piao, S., X. Wang, K. Wang, X. Li, A. Bastos, J. G. Canadell, P. Ciais, P. Friedlingstein, and S. Sitch (2020). "Interannual variation of terrestrial carbon cycle: Issues and perspectives." *Global Change Biology* 26.1, pp. 300–318. DOI: https://doi.org/10.1111/gcb.14884.

Poulter, B., D. Frank, P. Ciais, R. B. Myneni, N. Andela, J. Bi, G. Broquet, J. G. Canadell, F. Chevallier, Y. Y. Liu, S. W. Running, S. Sitch, and G. R. van der Werf (2014). "Contribution of semi-arid ecosystems to interannual variability of the global carbon cycle." *Nature* 509.7502, pp. 600–603. DOI: 10.1038/nature13376.

Qian, H., R. Joseph, and N. Zeng (2008). "Response of the terrestrial carbon cycle to the El Niño-Southern Oscillation." *Tellus B: Chemical and Physical Meteorology* 60.4, pp. 537–550. DOI: 10.1111/j.1600-0889.2008.00360.x.

Qiao, L., Z. Zuo, and D. Xiao (2022). "Evaluation of Soil Moisture in CMIP6 Simulations." *Journal of Climate* 35.2, pp. 779–800. DOI: 10.1175/JCLI-D-20-0827.1.

Quesada, B., R. Vautard, P. Yiou, M. Hirschi, and S. I. Seneviratne (2012). "Asymmetric European summer heat predictability from wet and dry southern winters and springs." *Nature Climate Change* 2.10, pp. 736–741. DOI: 10.1038/nclimate1536.

Rayner, N. A., D. E. Parker, E. B. Horton, C. K. Folland, L. V. Alexander, D. P. Rowell, E. C. Kent, and A. Kaplan (2003). "Global analyses of sea surface temperature, sea ice, and night marine air temperature since the late nineteenth century." *Journal of Geophysical Research: Atmospheres* 108.D14. DOI: https://doi.org/10.1029/2002JD002670.

Reichstein, M., A. Rey, A. Freibauer, J. Tenhunen, R. Valentini, J. Banza, P. Casals, Y. Cheng, J. M. Grünzweig, J. Irvine, R. Joffre, B. E. Law, D. Loustau, F. Miglietta, W. Oechel, J.-M. Ourcival, J. S. Pereira, A. Peressotti, F. Ponti, Y. Qi, S. Rambal, M. Rayment, J. Romanya, F. Rossi, V. Tedeschi, G. Tirone, M. Xu, and D. Yakir (2003). "Modeling temporal and large-scale spatial variability of soil respiration from soil water availability, temperature and vegetation productivity indices." *Global Biogeochemical Cycles* 17.4. DOI: https://doi.org/10.1029/2003GB002035.

Reick, C. H., T. Raddatz, V. Brovkin, and V. Gayler (2013). "Representation of natural and anthropogenic land cover change in MPI-ESM." *Journal of Advances in Modeling Earth Systems* 5.3, pp. 459–482. DOI: https://doi.org/10.1002/jame.20022.

Running, S., M. Qiaozhen, and M. Zhao (2019). "MOD17A2H MODIS/Terra Gross Primary Productivity 8-Day L4 Global 500m SIN Grid V006. NASA EOSDIS Land Processes DAAC." DOI: doi.org/10.5067/MODIS/MOD17A2H.006.

Santanello, J. A., P. A. Dirmeyer, C. R. Ferguson, K. L. Findell, A. B. Tawfik, A. Berg, M. Ek, P. Gentine, B. P. Guillod, C. v. Heerwaarden, J. Roundy, and V. Wulfmeyer (2018). "Land–Atmosphere Interactions: The LoCo Perspective." *Bulletin of the American Meteorological Society* 99.6, pp. 1253–1272. DOI: 10.1175/BAMS-D-17-0001.1.

Santos, V. A. H. F. d., M. J. Ferreira, J. V. F. C. Rodrigues, M. N. Garcia, J. V. B. Ceron, B. W. Nelson, and S. R. Saleska (2018). "Causes of reduced leaf-level photosynthesis during strong El Niño drought in a Central Amazon forest." *Global Change Biology* 24.9, pp. 4266–4279. DOI: https://doi.org/10.1111/gcb.14293.

Scaife, A. A., A. Arribas, E. Blockley, A. Brookshaw, R. T. Clark, N. Dunstone, R. Eade, D. Fereday, C. K. Folland, M. Gordon, L. Hermanson, J. R. Knight, D. J. Lea, C. MacLachlan, A. Maidens, M. Martin, A. K. Peterson, D. Smith, M. Vellinga, E. Wallace, J. Waters, and A. Williams (2014). "Skillful long-range prediction of European and North American winters." *Geophysical Research Letters* 41.7, pp. 2514–2519. DOI: https://doi.org/10.1002/2014GL059637.

Schaefer, K., A. S. Denning, N. Suits, J. Kaduk, I. Baker, S. Los, and L. Prihodko (2002). "Effect of climate on interannual variability of terrestrial CO2 fluxes." *Global Biogeochemical Cycles* 16.4, pp. 49–1–49–12. DOI: 10.1029/2002GB001928.

Schömann, E.-M., S. N. Vardag, S. Basu, M. Jung, B. Ahrens, T. El-Madany, S. Sitch, V. K. Arora, P. R. Briggs, P. Friedlingstein, D. S. Goll, A. K. Jain, E. Kato, D. Lombardozzi, J. E. M. S. Nabel, B. Poulter, R. Séférian, H. Tian, A. Wiltshire, W. Yuan, X. Yue, S. Zaehle, N. M. Deutscher, D. W. T. Griffith, and A. Butz (2022). "Respiration driven CO2 pulses dominate Australia's flux variability." *arXiv:2207.06869 [physics]*.

Seland, M. Bentsen, D. Olivié, T. Toniazzo, A. Gjermundsen, L. S. Graff, J. B. Debernard, A. K. Gupta, Y.-C. He, A. Kirkevåg, J. Schwinger, J. Tjiputra, K. S. Aas, I. Bethke, Y. Fan, J. Griesfeller, A. Grini, C. Guo, M. Ilicak, I. H. H. Karset, O. Landgren,

J. Liakka, K. O. Moseid, A. Nummelin, C. Spensberger, H. Tang, Z. Zhang, C. Heinze, T. Iversen, and M. Schulz (2020). "Overview of the Norwegian Earth System Model (NorESM2) and key climate response of CMIP6 DECK, historical, and scenario simulations." *Geoscientific Model Development* 13.12, pp. 6165–6200. DOI: 10.5194/gmd-13-6165-2020.

Sellar, A. A., C. G. Jones, J. P. Mulcahy, Y. Tang, A. Yool, A. Wiltshire, F. M. O'Connor, M. Stringer, R. Hill, J. Palmieri, S. Woodward, L. d. Mora, T. Kuhlbrodt, S. T. Rumbold, D. I. Kelley, R. Ellis, C. E. Johnson, J. Walton, N. L. Abraham, M. B. Andrews, T. Andrews, A. T. Archibald, S. Berthou, E. Burke, E. Blockley, K. Carslaw, M. Dalvi, J. Edwards, G. A. Folberth, N. Gedney, P. T. Griffiths, A. B. Harper, M. A. Hendry, A. J. Hewitt, B. Johnson, A. Jones, C. D. Jones, J. Keeble, S. Liddicoat, O. Morgenstern, R. J. Parker, V. Predoi, E. Robertson, A. Siahaan, R. S. Smith, R. Swaminathan, M. T. Woodhouse, G. Zeng, and M. Zerroukat (2019). "UKESM1: Description and Evaluation of the U.K. Earth System Model." *Journal of Advances in Modeling Earth Systems* 11.12, pp. 4513–4558. DOI: https://doi.org/10.1029/2019MS001739.

Seo, E., M.-I. Lee, J.-H. Jeong, R. D. Koster, S. D. Schubert, H.-M. Kim, D. Kim, H.-S. Kang, H.-K. Kim, C. MacLachlan, and A. A. Scaife (2019). "Impact of soil moisture initialization on boreal summer subseasonal forecasts: mid-latitude surface air temperature and heat wave events." *Climate Dynamics* 52.3, pp. 1695–1709. DOI: 10.1007/s00382-018-4221-4.

Shi, X., G. Lohmann, D. Sidorenko, and H. Yang (2020). "Early-Holocene simulations using different forcings and resolutions in AWI-ESM." *The Holocene* 30.7, pp. 996–1015. DOI: 10.1177/0959683620908634.

Silva, C. V. J., L. E. O. C. Aragão, J. Barlow, F. Espirito-Santo, P. J. Young, L. O. Anderson, E. Berenguer, I. Brasil, I. Foster Brown, B. Castro, R. Farias, J. Ferreira, F. França, P. M. L. A. Graça, L. Kirsten, A. P. Lopes, C. Salimon, M. A. Scaranello, M. Seixas, F. C. Souza, and H. A. M. Xaud (2018). "Drought-induced Amazonian wildfires instigate a decadal-scale disruption of forest carbon dynamics." *Philosophical Transactions of the Royal Society B: Biological Sciences* 373.1760, p. 20180043. DOI: 10.1098/rstb.2018.0043.

Sitch, S., P. Friedlingstein, N. Gruber, S. D. Jones, G. Murray-Tortarolo, A. Ahlström, S. C. Doney, H. Graven, C. Heinze, C. Huntingford, S. Levis, P. E. Levy, M. Lomas, B. Poulter, N. Viovy, S. Zaehle, N. Zeng, A. Arneth, G. Bonan, L. Bopp, J. G.

Canadell, F. Chevallier, P. Ciais, R. Ellis, M. Gloor, P. Peylin, S. L. Piao, C. Le Quéré, B. Smith, Z. Zhu, and R. Myneni (2015). "Recent trends and drivers of regional sources and sinks of carbon dioxide." *Biogeosciences* 12.3, pp. 653–679. DOI: 10.5194/bg-12-653-2015.

Smith, D. M., A. A. Scaife, and B. P. Kirtman (2012). "What is the current state of scientific knowledge with regard to seasonal and decadal forecasting?" *Environmental Research Letters* 7.1, p. 015602. DOI: 10.1088/1748-9326/7/1/015602.

Smith, T. M., R. W. Reynolds, T. C. Peterson, and J. Lawrimore (2008). "Improvements to NOAA's Historical Merged Land–Ocean Surface Temperature Analysis (1880–2006)." *Journal of Climate* 21.10, pp. 2283–2296. DOI: 10.1175/2007JCLI2100.1.

Song, X., D.-Y. Wang, F. Li, and X.-D. Zeng (2021). "Evaluating the performance of CMIP6 Earth system models in simulating global vegetation structure and distribution." *Advances in Climate Change Research*. Special Issue on Arctic Rapid Change 12.4, pp. 584–595. DOI: 10.1016/j.accre.2021.06.008.

Spring, A., I. Dunkl, H. Li, V. Brovkin, and T. Ilyina (2021). "Trivial improvements in predictive skill due to direct reconstruction of the global carbon cycle." *Earth System Dynamics* 12.4, pp. 1139–1167. DOI: 10.5194/esd-12-1139-2021.

Spring, A. and T. Ilyina (2020). "Predictability Horizons in the Global Carbon Cycle Inferred From a Perfect-Model Framework." *Geophysical Research Letters* 47.9, e2019GL085311. DOI: https://doi.org/10.1029/2019GL085311.

Spring, A., T. Ilyina, and J. Marotzke (2020). "Inherent uncertainty disguises attribution of reduced atmospheric CO2 growth to CO2 emission reductions for up to a decade." *Environ. Res. Lett.* 15.11, p. 114058. DOI: 10.1088/1748-9326/abc443.

Stockmann, U., M. A. Adams, J. W. Crawford, D. J. Field, N. Henakaarchchi, M. Jenkins, B. Minasny, A. B. McBratney, V. d. R. d. Courcelles, K. Singh, I. Wheeler, L. Abbott, D. A. Angers, J. Baldock, M. Bird, P. C. Brookes, C. Chenu, J. D. Jastrow, R. Lal, J. Lehmann, A. G. O'Donnell, W. J. Parton, D. Whitehead, and M. Zimmermann (2013). "The knowns, known unknowns and unknowns of sequestration of soil organic carbon." *Agriculture, Ecosystems & Environment* 164, pp. 80–99. DOI: 10.1016/j.agee.2012.10.001.

Swart, N. C., J. N. S. Cole, V. V. Kharin, M. Lazare, J. F. Scinocca, N. P. Gillett, J. Anstey, V. Arora, J. R. Christian, S. Hanna, Y. Jiao, W. G. Lee, F. Majaess, O. A. Saenko, C. Seiler, C. Seinen,

A. Shao, M. Sigmond, L. Solheim, K. von Salzen, D. Yang, and B. Winter (2019). "The Canadian Earth System Model version 5 (CanESM5.0.3)." *Geoscientific Model Development* 12.11, pp. 4823–4873. DOI: 10.5194/gmd-12-4823-2019.

Séférian, R., S. Berthet, and M. Chevallier (2018). "Assessing the Decadal Predictability of Land and Ocean Carbon Uptake." *Geophysical Research Letters* 45.5, pp. 2455–2466. DOI: https://doi.org/10.1002/2017GL076092.

Séférian, R., P. Nabat, M. Michou, D. Saint-Martin, A. Voldoire, J. Colin, B. Decharme, C. Delire, S. Berthet, M. Chevallier, S. Sénési, L. Franchisteguy, J. Vial, M. Mallet, E. Joetzjer, O. Geoffroy, J.-F. Guérémy, M.-P. Moine, R. Msadek, A. Ribes, M. Rocher, R. Roehrig, D. Salas-y Mélia, E. Sanchez, L. Terray, S. Valcke, R. Waldman, O. Aumont, L. Bopp, J. Deshayes, C. Éthé, and G. Madec (2019). "Evaluation of CNRM Earth System Model, CNRM-ESM2-1: Role of Earth System Processes in Present-Day and Future Climate." *Journal of Advances in Modeling Earth Systems* 11.12, pp. 4182–4227. DOI: https://doi.org/10.1029/2019MS001791.

Tedeschi, R. G. and M. Collins (2016). "The influence of ENSO on South American precipitation during austral summer and autumn in observations and models." *International Journal of Climatology* 36.2, pp. 618–635. DOI: https://doi.org/10.1002/joc.4371.

Tews, J., A. Esther, S. J. Milton, and F. Jeltsch (2006). "Linking a population model with an ecosystem model: Assessing the impact of land use and climate change on savanna shrub cover dynamics." *Ecological Modelling* 195.3, pp. 219–228. DOI: 10.1016/j.ecolmodel.2005.11.025.

Tian, H., J. M. Melillo, D. W. Kicklighter, A. D. McGuire, J. H. Iii, B. M. Iii, and C. J. Vörösmarty (2000). "Climatic and biotic controls on annual carbon storage in Amazonian ecosystems." *Global Ecology and Biogeography* 9.4, pp. 315–335. DOI: 10.1046/j.1365-2699.2000.00198.x.

Tian, H., J. M. Melillo, D. W. Kicklighter, A. D. McGuire, J. V. K. Helfrich, B. Moore, and C. J. Vörösmarty (1998). "Effect of interannual climate variability on carbon storage in Amazonian ecosystems." *Nature* 396.6712, pp. 664–667. DOI: 10.1038/25328.

Titchner, H. A. and N. A. Rayner (2014). "The Met Office Hadley Centre sea ice and sea surface temperature data set, version 2: 1. Sea ice concentrations." *Journal of Geophysical Research:*

Atmospheres 119.6, pp. 2864–2889. DOI: https://doi.org/10.1002/2013JD020316.

Tsujino, H., S. Urakawa, H. Nakano, R. J. Small, W. M. Kim, S. G. Yeager, G. Danabasoglu, T. Suzuki, J. L. Bamber, M. Bentsen, C. W. Böning, A. Bozec, E. P. Chassignet, E. Curchitser, F. Boeira Dias, P. J. Durack, S. M. Griffies, Y. Harada, M. Ilicak, S. A. Josey, C. Kobayashi, S. Kobayashi, Y. Komuro, W. G. Large, J. Le Sommer, S. J. Marsland, S. Masina, M. Scheinert, H. Tomita, M. Valdivieso, and D. Yamazaki (2018). "JRA-55 based surface dataset for driving ocean–sea-ice models (JRA55-do)." *Ocean Modelling* 130, pp. 79–139. DOI: 10.1016/j.ocemod.2018.07.002.

Tuomi, M., T. Thum, H. Järvinen, S. Fronzek, B. Berg, M. Harmon, J. A. Trofymow, S. Sevanto, and J. Liski (2009). "Leaf litter decomposition—Estimates of global variability based on Yasso07 model." *Ecological Modelling* 220.23, pp. 3362–3371. DOI: 10.1016/j.ecolmodel.2009.05.016.

Tziolas, N., N. Tsakiridis, Y. Ogen, E. Kalopesa, E. Ben-Dor, J. Theocharis, and G. Zalidis (2020). "An integrated methodology using open soil spectral libraries and Earth Observation data for soil organic carbon estimations in support of soil-related SDGs." *Remote Sensing of Environment* 244, p. 111793. DOI: 10.1016/j.rse.2020.111793.

Uppala, S. M., P. W. KÅllberg, A. J. Simmons, U. Andrae, V. D. C. Bechtold, M. Fiorino, J. K. Gibson, J. Haseler, A. Hernandez, G. A. Kelly, X. Li, K. Onogi, S. Saarinen, N. Sokka, R. P. Allan, E. Andersson, K. Arpe, M. A. Balmaseda, A. C. M. Beljaars, L. V. D. Berg, J. Bidlot, N. Bormann, S. Caires, F. Chevallier, A. Dethof, M. Dragosavac, M. Fisher, M. Fuentes, S. Hagemann, E. Hólm, B. J. Hoskins, L. Isaksen, P. a. E. M. Janssen, R. Jenne, A. P. Mcnally, J.-F. Mahfouf, J.-J. Morcrette, N. A. Rayner, R. W. Saunders, P. Simon, A. Sterl, K. E. Trenberth, A. Untch, D. Vasiljevic, P. Viterbo, and J. Woollen (2005). "The ERA-40 re-analysis." *Quarterly Journal of the Royal Meteorological Society* 131.612, pp. 2961–3012. DOI: https://doi.org/10.1256/qj.04.176.

Van Oijen, M., A. Schapendonk, and M. Höglind (2010). "On the relative magnitudes of photosynthesis, respiration, growth and carbon storage in vegetation." *Annals of Botany* 105.5, pp. 793–797. DOI: 10.1093/aob/mcq039.

Walther, S., S. Besnard, J. A. Nelson, T. S. El-Madany, M. Migliavacca, U. Weber, N. Carvalhais, S. L. Ermida, C. Brümmer, F. Schrader, A. S. Prokushkin, A. V. Panov, and M. Jung (2022).

"Technical note: A view from space on global flux towers by MODIS and Landsat: the FluxnetEO data set." *Biogeosciences* 19.11, pp. 2805–2840. DOI: 10.5194/bg-19-2805-2022.

Wang, G., S. Sun, and R. Mei (2011). "Vegetation dynamics contributes to the multi-decadal variability of precipitation in the Amazon region." *Geophysical Research Letters* 38.19. DOI: 10.1029/2011GL049017.

Wang, J., N. Zeng, and M. Wang (2016). "Interannual variability of the atmospheric CO2 growth rate: roles of precipitation and temperature." *Biogeosciences* 13.8, pp. 2339–2352. DOI: 10.5194/bg-13-2339-2016.

Wang, Y., P. Zhao, R. Yu, and G. Rasul (2010). "Inter-decadal variability of Tibetan spring vegetation and its associations with eastern China spring rainfall." *International Journal of Climatology* 30.6, pp. 856–865. DOI: 10.1002/joc.1939.

Wei, W., C. Weile, and W. Shaopeng (2010). "Forest soil respiration and its heterotrophic and autotrophic components: Global patterns and responses to temperature and precipitation." *Soil Biology and Biochemistry* 42.8, pp. 1236–1244. DOI: 10.1016/j.soilbio.2010.04.013.

Weiss, M., B. van den Hurk, R. Haarsma, and W. Hazeleger (2012). "Impact of vegetation variability on potential predictability and skill of EC-Earth simulations." *Climate Dynamics* 39.11, pp. 2733–2746. DOI: 10.1007/s00382-012-1572-0.

Weiss, M., P. A. Miller, B. J. J. M. van den Hurk, T. van Noije, S. Ştefănescu, R. Haarsma, L. H. van Ulft, W. Hazeleger, P. Le Sager, B. Smith, and G. Schurgers (2014). "Contribution of Dynamic Vegetation Phenology to Decadal Climate Predictability." *Journal of Climate* 27.22, pp. 8563–8577. DOI: 10.1175/JCLI-D-13-00684.1.

Wieder, W. R., Z. Butterfield, K. Lindsay, D. L. Lombardozzi, and G. Keppel-Aleks (2021). "Interannual and Seasonal Drivers of Carbon Cycle Variability Represented by the Community Earth System Model (CESM2)." *Global Biogeochemical Cycles* 35.9, e2021GB007034. DOI: https://doi.org/10.1029/2021GB007034.

Wigneron, J.-P., L. Fan, P. Ciais, A. Bastos, M. Brandt, J. Chave, S. Saatchi, A. Baccini, and R. Fensholt (2020). "Tropical forests did not recover from the strong 2015–2016 El Niño event." *Science Advances*. DOI: 10.1126/sciadv.aay4603.

Winkler, A. J., R. B. Myneni, A. Hannart, S. Sitch, V. Haverd, D. Lombardozzi, V. K. Arora, J. Pongratz, J. E. M. S. Nabel, D. S.

Goll, E. Kato, H. Tian, A. Arneth, P. Friedlingstein, A. K. Jain, S. Zaehle, and V. Brovkin (2021). "Slowdown of the greening trend in natural vegetation with further rise in atmospheric CO_2." *Biogeosciences* 18.17, pp. 4985–5010. DOI: 10.5194/bg-18-4985-2021.

Wu, R.-J., M.-H. Lo, and B. R. Scanlon (2021). "The Annual Cycle of Terrestrial Water Storage Anomalies in CMIP6 Models Evaluated against GRACE Data." *Journal of Climate* 34.20, pp. 8205–8217. DOI: 10.1175/JCLI-D-21-0021.1.

Wu, T., Y. Lu, Y. Fang, X. Xin, L. Li, W. Li, W. Jie, J. Zhang, Y. Liu, L. Zhang, F. Zhang, Y. Zhang, F. Wu, J. Li, M. Chu, Z. Wang, X. Shi, X. Liu, M. Wei, A. Huang, Y. Zhang, and X. Liu (2019). "The Beijing Climate Center Climate System Model (BCC-CSM): the main progress from CMIP5 to CMIP6." *Geoscientific Model Development* 12.4, pp. 1573–1600. DOI: 10.5194/gmd-12-1573-2019.

Xu, X., J. Schimel, P. E. Thornton, X. Song, F. Yuan, and S. Goswami (2014). "Substrate and environmental controls on microbial assimilation of soil organic carbon: a framework for Earth System Models." *Ecology Letters* 17.5. DOI: 10.1111/ele.12254.

Xue, Y., T. M. Smith, and R. W. Reynolds (2003). "Interdecadal Changes of 30-Yr SST Normals during 1871–2000." *Journal of Climate* 16.10, pp. 1601–1612. DOI: 10.1175/1520-0442(2003)016<1601:ICOYSN>2.0.CO;2.

Yeager, S. G., G. Danabasoglu, N. A. Rosenbloom, W. Strand, S. C. Bates, G. A. Meehl, A. R. Karspeck, K. Lindsay, M. C. Long, H. Teng, and N. S. Lovenduski (2018). "Predicting Near-Term Changes in the Earth System: A Large Ensemble of Initialized Decadal Prediction Simulations Using the Community Earth System Model." *Bulletin of the American Meteorological Society* 99.9, pp. 1867–1886. DOI: 10.1175/BAMS-D-17-0098.1.

Yeager, S. G., N. Rosenbloom, A. A. Glanville, X. Wu, I. Simpson, H. Li, M. J. Molina, K. Krumhardt, S. Mogen, K. Lindsay, D. Lombardozzi, W. Wieder, W. M. Kim, J. H. Richter, M. Long, G. Danabasoglu, D. Bailey, M. Holland, N. Lovenduski, and W. G. Strand (2022). "The Seasonal-to-Multiyear Large Ensemble (SMYLE) Prediction System using the Community Earth System Model Version 2." *Geoscientific Model Development Discussions*, pp. 1–42. DOI: 10.5194/gmd-2022-60.

Yukimoto, S., H. Kawai, T. Koshiro, N. Oshima, K. Yoshida, S. Urakawa, H. Tsujino, M. Deushi, T. Tanaka, M. Hosaka, S. Yabu, H. Yoshimura, E. Shindo, R. Mizuta, A. Obata, Y. Adachi,

and M. Ishii (2019). "The Meteorological Research Institute Earth System Model Version 2.0, MRI-ESM2.0: Description and Basic Evaluation of the Physical Component." *Journal of the Meteorological Society of Japan. Ser. II* 97.5, pp. 931–965. DOI: 10.2151/jmsj.2019-051.

Zeng, N., J. D. Neelin, K.-M. Lau, and C. J. Tucker (1999). "Enhancement of Interdecadal Climate Variability in the Sahel by Vegetation Interaction." *Science* 286.5444, pp. 1537–1540. DOI: 10.1126/science.286.5444.1537.

Zeng, N., J.-H. Yoon, A. Vintzileos, G. J. Collatz, E. Kalnay, A. Mariotti, A. Kumar, A. Busalacchi, and S. Lord (2008). "Dynamical prediction of terrestrial ecosystems and the global carbon cycle: A 25-year hindcast experiment." *Global Biogeochemical Cycles* 22.4. DOI: https://doi.org/10.1029/2008GB003183.

Zeng, N., F. Zhao, G. J. Collatz, E. Kalnay, R. J. Salawitch, T. O. West, and L. Guanter (2014). "Agricultural Green Revolution as a driver of increasing atmospheric CO2 seasonal amplitude." *Nature* 515.7527, pp. 394–397. DOI: 10.1038/nature13893.

Zhang, Y. and A. Ye (2021). "Would the obtainable gross primary productivity (GPP) products stand up? A critical assessment of 45 global GPP products." *Science of The Total Environment* 783, p. 146965. DOI: 10.1016/j.scitotenv.2021.146965.

– (2022). "Improving global gross primary productivity estimation by fusing multi-source data products." *Heliyon* 8.3, e09153. DOI: 10.1016/j.heliyon.2022.e09153.

Zhang, Y., T. F. Keenan, and S. Zhou (2021). "Exacerbated drought impacts on global ecosystems due to structural overshoot." *Nature Ecology & Evolution* 5.11, pp. 1490–1498. DOI: 10.1038/s41559-021-01551-8.

Zhang, Y., M. P. Dannenberg, T. Hwang, and C. Song (2019). "El Niño-Southern Oscillation-Induced Variability of Terrestrial Gross Primary Production During the Satellite Era." *Journal of Geophysical Research: Biogeosciences* 124.8, pp. 2419–2431. DOI: https://doi.org/10.1029/2019JG005117.

Zhu, Y. and S. Yang (2021). "Interdecadal and interannual evolution characteristics of the global surface precipitation anomaly shown by CMIP5 and CMIP6 models." *International Journal of Climatology* 41.S1, E1100–E1118. DOI: https://doi.org/10.1002/joc.6756.

Ziehn, T., M. A. Chamberlain, R. M. Law, A. Lenton, R. W. Bodman, M. Dix, L. Stevens, Y.-P. Wang, J. Srbinovsky, T. Ziehn, M. A. Chamberlain, R. M. Law, A. Lenton, R. W. Bodman,

M. Dix, L. Stevens, Y.-P. Wang, and J. Srbinovsky (2020). "The Australian Earth System Model: ACCESS-ESM1.5." *Journal of Southern Hemisphere Earth Systems Science* 70.1, pp. 193–214. DOI: 10.1071/ES19035.

Zscheischler, J., M. D. Mahecha, J. von Buttlar, S. Harmeling, M. Jung, A. Rammig, J. T. Randerson, B. Schölkopf, S. I. Seneviratne, E. Tomelleri, S. Zaehle, and M. Reichstein (2014). "A few extreme events dominate global interannual variability in gross primary production." *Environmental Research Letters* 9.3, p. 035001. DOI: 10.1088/1748-9326/9/3/035001.

Zuo, H., M. A. Balmaseda, S. Tietsche, K. Mogensen, and M. Mayer (2019). "The ECMWF operational ensemble reanalysis–analysis system for ocean and sea ice: a description of the system and assessment." *Ocean Science* 15.3, pp. 779–808. DOI: 10.5194/os-15-779-2019.

ACKNOWLEDGMENTS

The work that went in this thesis would not have been possible without all the people at in- and outside the MPI supporting and helping me. I am deeply grateful for your contribution.

I want to thank my supervisors Victor and Tatiana. You helped me start my PhD in a new field, and guided me towards the relevant ideas and people. Thank you, Victor, for giving me the freedom to steer my research in the directions I was most interested in, and in helping me develop these ideas. Tatiana, thank you for pointing me towards new directions I would have missed, and thank you for all the encouraging and motivating words. My panel chair Martin has always allowed me to see my research through new eyes and put everything into perspective.

I'm immensely grateful to Antje, Cornelia, and Michaela for facilitating the path from my arrival at the institute up until the submission of my thesis.

Thanks to everyone at the MPI who have allowed me to familiarize myself with the work. Thank you, Aaron, for giving me a huge head start. Veronika and Nora, you have guided me through many technical difficulties. I especially thank all the attentive proofreaders who have helped me improve my writing, Hongmei, Meike, Marenka and Ellie.

Thank you, Zoé and Alex, for welcoming me at the institute and guiding me into the PhD life at MPI, and to everyone in the land department for the social events and enriching lunches.

I want to thank my parents for nourishing my interests and providing me with the education I was so lucky to enjoy. Thank you Marenka and Tony for all the support you have given me. Ellie – I'm grateful for having done this with you on my side.

EIDESSTATTLICHE VERSICHERUNG

Hiermit erkläre ich an Eides statt, dass ich die vorliegende Dissertationsschrift selbst verfasst und keine anderen als die angegebenen Quellen und Hilfsmittel benutzt habe.

20146 Hamburg, August 2022

István Dunkl

Hinweis / Reference

Die gesamten Veröffentlichungen in der Publikationsreihe des MPI-M
„Berichte zur Erdsystemforschung / Reports on Earth System Science“,
ISSN 1614-1199

sind über die Internetseiten des Max-Planck-Instituts für Meteorologie erhältlich:
http://www.mpimet.mpg.de/wissenschaft/publikationen.html

All the publications in the series of the MPI -M
„Berichte zur Erdsystemforschung / Reports on Earth System Science“,
ISSN 1614-1199

are available on the website of the Max Planck Institute for Meteorology:
http://www.mpimet.mpg.de/wissenschaft/publikationen.html